A Study of Gravitational Collapse of Filaments in Molecular Clouds with Radiation Hydrodynamics Simulations

Koji OGOCHI

A dissertation submitted to the Doctoral Program
in Physics, the University of Tsukuba
in partial fulfillment of the requirements for the
degree of Doctor of Philosophy (Science)

January, 2000

Abstract

We perform radiation hydrodynamics (RHD) simulations to study the self-gravitational collapse of the filaments in molecular clouds. For simplicity, we assume that the filaments are in 1-D axisymmetric geometry and that neither magnetic field nor angular momentum is present. We focus our attention on the radiative transfer effects.

The dynamics of the collapsing filaments strongly depends on thermodynamic properties. Especially, the isothermality has special meanings in the cylindrical geometry. Therefore, the careful treatments of thermodynamics are indispensable to study the collapse of the filaments. For the purpose, we take into account the effects of the radiative transfer since it mainly determines the energy flows. Unfortunately, simple approximated methods in which the optical depth is assumed are inadequate for our study. Instead, we adopt the variable Eddington factor (VEF) method though its numerical costs are expensive. This is the first RHD calculation using the VEF method for the collapse of the filaments.

From both analytic and computational calculations, we derive a criterion that the filaments can be isothermal during the collapse. The criterion is expressed in terms of the central density when the isothermality breaks down. We investigate the criterion under various conditions. As a result, we find that the criterion does not agree with an intuitive understanding that the

filaments become adiabatic when they become opaque to radiation. Indeed, numerical results show that the collapsing filaments can be still isothermal even when they become opaque, if the cooling rate dominates the heating rate. Alternatively, the filament temperature can depart from constant even in the optically thin regime if the heating rate exceeds the cooling rate.

Using the criterion, we also estimate the mass of dense cores which will be formed by the fragmentation of the filaments. It is expected that the estimated mass could explain the mass spectrum of very low mass stars such as brown dwarfs in star forming sites.

Contents

Abstract **iii**

1 Introduction **1**

1.1 Background 1

1.2 Thermodynamical effects 5

1.3 Purpose of this work 8

2 Model **11**

2.1 Overview 11

2.2 Gas 11

2.3 Dust grains 12

2.4 Heating and cooling processes 13

2.5 Filaments 14

2.6 Summary of modeling 15

3 Basic Equations **19**

3.1 Overview 19

3.2 Radiative transfer equation 20

3.3 Radiation hydrodynamics equations 23

4 Numerical Method **27**

4.1 Overview 27
4.2 Radiative transfer solver 29
4.2.1 Formal solution 30
4.2.2 Short/long characteristics method 31
4.2.3 The case of plane-parallel medium 31
4.2.4 The case of 1-D axisymmetric medium 33
4.2.5 To discretize the direction 35
4.3 Radiation hydrodynamics solver 37
4.3.1 Motion equation solver 37
4.3.2 Energy equations solver 38
4.4 Test problems 39
4.4.1 Blast wave 39
4.4.2 Static radiative diffusion 40
4.4.3 RT solver test 46

5 Numerical Results **49**
5.1 Standard model 50
5.1.1 Density and velocity 50
5.1.2 Gas temperature 57
5.1.3 Heating and cooling rates 58
5.1.4 Gravity and pressure forces 60
5.1.5 Optical depth 69
5.1.6 Radiative flux 70
5.2 Flat density model 71
5.3 Cosmic ray heating model 75

6 Discussion **77**
6.1 Criterion of the isothermality 78

6.1.1 Effective cooling rate 79
6.1.2 Cooling time-scale and dynamical time-scale 80
6.1.3 Characteristic densities 82
6.1.4 Comparison with numerical results 84
6.2 Fragmentation of filaments 91

7 Conclusions **95**

A Scalars, Vectors, and Tensors **99**

B Results of the standard model **101**

C Results of the flat density model **107**

D Results of the cosmic ray heating model **111**

Bibliography **115**

Chapter 1

Introduction

1.1 Background

Star formation is one of the most fundamental and important subjects in the modern astrophysics. The subject has been widely researched since 1950's with the modern physical considerations, but still there are a number of unsolved problems.

It is generally considered that stars form from molecular clouds through the gravitational collapse. According to a general picture, a gravitationally unstable gas cloud, in which the gravity is greater than other forces such as the pressure gradient force, the magnetic force, the centrifugal force, the radiation pressure, and so on, begins to collapse. The collapse would last until the gravity is overtaken by other forces. One main force which stops the gravitational collapse is the pressure, which tend to make an object hydrostatic by balancing the gravity and the pressure gradient. When a hydrostatic object is formed, it is expected that the object undergoes the Kelvin-Helmholtz contraction to end up with the formation of a star.

Although the general idea seems to be right, there are a lot of problems

to be addressed to understand the star formation process precisely. Some of them are as follows: Why is the molecular cloud gravitationally unstable? What is the realistic initial condition for the gravitational collapse? What are effects of other forces such as the magnetic force and the centrifugal force on the gravitational collapse? What is the mass of the star formed after the collapse? Does the collapse make a single star or a binary star system? Does the collapse make a planetary system like our Solar system or not?

Among the subjects listed above, the formation of a hydrostatic object due to the balance between the pressure and the gravity is an important and interesting subject because it makes an embryo of an ordinary star and it could determine fundamental properties of a star such as the mass.

The subject is also interesting because the mass of the first formed hydrostatic object may have a relation to the minimum mass of objects in the universe which are formed through the gravitational collapse of clouds. The mass of a newly born star, which is called the initial mass function (IMF), is a quite fundamental and important quantity in the modern astrophysics. The IMF seems to be a function of physical conditions of star forming clouds. However, the mechanism which generates the IMF is still uncertain. Observationally, it is considered that the IMF has a peak and a cut-off at the low-mass side below $1\,\mathrm{M}_\odot$ (where $\mathrm{M}_\odot$ denotes the solar mass unit, $1\,\mathrm{M}_\odot \approx 2.0 \times 10^{33}\,\mathrm{g}$). The cut-off of the mass might be determined by the minimum mass of the first formed hydrostatic object. Recently, some very low mass stars (VLMSs) about $0.01\,\mathrm{M}_\odot$ are detected (Martín *et al.* 1998 [15]; Zapatero Osorio *et al.* 1999 [51]). These observations are full of interesting suggestions to the formation of low-mass stars and the IMF. Though the minimum mass was estimated with some analytical considerations by Rees (1976 [34]) and Silk (1977 [37]), their estimations did not take into account

appropriately the geometrical and radiative transfer effects of clouds, which could be crucial. Thus it is not ready to adopt their estimation to compare with recent observational data. It seems necessary to reexamine the minimum mass of the first formed hydrostatic objects with including key effects accurately.

In early days, the formation of a hydrostatic object was investigated under the spherically symmetric approximation. For example, Larson (1969 [13]) carried out the numerical simulation of the spherically symmetric gravitational collapse of clouds. He found that the cloud collapse proceeds inhomogeneously. In other words, since the higher the density is, the faster the region falls in, the density in the central region rises first and forms the high density core remaining a low density skirt in an envelope. Because the radiative cooling efficiency decreases as the density of the central region increases, the temperature and the pressure in the region begins to rise, and finally the pressure force overtakes the gravity to form a hydrostatic core. This process was investigated by many following researchers taking into account the radiative transfer effects more precisely using numerical simulations (e.g., Winkler & Newman 1980 [48, 49]; Masunaga, Miyama, & Inutsuka 1998 [17]) as well as semi-analytic approaches (Stahler, Shu, & Taam 1980 [38, 39], 1981 [40]). Results of those works were not quite different from Larson's one qualitatively.

However, a number of observations have revealed that the star formation does not take place in a spherically symmetric manner. For instance, a rotating gas disk in a few thousand AU scale (AU stands for the Astronomical Unit, which is equal to 1.5×10^{13} cm) was discovered around a protostar candidate named "L1551 IRS 5" (Kaifu *et al.* 1984 [10]), a dynamically contracting disk-like object of a several hundred AU scale was discovered around

a newly born star named "HL Tau" (Hayashi, Ohashi, & Miyama 1993 [7]), and some young stellar objects were observed that they are surrounded by a non-spherical envelope (Padgett *et al.* 1999 [32]). Thus, it is clear that the collapse of the cloud which is not spherically symmetric should be investigated to understand the realistic star formation process.

On the other hand, observations have also discovered that many molecular clouds have filamentary shapes (e.g., Schneider & Elmegreen 1979 [36]) and that young stellar objects (YSOs) such as protostars or T Tauri stars are embedded in the clouds. These facts strongly suggest that stars are formed from the filamentary molecular clouds. Therefore, it seems to be necessary to investigate the gravitational collapse of filamentary clouds for understanding the real process of the star formation.

It is thought that these filamentary structures in a cloud are formed by the gravitational break-up of a sheet-like parent cloud; the numerical simulations performed by Miyama, Narita, and Hayashi (1987 [23]) indicated that a sheet-like cloud prefers to fragment into filaments. The following evolution of these filaments have been studied by many authors intensively (isothermal similarity solution: Inutsuka & Miyama 1992 [8]; effects of magnetic fields and/or rotation: Mouschovias & Morton 1991 [24], Nakamura, Hanawa, & Nakano 1995 [27], Basu & Mouschovias 1994 [1], Matsumoto, Nakamura, & Hanawa 1994 [20], Tomisaka 1995 [43], 1996 [45, 44], 1998 [46], Matsumoto, Hanawa, & Nakamura 1997 [19], Nakamura *et al.* 1999 [28]; effects of the equation of state: Inutsuka & Miyama 1997 [9], Kawachi & Hanawa 1998 [11], Nakamura 1998 [26], Ogochi & Nakamoto 1999 [31, 30]). It should be noticed, however, that in almost all works the dynamical evolution of a filamentary cloud has been investigated using the isothermal approximation.

1.2 Thermodynamical effects

Thermodynamic processes in the gravitationally collapsing clouds are important because they could determine the properties of newly born stars such as the mass and the luminosity. But the thermodynamical effects on the gravitational collapse of the filamentary clouds has been studied by only a few authors so far.

Inutsuka & Miyama (1997 [9]) studied the collapse of isothermal filaments and found that the filaments do not fragment into small cores if the temperature of the cloud keeps constant. They also estimated the density at which the cloud departs from the isothermal state to the adiabatic one. Since the change of the state increases the pressure and decelerates the contraction in the radial direction, the gravitational instability along the filament axis leads the fragmentation of the filament. Using the critical density for the isothermal collapse estimated analytically, they derived mass of fragments, which could be the minimum mass of hydrostatic objects formed through the gravitational collapse of clouds. However, it is not clear if their estimation of the critical density is accurate enough or not, because they used a simple analytical consideration. Moreover, it has been noticed that their estimation of the critical density was not valid for the case of an opaque filament (Masunaga & Inutsuka 1999 [16]).

Kawachi & Hanawa (1998 [11]) studied the gravitational collapse of filaments whose pressure can be given by $p = K\rho^{\gamma_p}$ (polytrope gas), where p is the pressure, ρ is the density, and K is a constant. The polytropic index γ_p was introduced to take into account the thermodynamic processes approximately. They found a similarity solution for the collapse when the polytropic index lies in the range $0 < \gamma_p < 1$. They pointed out that the thermodynamics is the key factor that determines the fate of the collapsing filaments.

However, they mainly investigated the case for $0 < \gamma_p < 1$ and constant γ_p, and the effect of phase change from the isothermal collapse to the adiabatic collapse was not addressed.

Nakamura (1998 [26]) investigated the collapse of filaments taking into account the radiative cooling processes by atomic elements, molecules, and dust grains. The collapse was simulated numerically. He found that the main coolants are CO molecules and dust grains. When the density of the hydrogen molecule gas $n(\mathrm{H_2})$ is less than about $10^5\,\mathrm{cm^{-3}}$, the CO molecule cooling dominates, while the dust grain cooling becomes dominant in the density region greater than $10^5\,\mathrm{cm^{-3}}$. Since the cooling rate becomes inefficient compared to the compressional heating rate at the density about $10^5\,\mathrm{cm^{-3}}$, the collapse is slightly slowed down at that density. Consequently a dense spindle and a diffuse envelope structure is formed. He continued the calculation until the central density reached $10^{10}\,\mathrm{cm^{-3}}$ and found that the filament fragments into small cores as illustrated in Fig. 1.1. He reported that the fragment mass depends on the amplitude of the initial density perturbation; when the perturbation is small (initial amplitude A is less than 0.1), the mass of the fragment becomes 0.1–0.5 $\mathrm{M_\odot}$ and when the perturbation is large ($A \sim 0.1$), the fragment mass becomes about $10\,\mathrm{M_\odot}$.

The calculation performed by Nakamura (1998 [26]) treated the gas compressional heating as a main heating source. According to observations, however, some amount of heating sources are present in the star forming molecular cloud regions. Some of them are interstellar radiation (consisting of X-rays, ultraviolet, visible, infrared, sub-mm, and millimeter radiation), and cosmic rays. For example, Goldsmith & Langer (1978 [6]) found that the gas temperature throughout most of the volume of a dense cloud lies in the range 8 to 12 K if cosmic rays are the only source of heating. This re-

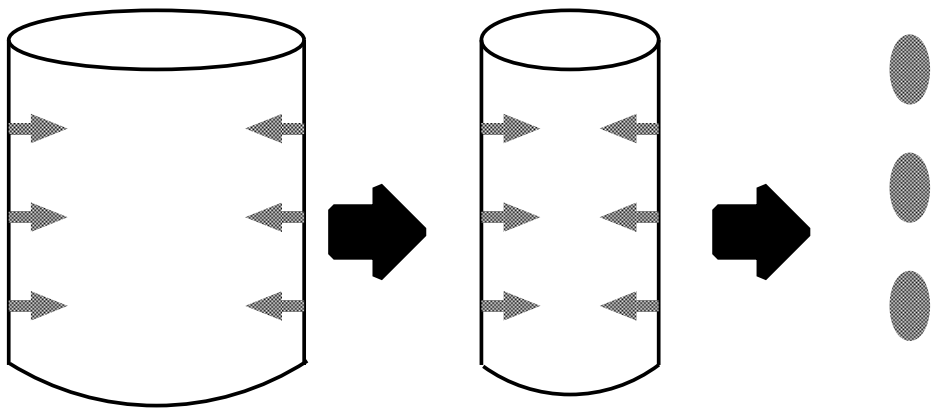

Figure 1.1: The schematic view of the evolution of a filamentary cloud.

sult is consistent with measurements of the dense cloud temperature, 9.5 K, by Dickman (1975 [4]), and implies that the assumption in the analysis by Goldsmith & Langer is valid. Also, Mathis, Mezger, & Panagia (1983 [18]) reported that the interstellar radiation could rise the temperature of dust grains in the cloud up to 3.2 K. When these external heating sources dominate all heating sources, the cloud temperature in an early phase of the collapse is determined by the balance between the external heating and the dust cooling. In that case, the temperature of the cloud would keep constant to a certain phase and the polytropic γ_p in the phase remains to be $\gamma_p = 1$. The collapse of a $\gamma_p = 1$ filament should be resultantly different from that of a $\gamma_p > 1$ cloud. Therefore, it is needed to investigate the gravitational collapse of filaments heated by external heating sources to reveal the real star formation process. Moreover, the radiation energy transport, which must be the key process to govern the thermodynamics of the collapsing cloud, should be treated carefully. Though the escape probability approximation for the line cooling rates (de Jong, Dalgarno, & Boland 1980 [3]) was employed in the analysis by Nakamura (1998 [26]), it is not clear if the approximation is valid enough or not in the case of the gravitational collapse of filaments.

1.3 Purpose of this work

During the star formation phase, the radiation plays an important role as the main energy transport mechanism, which has a great influence on thermodynamics and hydrodynamics of collapsing clouds. The filaments are generally isothermal in an early phase of the collapse but become non-isothermal at a certain phase. This thermodynamical transition depends on the radiative transfer mechanism. The mass of the first hydrostatic object formed by the collapse may be affected by the transition.

The purpose of this work is to study the gravitational collapse of filaments taking into account the radiative energy transport effect faithfully and to examine the critical density at which the collapsing filamentary cloud departs from the isothermal state. The critical density is quite important because it determines the mass of the first hydrostatic object formed by the gravitation collapse of clouds.

In the first step of this study, we establish a numerical method which enables us to treat the hydrodynamical collapse of filaments and the radiative energy transport consistently and accurately. But in general the calculation of radiation hydrodynamics (RHD) is quite difficult to carry out because it demands a huge amount of computation. That is the main reason why in almost all previous works some kind of approximation method has been used. In our study, we use the so-called variable Eddington factor method (Yorke 1980 [50]; Stone, Mihalas, & Norman 1992 [41]) that allows us to treat the radiation transfer appropriately in any optical depth situation, which is essentially desirable for our purpose because the critical density strongly depends on the radiation transfer process and the optical depth. This work is the first RHD calculation of collapsing filaments without adopting any approximation for optical depths.

Next, we carry out the RHD calculations and explore the thermodynamical and hydrodynamical behaviour of collapsing filaments. Then, the critical density for the thermodynamical change is examined. Investigating the behaviour of filaments with various initial and boundary conditions as well as considering the problem semi-analytically, we find a general description of the critical density. This is the main part of this study.

Finally, we estimate the mass of fragments which are produced by the fragmentation of filaments. It is revealed that the fragment mass depends on the initial temperature of the cloud and opacity of dust grains.

Chapter 2

Model

2.1 Overview

We simulate the evolution of a self-gravitating filamentary cloud taking into account the radiative transfer effects. To do that, we construct a model of the process. First, we assume that the filament is an infinitely long cylindrical cloud in which the density is uniform along the cylinder axis. It is also assumed that no magnetic field, no turbulent motion, and no rotation is present in the cloud. Each ingredient of our model is described in detail in this chapter.

2.2 Gas

The gas is assumed to be the ideal gas. The gas internal energy per unit mass $e_{\rm gas}$ is given by $e_{\rm gas} = c_v T$, where c_v is the specific heat and T is the gas temperature. The gas pressure is given by the equation of state for ideal gas, $p = (\gamma - 1)\rho e_{\rm gas}$, where ρ is the gas density and γ is the specific heat ratio.

We do not take into account the chemical reactions since our calculation does not depend on the chemical composition except for the mean molecular weight. The validity will be mentioned later. We also assume that the mean molecular weight is a constant, $\mu \simeq 2.3$, and that the specific heat ratio is a constant, $\gamma = 5/3$, since the rotational degrees of freedom of hydrogen molecules are not excited at low temperature of $T \lesssim 100\,\mathrm{K}$.

2.3 Dust grains

The typical molecular clouds contain the dust grains, which have the mass fraction about 0.01. The dust grains in the molecular clouds play an important role in radiative transfer mechanism not only as coolants of the gas clouds but also as absorbers of the radiation.

The rate of radiative energy emission per unit volume is $\rho\kappa_P B(T_d)$, where κ_P is the Planck mean opacity, T_d is the dust temperature, B is the frequency-integrated Planck function, $B(T) = \sigma T^4/\pi$, and σ is the Stefan-Boltzmann constant. The dust grains also absorb the radiation at the rate of $c\kappa_E E$, where κ_E is the energy mean opacity and E is the radiation energy density. The emission and absorption are the processes which exchange energy between the gas and dust grains.

If T_d is lower than the gas temperature, the dust cooling is not effective. The gas particles and dust grains, however, are thermally well-coupled in clouds concerned in our study since the density is high enough, $\rho > 10^{-19}\,\mathrm{g\,cm^{-3}}$. Therefore, T_d is assumed to be equal to the gas temperature and the dust cooling is effective.

The opacity of dust grains in interstellar medium at large wavelength compared to the grain size has the dependence on the frequency as $\kappa_\nu \propto \nu^\beta$.

Theoretically, the value of β is expected to be 2, if the constituent of dust grains is an ordinary dielectric material. The typical value of β is $\beta = 2$ (Draine & Lee 1984 [5]; Beckwith & Sargent 1991 [2]; Miyake & Nakagawa 1993 [22]; Pollack *et al.* 1994 [33]), or it is reported that $1.75 \leq \beta \leq 2.5$ in the Orion Molecular Cloud-1 (Lis *et al.* 1998 [14]). Then, the Planck mean opacity of κ_ν at the low temperature is proportional to T_d^β. A model parameter κ_{10} is also defined as the Planck mean opacity at $T_d = 10\,\mathrm{K}$. Thus, the Planck mean opacity is given by

$$\kappa_P = \kappa_{10} \left(\frac{T_d}{10\,\mathrm{K}} \right)^\beta . \tag{2.1}$$

Notice that the κ_{10} depends on the dust size and the metallicity, which can vary for each cloud. Also, the β could vary from cloud to cloud. Therefore, we leave κ_{10} and β as parameters in our model.

2.4 Heating and cooling processes

Observations suggest that the temperature of the molecular clouds is about 10–60 K. We explore this range as the initial conditions in our numerical simulations. The temperatures are determined by the balance between the heating and cooling processes. Then, the question is which process dominates? In the dense clouds, the dust cooling is more effective than the other cooling processes such as CO line cooling, which is the most effective one among the molecular line cooling processes. The dust cooling rate Λ_{dust} is

$$\Lambda_{\mathrm{dust}} = 4\sigma\kappa_P T^4 = 4.5 \times 10^{-2} \left(\frac{\kappa_{10}}{0.02\,\mathrm{g^{-1}\,cm^2}} \right) \left(\frac{T}{10\,\mathrm{K}} \right)^{4+\beta} \mathrm{erg\,g^{-1}\,s^{-1}}, \tag{2.2}$$

and CO line cooling rate Λ_{CO} is $\Lambda_{\mathrm{CO}} \sim 3 \times 10^{-5}\,\mathrm{erg\,g^{-1}\,s^{-1}}$, when $n(\mathrm{H_2}) < 10^6\,\mathrm{cm^{-3}}$ (Goldsmith & Langer 1978 [6]). Therefore, the line coolings can be

ignored, and there is no need to take the chemical reactions into account.

As to the heating processes, it can be considered that the main heating sources which maintain the initial temperature in the early phase are the incident radiation from nearby stars and the cosmic rays since the compressional heating rate due to the gravitational collapse in that phase is very small (Goldsmith & Langer 1978 [6]; Mathis, Mezger, & Panagia 1983 [18]). Though there must be some extent of external heating sources, the amount could vary from place to place in a parent cloud. Therefore, we would rather leave the external heating mechanism and its intensity as model parameters.

2.5 Filaments

Some observations suggest that many molecular clouds have filamentary shapes. We simplify the model of the filamentary clouds to save numerical costs and to clear the effects of the radiation transfer. The filaments are assumed to be an axisymmetric infinite cylinder and to have no magnetic field and no rotation. Also we suppose that the density of the filaments is given by

$$\rho(r) = \rho_{\rm init} \left[1 + \left(\frac{r}{hH(\rho_{\rm init}, T_{\rm init})} \right)^2 \right]^{-2}, \tag{2.3}$$

where $\rho_{\rm init}$ is the density on the axis, H is a scale height, and h is a model parameter (see Fig. 2.1). This scale height H is a function of the density on the axis and the temperature,

$$H(\rho, T) = \left(\frac{2\mathcal{R}T}{\pi G \rho \mu} \right)^{1/2}. \tag{2.4}$$

The filaments are in the hydrostatic equilibrium state in the case of $h = 1$ and the filaments contract gravitationally if $h > 1$.

The mass of a filament per unit length is called the line mass. The line mass of the isothermal equilibrium filament $m_{\rm eq}$ can be obtained by substituting $h = 1$ in Eq. (2.3) and integrating over radius,

$$m_{\rm eq}(T) \equiv \int_0^\infty 2\pi r \rho(r; h{=}1)\, dr = \frac{2\mathcal{R}T}{G\mu} \approx 17 \left(\frac{T}{10\,{\rm K}}\right) {\rm M}_\odot\,{\rm pc}^{-1}. \qquad (2.5)$$

It is remarkable that the $m_{\rm eq}$ is independent of the central density. The line mass of the filament of with $h > 1$ is given by $h^2 m_{\rm eq}$.

The $m_{\rm eq}H$ has the dimension of mass, and it corresponds to the Jeans mass. Therefore a filament which has a line mass $h^2 m_{\rm eq}$ is gravitationally unstable in the case of $h > 1$. It corresponds to the Jeans criterion and the model parameter h represents the degree of gravitational instability.

The numerical simulations of the fragmentation of sheet-like cloud performed by Miyama, Narita, & Hayashi (1987 [23]) have shown that the line mass of a formed filament was twice of the equilibrium line mass. Therefore we adopt $h = \sqrt{2}$ for typical models.

2.6 Summary of modeling

We consider in this work three types of models named as,

1. Standard model,

2. Flat density model,

3. Cosmic ray heating model.

In the standard model, the initial density distribution is given by Eq. (2.3), and the main heating source at the initial time is assumed to be incident radiation.

The flat density model is almost identical to the standard model except for an initial density distribution. The line mass, however, is the same value ($h^2 m_{\rm eq}$) with the standard model. The initial density distribution is given by Eq. (2.6).

$$\rho(r) = \begin{cases} \rho_{\rm init} & \text{for } r \leq hH(\rho_{\rm init}, T_{\rm init}) \\ \sim 0 & \text{otherwise} \end{cases} \tag{2.6}$$

The cosmic ray heating model has no incident radiation. The energy balance at the initial time is established by the cosmic ray heating. The heating process which is dominant at the initial time is essentially different from the standard model. The other conditions are the same to those of the standard model.

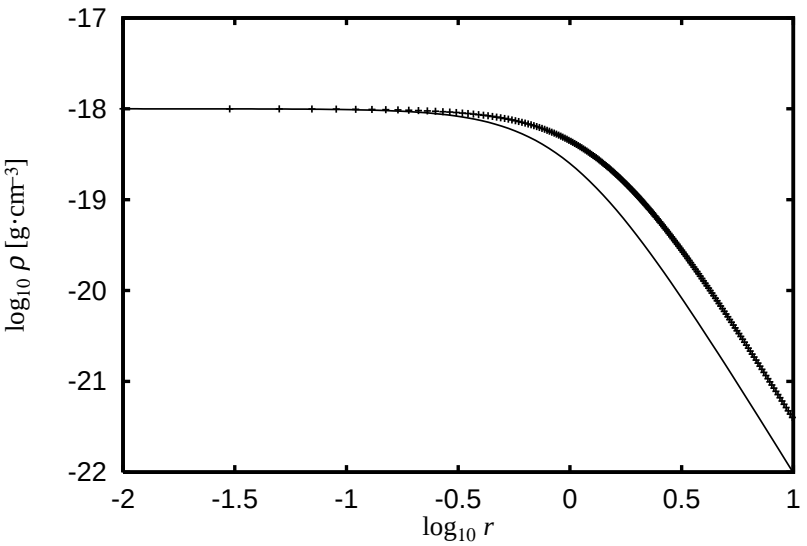

Figure 2.1: A set of points denotes an initial density distribution ($h = \sqrt{2}$) and a solid line denotes the equilibrium distribution ($h = 1$), whose central density is taken to be $10^{-18}\,{\rm g\,cm^{-3}}$.

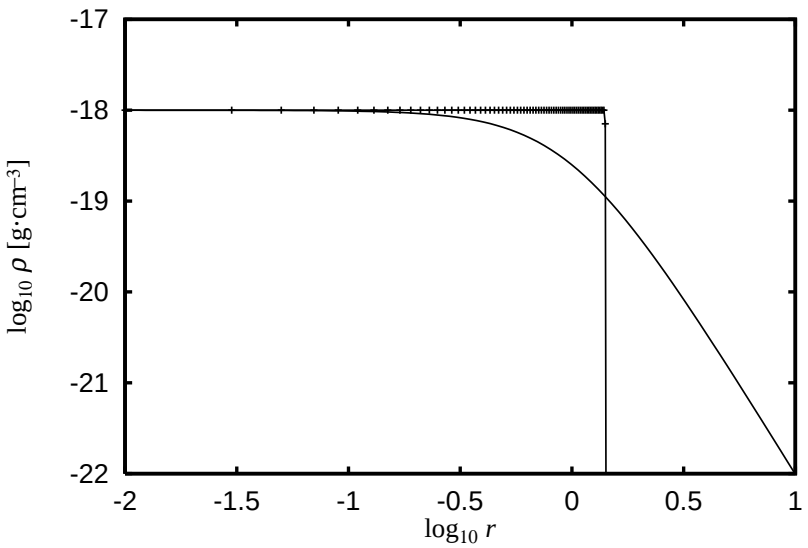

Figure 2.2: Initial density distribution for the flat density model. The meanings of points and a solid line is the same to Fig. 2.1.

Chapter 3

Basic Equations

3.1 Overview

The basic equations and concepts of the radiative transfer and radiation hydrodynamics (RHD) are described in this chapter.

The radiative transfer equation is solved to obtain geometrical information of the radiation field, and the RHD equations are solved to update the gas and radiation distribution, such as the gas density, the velocity, the gas energy density, the radiative energy density, and the radiative flux.

The importance of the radiation on the thermodynamics and the hydrodynamics can be represented by two parameters (Mihalas & Mihalas [21]). A parameter R is defined as the ratio of the gas internal energy density to the radiation energy density at the thermal equilibrium state,

$$R \equiv \frac{\rho c_v T}{aT^4} \sim 7.1 \left(\frac{\rho}{10^{-18}\,\mathrm{g\,cm^{-3}}}\right)\left(\frac{T}{10\,\mathrm{K}}\right)^{-3}. \tag{3.1}$$

This ratio R gives a measure of the relative importance of gas and radiation pressure because the perfect gas pressure is two thirds of the gas internal energy density and the radiation pressure is one third of the radiation energy

density. When the value R is large enough, the radiation pressure can be ignored.

The other parameter, B_o, is the Boltzmann number which is defined as the ratio of the gas energy flux to the radiative flux,

$$B_o \equiv \frac{\rho\,(e_{\rm gas}+p)c_T}{\sigma T^4} \sim 3.0\times10^{-5}\left(\frac{\rho}{10^{-18}\,{\rm g\,cm^{-3}}}\right)\left(\frac{T}{10\,{\rm K}}\right)^{-5/2}. \qquad (3.2)$$

When B_o is small, the radiative energy transport is important compared to the energy transport due to the gas flow. At $\rho = 10^{-18}\,{\rm g\,cm^{-3}}$ and $T = 10$ K, the energy transport by the radiation is greatly larger than that by the gas. This means that the radiative transport is quite important for the star formation process. From these considerations, it can be seen that the radiative energy transport should be treated accurately to investigate the formation process of stars.

In order to take into account the radiative transfer appropriately, we have to solve the radiative transfer equation. We also solve the ordinary hydrodynamics equations to simulate the gravitational collapse of filaments.

3.2 Radiative transfer equation

Using the specific intensity I_ν, the radiation energy crossing a surface element $d\boldsymbol{S}$, in a time interval dt, in a frequency range $d\nu$, into a solid angle $d\Omega$ around a unit direction vector $\boldsymbol{n}$, (Fig. 3.1) is written as

$$dE_\nu = I_\nu(\boldsymbol{x},\boldsymbol{n})\,\boldsymbol{n}\cdot d\boldsymbol{S}\,d\Omega\,d\nu\,dt. \qquad (3.3)$$

In principle, the intensity depends on the time. However, the speed of light or the diffusion velocity c/τ is so fast that the radiation field in the star forming region achieves steady distribution in a short time period which is much smaller than the time scale of some hydrodynamic motions. Thus, we

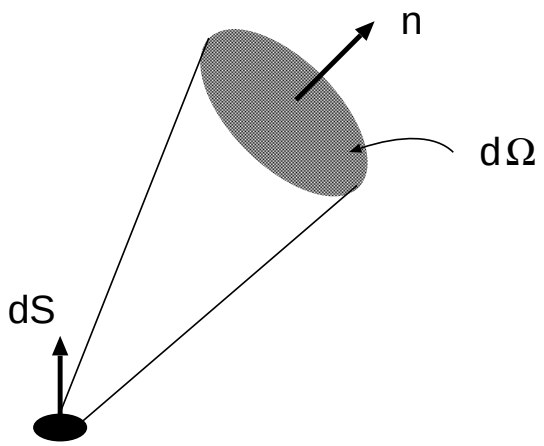

Figure 3.1: The radiative energy flow

can ignore the time dependence of the intensity. Then the intensity depends on six independent variables, i.e., three from the configuration space ($\boldsymbol{x}$), two from the directions ($\boldsymbol{n}$), and one from the frequency (ν), in general. The intensity has the relation to the photon distribution function in the phase space, and the intensity provides the complete description about the radiation field.

The intensity I_ν can be obtained by the radiative transfer equation, which is essentially equal to the Boltzmann transfer equation for the photon distribution function,

$$\frac{dI_\nu}{ds} = -\chi_\nu I_\nu + \eta_\nu, \tag{3.4}$$

where ds is an element of the length along a ray, χ_ν is the frequency dependent extinction coefficient, and η_ν is the frequency dependent emission coefficient. The intensity I_ν varies along the ray due to the absorption and the emission. The extinction coefficient χ_ν is often substituted for $\rho\kappa_\nu$, where κ_ν is called the opacity.

Assuming the local thermodynamic equilibrium (LTE), a relation between the emission and the absorption is established (the Kirchhoff's law; Rybicki & Lightman [35]),

$$\eta_\nu = \chi_\nu B_\nu, \tag{3.5}$$

where B_ν is the Planck function given by

$$B_\nu(\nu, T) = \frac{2h\nu^3}{c^2} \frac{1}{e^{h\nu/k_B T} - 1}, \tag{3.6}$$

and h is the Planck constant and k_B is the Boltzmann constant.

Summing up over all frequencies, integrated 'gray' variables can be obtained, i.e., η is the integrated total emission coefficient, written as

$$\eta \equiv \int_0^\infty \eta_\nu \, d\nu = \int_0^\infty \rho \kappa_\nu B_\nu \, d\nu = \rho \kappa_P B, \tag{3.7}$$

where B is the integrated Planck function, $B = \sigma T^4/\pi$, and κ_P is the Planck mean opacity defined as

$$\kappa_P \equiv \frac{\int_0^\infty \kappa_\nu B_\nu \, d\nu}{\int_0^\infty B_\nu \, d\nu}. \tag{3.8}$$

The variables integrated over frequencies are denoted by the symbols without a suffix of ν as like η instead of η_ν.

Integrating the specific intensity over all solid angles, we can obtain moments of the intensity. The radiative energy density per unit volume is obtained as

$$E(\boldsymbol{x}) \equiv \frac{1}{c} \oint I(\boldsymbol{x}, \boldsymbol{n}) \, d\Omega. \tag{3.9}$$

Multiplying $\boldsymbol{n}$ and integrating, the radiative flux vector is obtained as

$$\boldsymbol{F}(\boldsymbol{x}) \equiv \oint I(\boldsymbol{x}, \boldsymbol{n}) \boldsymbol{n} \, d\Omega. \tag{3.10}$$

Multiplying $\boldsymbol{nn}$ and integrating, the radiative pressure tensor is obtained as

$$\mathsf{P}(\boldsymbol{x}) \equiv \frac{1}{c} \oint I(\boldsymbol{x}, \boldsymbol{n}) \boldsymbol{nn} \, d\Omega. \tag{3.11}$$

Notice that these moments, E, $\boldsymbol{F}$, and P, do not depend on the direction and the frequency. In the system of the RHD equations, these moments, are used rather than the specific intensity itself.

3.3 Radiation hydrodynamics equations

Some equations or some terms are joined to the equations of hydrodynamics (HD) to include the effects of the radiation. RHD equations are expressed as follows.

The equation of state for the ideal gas:

$$p = \frac{\mathcal{R}}{\mu} \rho T = (\gamma - 1) \rho e_{\mathrm{gas}}, \tag{3.12}$$

where p is the gas pressure, $\mathcal{R}$ is the gas constant, μ is the mean molecular weight, ρ is the gas density, T is the gas temperature, e_{gas} is the gas energy density per unit mass, and γ is the ratio of specific heat.

The equation of continuity:

$$\frac{\partial \rho}{\partial t} + \nabla \cdot (\rho \boldsymbol{v}) = 0, \tag{3.13}$$

where $\boldsymbol{v}$ is a velocity vector.

The equation of motion:

$$\frac{D\boldsymbol{v}}{Dt} = -\frac{1}{\rho} \nabla p + \boldsymbol{g} + \frac{\kappa_F}{c} \boldsymbol{F}, \tag{3.14}$$

where κ_F is the flux-mean opacity given by

$$\kappa_F \equiv \frac{\int_0^\infty \kappa_\nu F_\nu, d\nu}{\int_0^\infty F_\nu \, d\nu}, \tag{3.15}$$

and $\boldsymbol{g}$ is the gravitational acceleration. For the 1-D axisymmetric geometry, all components of $\boldsymbol{g}$ are zero except for the radial component g_r. The radial component of $\boldsymbol{g}$ becomes

$$g_r = -\frac{2Gm_r}{r}, \tag{3.16}$$

where G is the gravitational constant and m_r is a line mass inside radius r.

Energy equations:

$$\frac{D}{Dt}\left(e_{\rm gas} + \frac{E}{\rho}\right) + \frac{1}{\rho}\nabla\cdot\boldsymbol{F} = \Gamma_{\rm dyn} + \Gamma_{\gamma} + \Gamma_{\rm ext}, \tag{3.17}$$

$$\frac{De_{\rm gas}}{Dt} = \Gamma_{\rm dyn} + \Gamma_{\rm abs} - \Lambda_{\rm dust} + \Gamma_{\rm ext}, \tag{3.18}$$

where E is the radiation energy density per unit volume. Each term in RHSs is a heating/cooling rate per unit mass expressed below.

The gas compressional heating rate is written as

$$\Gamma_{\rm dyn} = -\frac{p}{\rho}\nabla\cdot\boldsymbol{v}. \tag{3.19}$$

The rate of radiation energy absorption by dust grains is written,

$$\Gamma_{\rm abs} = c\kappa_E E, \tag{3.20}$$

where κ_E is the energy-mean opacity defined as

$$\kappa_E \equiv \frac{\int_0^\infty \kappa_\nu E_\nu, d\nu}{\int_0^\infty E_\nu\, d\nu}. \tag{3.21}$$

The emission rate by the dust grains is written,

$$\Lambda_{\rm dust} = 4\kappa_P\sigma T^4. \tag{3.22}$$

The radiation compressional heating rate is given by

$$\Gamma_{\gamma} = -\frac{\mathsf{P}}{\rho}:\nabla\boldsymbol{v}. \tag{3.23}$$

The heating rate by the external heating source, e.g., the cosmic rays, is written as $\Gamma_{\rm ext}$.

The equation of radiative flux:

$$\frac{D\boldsymbol{F}}{Dt} = -c^2 \nabla \cdot \mathsf{P} - \rho \left[c\kappa_F + \frac{1}{\rho} \nabla \cdot \boldsymbol{v} \right] \boldsymbol{F}. \tag{3.24}$$

The system of the RHD equations described here is not closed, since an equation for the time evolution of P is absent. But the equation $D\mathsf{P}/Dt = \cdots$ contains the term of higher order moments, therefore the system will be never closed. The details of the closure problem are described in the next chapter.

Chapter 4

Numerical Method

4.1 Overview

We require a numerical method which can solve the radiation hydrodynamics (RHD) for any optical depth, since the optical depth of gravitationally collapsing clouds changes significantly. The variable Eddington factor method (VEF) is a method which satisfies our requirements with the present computational facilities. The key point of the VEF algorithm is to close the system of equations by using the variable Eddington factors. They are geometrical factors of the radiation field, and it is necessary to solve the radiative transfer equation in order to obtain the variable Eddington factors.

We have developed a numerical RHD code using the VEF algorithm (Nakamoto & Ogochi 1997 [25]; Ogochi & Nakamoto 1999 [31, 30]), which is based on the ZEUS-2D (Stone & Norman 1992 [42]; Stone, Mihalas, & Norman 1992 [41]). Differences between our code and the ZEUS-2D are that we reduced the geometrical dimension to 1-D and that we used the Lagrangian technique instead of the Eulerian technique. Our code can solve the problem with the Cartesian coordinates, the cylindrical coordinates, and the spherical

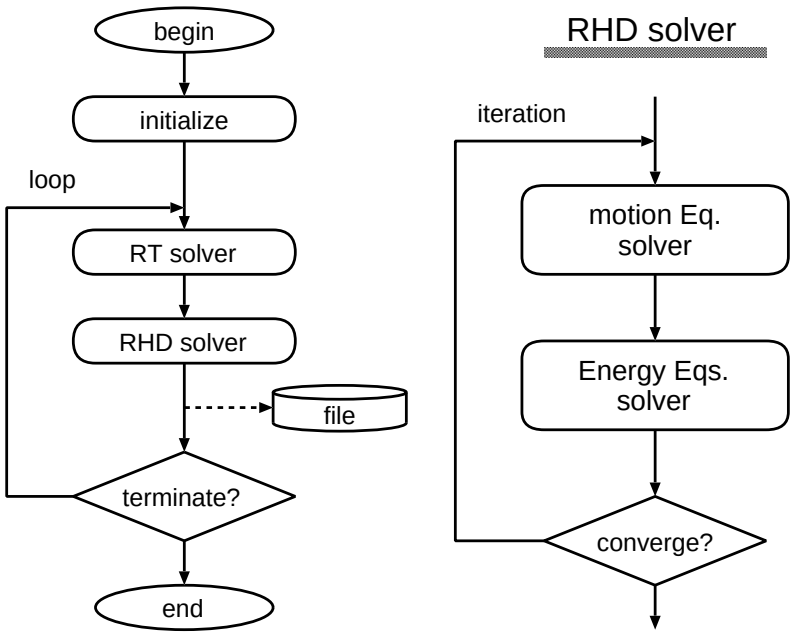

Figure 4.1: The flow chart of our code.

coordinates.

The numerical code can be divided into two parts; one is the radiation transfer (RT) solver and the other is the RHD solver (see Fig. 4.1). These parts are independent each other. It is possible to run the code without the RT solver by utilizing some approximations. The RHD solver can again be divided into the motion equation solver and the energy equation solver. The details are described below.

The computational sequence of the method is following:

1. obtain the intensity I by solving the radiative transfer equation at each point,

2. calculate the 0th and 2nd order moments of the intensity,

3. calculate the Eddington factor tensor $\mathsf{f} = \mathsf{P}/E$ from the moments,

4. substitute $\mathsf{f}E$ for the radiative pressure tensor P in the energy equations.

The reason for such complicated procedures is that there is no equation which represents time evolution of P in basic equations. This is a well-known problem as the closure problem; the equation of time evolution of the n th moment contains the term of the $n+1$ th moment, and therefore the system of the equations is never closed. To close the sequence, we adopt a closure relation $\mathsf{P} = \mathsf{f}E$. This is called the Variable Eddington Factor approximation.

The Variable Eddington Factor method is one that has been used since 1980's for spherically symmetric problems (Yorke 1980 [50]; Winkler & Newman 1980 [48, 49]; Masunaga, Miyama, & Inutsuka 1998 [17]) and been confirmed that it can calculate arbitrary optical depth situations with high accuracy; the method is more accurate than the diffusion approximation or flux-limited diffusion approximation method, especially at a place where the optical depth is around unity. We apply the Variable Eddington Factor method for the cylindrical problems.

The details of each step are described below.

4.2 Radiative transfer solver

The aim to solve the radiative transfer equation is to obtain the geometrical information of the radiation field, which is expressed as the tensor Eddington factor. The tensor Eddington factor obtained by the RT solver is used in the RHD solver. The reason why the RHD solver requires the Eddington factor is that the system of moment equations for RHD is not closed by itself. The closure relation is generally uncertain unless the radiative transfer equation is solved.

4.2.1 Formal solution

Substituting $d\tau$ for χds in the Eq. (3.4), the radiative transfer equation is written as

$$\frac{dI}{d\tau} = -I + S, \tag{4.1}$$

where S is the so-called source function defined as the ratio of the emission coefficient to the absorption coefficient, $S = \eta/\chi$. The formal solution of above differential equation can be expressed as

$$I(\tau) = I(0)e^{-\tau} + \int_0^\tau e^{-(\tau-\tau')} S(\tau')\, d\tau'. \tag{4.2}$$

The intensity $I(0)$ should be given as the boundary conditions according to the problems. The source function S is determined by physical processes at that place, e.g., by the quantum mechanical processes of photons with atoms, molecules, and dust grains. In the case of the LTE, the source function becomes equal to the Planck function with the temperature at the point.

We integrate the Eq. (4.2) along a line of ray from one grid point to the other grid point. Then we obtain a formula used in the numerical code. The discrete grid points are labeled by the sequential number. The variables on each grid point are denoted by the suffixed symbol such as S_i, S_{i+1}. Integrating the Eq. (4.2) from i to $i+1$, the intensity I_{i+1} is calculated as

$$I_{i+1} = I_i e^{-\Delta\tau_i} + S_{i+1} - S_i e^{-\Delta\tau_i} - \frac{S_{i+1} - S_i}{\Delta\tau_i}(1 - e^{-\Delta\tau_i}), \tag{4.3}$$

where I_i is the intensity at the upwind grid point, and $\Delta\tau_i$ is the optical depth from i th point to $i+1$ th point. One advantage of this difference formula is that it is more robust to calculate arbitrary optical depth situations than a formula based on the differential equation.

4.2.2 Short/long characteristics method

There are two well-known ideas to calculate the intensity on all the grid points, they are so-called the short characteristics method and the long characteristics method. These names are taken from the length of integral path, which is "short" or "long".

Generally, each method has merits and demerits; the short characteristics method is low-cost but diffusive, since that method interpolates both the intensity and the source function. On the contrary, the long characteristics method interpolates only the source function, therefore that method is precise but costly. Such differences, however, exist only in the case of 2-D or 3-D. Two methods are equivalent in 1-D since there is no need to interpolate the intensity.

4.2.3 The case of plane-parallel medium

We now consider the radiative transfer in a layered plane-parallel medium (see Fig. 4.2), which is the most simple example, to explain the procedures of the RT solver.

Notice that the intensity I generally depends not only on z but also on Θ. Therefore, it is necessary to integrate along the many various rays to obtain the intensity with various Θ, which is the angle between the path and the z axis. It is convenient to use $\mu = \cos\Theta$ as the variable instead of Θ itself, therefore μ is used as well as Θ below.

The radiative transfer equation for a plane-parallel medium can be written as

$$\mu \frac{dI(z,\mu)}{dz} = -\chi(z)\,[I(z,\mu) - S(z)]\,. \tag{4.4}$$

As shown in Fig. 4.2, the formal solution should be integrated from the

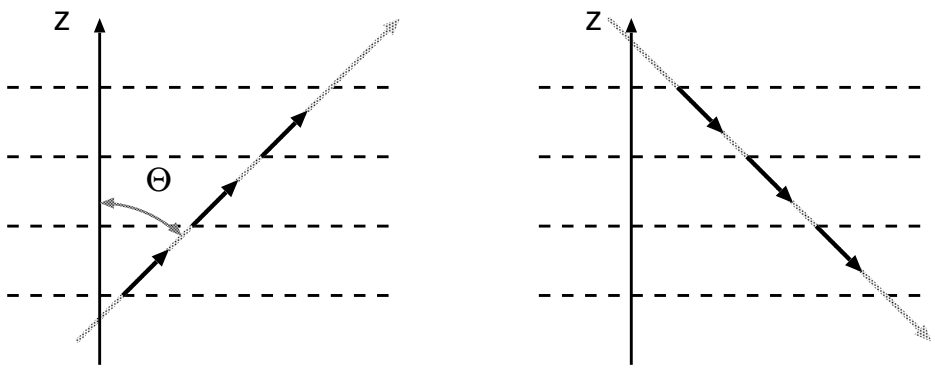

Figure 4.2: The radiative transfer in a layered plane-parallel medium. The oblique and long arrow denotes a virtual ray, which is a integral path for the radiative transfer equation. The angle between z axis and the ray is denoted by Θ, which has the range of $0 \leq \Theta \leq \pi$. The short arrows along the ray denote the intensity at those points, which are calculated by integrating radiative transfer equation. For $0 \leq \Theta < \pi/2$ (see left), the integration should be done from the bottom to the top. On the contrary, the integration should be done from the top to the bottom for $\pi/2 < \Theta \leq \pi$ (see right).

bottom to the top when $0 < \mu \leq 1$, and from the top to the bottom when $-1 \leq \mu < 0$.

Once the intensities are obtained, the moments should be calculated next. Practically, these two procedures are done at the same time in the numerical code.

The moments of intensity for a plane-parallel medium are defined as

$$J(z) \equiv \frac{1}{2} \int_{-1}^{1} I(z, \mu)\, d\mu, \tag{4.5}$$

$$H(z) \equiv \frac{1}{2} \int_{-1}^{1} \mu I(z, \mu)\, d\mu, \tag{4.6}$$

$$K(z) \equiv \frac{1}{2}\int_{-1}^{1} \mu^2 I(z,\mu)\, d\mu, \tag{4.7}$$

where J, H, K are 0th, 1st, and 2nd moments.

As mentioned above, the intensity itself is not referred in the RHD solver in the VEF method. The directional dependence of the intensity is reduced to an integrated variable so-called the Eddington factor, which is defined as the ratio of 2nd moment to 0th moment. For the plane-parallel medium, it can be calculated as following,

$$f = \frac{\int_{-1}^{1} I\mu^2\, d\mu}{\int_{-1}^{1} I\, d\mu}. \tag{4.8}$$

4.2.4 The case of 1-D axisymmetric medium

We have explained the procedures to calculate the Eddington factor for the plane-parallel medium as a simple example. Now, we present the actual method used in our RT solver for 1-D axisymmetric medium.

The axisymmetric geometry is more complicated in comparison with the plane-parallel geometry. The direction in the axisymmetric geometry depends not only on Θ but also on the azimuthal angle Φ (see Fig. 4.3), while the direction in the plane-parallel geometry depends only on the polar angle Θ. The polar angle Θ is replaced with $\mu = \cos\Theta$ like the case of the plane-parallel medium. The moments of the intensity in the 1-D axisymmetric medium are expressed as following:

$$J(r) = \frac{1}{4\pi}\int_{-1}^{1} d\mu \int_{0}^{2\pi} d\Phi\; I(r,\mu,\Phi) \tag{4.9}$$

$$H_r(r) = \frac{1}{4\pi}\int_{-1}^{1} d\mu \int_{0}^{2\pi} d\Phi\; (1-\mu^2)^{1/2}\cos\Phi I(r,\mu,\Phi), \tag{4.10}$$

$$K_{rr}(r) = \frac{1}{4\pi}\int_{-1}^{1} d\mu \int_{0}^{2\pi} d\Phi\; (1-\mu^2)\cos^2\Phi I(r,\mu,\Phi), \tag{4.11}$$

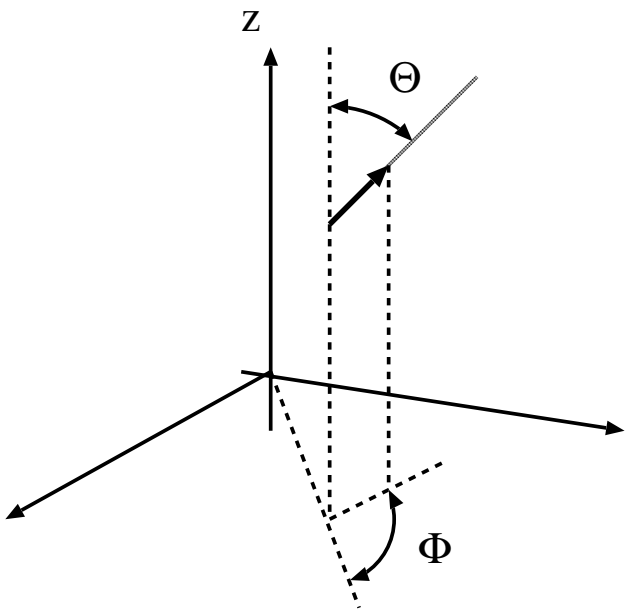

Figure 4.3: The directional dependence in the axisymmetric geometry.

$$K_{zz}(r) = \frac{1}{4\pi}\int_{-1}^{1} d\mu \int_{0}^{2\pi} d\Phi\ \mu^2 I(r,\mu,\Phi), \tag{4.12}$$

$$K_{\Phi\Phi}(r) = \frac{1}{4\pi}\int_{-1}^{1} d\mu \int_{0}^{2\pi} d\Phi\ (1-\mu^2)\sin^2\Phi I(r,\mu,\Phi). \tag{4.13}$$

Note that the 2nd moments K_{rr}, K_{zz}, $K_{\Phi\Phi}$ are components of 2-rank tensor and that the other components such as K_{rz}, $K_{r\Phi}$ and $K_{z\Phi}$ are identically zero due to the axisymmetric geometry. The 1st moment H_z is also zero identically. The Eddington factors are defined as

$$f_{rr} \equiv \frac{K_{rr}}{J}, \quad f_{zz} \equiv \frac{K_{zz}}{J}, \quad f_{\Phi\Phi} \equiv \frac{K_{\Phi\Phi}}{J}. \tag{4.14}$$

There is no need to calculate all of f_{rr}, f_{zz}, and $f_{\Phi\Phi}$ since $f_{rr} + f_{zz} + f_{\Phi\Phi} \equiv 1$.

4.2.5 To discretize the direction

The next problem is how to generate directional grids which must cover all the directions at any spatial positions. Though the directional dependence becomes complicated as described before, there is a skillful method for the spherical geometry or the cylindrical geometry.

Many planes crossing a cylinder with various offsets are considered, whose topview are illustrated in Fig. 4.4. Each plane is called the 'tangent plane', and the distance from the center of the cylinder is called the 'impact parameter', which is denoted by p. Notice that the radial spatial grid 'points' are expressed as 'arcs' in this figure. Each tangent plane intersects arcs with various radii and azimuthal angles. For example, a tangent plane crossing the center (that plane is specified by $p = 0$) intersects all radial 'points' with $\Phi = 0$ or $\Phi = \pi$. When $p > 0$, the azimuthal angles crossing each radial 'point' is not constant; the azimuthal angle at a radial grid 'point' r is $\Phi = \arcsin(p/r)$ (obviously $p \leq r$). When we focus on a radial grid 'point', we can observe that the point expressed by an arc is threaded by many rays. Since the arc represents an identical spatial point, many rays that thread the arc express the intensities which pass the point with different angles. By summing up the intensity on the arc, we can calculate the integration of the intensity over the direction at a spatial point.

Each tangent plane can be treated as the plane-parallel medium, since the cylinder is independent of z (see Fig. 4.5).

The azimuthal resolution is determined by the number of the tangent planes and their distribution. At least, the same number with the radial grids is needed to inform the inner structure to the outer region. After all, the needed number of the tangent planes is about twice of the number of radial grids to achieve enough azimuthal resolution at the inner radii.

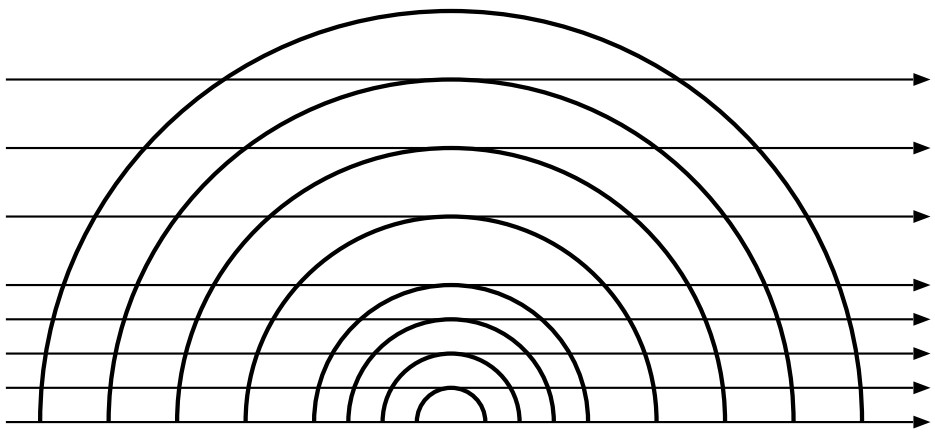

Figure 4.4: Topview. Arcs denote radial grids and horizontal lines denote tangent planes. All the points on the same arc are equivalent due to the axisymmetry.

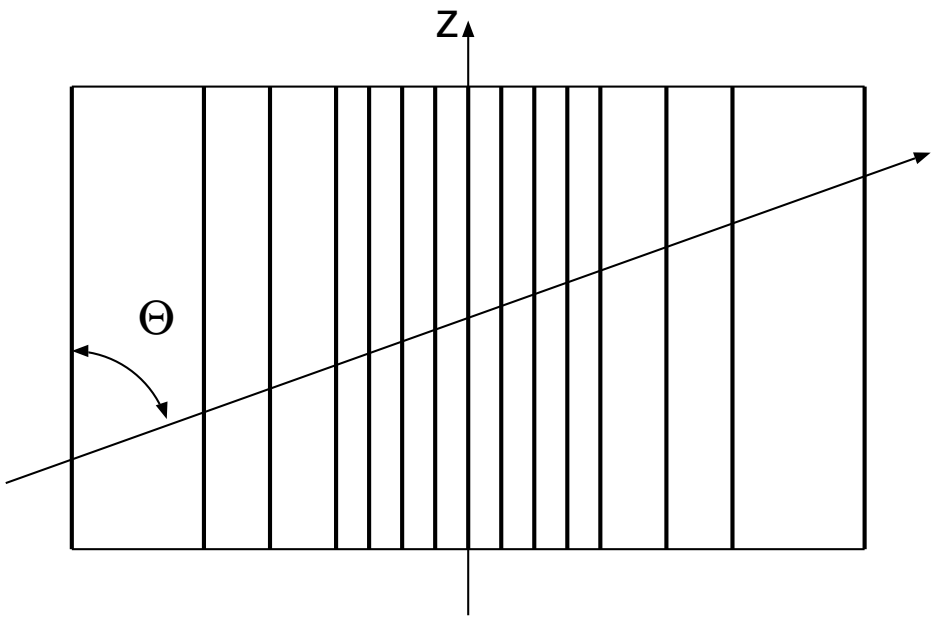

Figure 4.5: Sideview of a tangent plane. It is identical with the case of the plane-parallel media in Fig. 4.2, except for the direction of layers.

4.3 Radiation hydrodynamics solver

The RHD solver calculates the time evolution of the system, e.g., the density, the velocity, the gas internal energy, the radiation energy, and so on.

We present, first, the notations used in this section; t_n is a current time, t_{n+1} is a next time, m_i is the Lagrangian mesh ($i = 1, 2, \cdots, N$), N is the number of the spatial grid points, $A_{i,n}$ is a certain variable A at the position of x_i and the time of t_n, and $\langle A_{i,n} \rangle$ is the mean of A_i between t_n and t_{n+1}. A step-size of the time $\Delta t_n = t_{n+1} - t_n$ is determined by the CFL condition,

$$\Delta t = \nu_{\rm CFL} \min \left(\frac{\Delta x_i}{a_i + |v_i|} \right), \tag{4.15}$$

where $\nu_{\rm CFL}$ is a numerical coefficient about 0.5, and a_i is the sound speed at x_i. If $\nu_{\rm CFL}$ is taken larger than unity, the explicit code becomes unstable numerically.

In the following section, the details of the motion equation solver and the energy equation solver are described. Our code iterates these two solvers alternatively until the consistency between them (see Fig. 4.1) is achieved. Though it is possible to calculate without the iteration, iterations give a better accuracy. The number of the iteration times is usually 1–5 in each time step.

4.3.1 Motion equation solver

The equation of motion, Eq. (3.14), is almost identical with the usual hydrodynamics equation except for a radiation force term, which is the last term in the RHS in Eq. (3.14). The acceleration a_i at any position is calculated by the Eq. (3.14). Various variables are updated as following.

$$v_{i,n+1} = v_{i,n} + \langle a_{i,n} \rangle \Delta t_n, \tag{4.16}$$

$$x_{i,n+1} = x_{i,n} + \langle v_{i,n} \rangle \Delta t_n, \tag{4.17}$$

$$\rho_{i,n+1} = \frac{m_{i+1} - m_i}{V_{i+1,n+1} - V_{i,n+1}}, \tag{4.18}$$

where V_i denotes the volume of the i th cell. When the Cartesian coordinates are employed, the volume is expressed as $V_i = x_i$. In the case of different coordinates, it becomes $V_i = \pi x_i^2$ for the cylindrical coordinates, and $V_i = 4\pi x_i^3/3$ for the spherical coordinates.

4.3.2 Energy equations solver

This part calculates the time evolution of the gas energy, the radiation energy, and the radiative flux from Eqs. (3.17), (3.18), and (3.24). The algorithm used in this part is presented below.

The unknown next time-step variables such as $e_{i,n+1}$ and $E_{i,n+1}$ appear in the RHS terms of the energy equations and the 1st moment equation because we employ the implicit time integration. The equations can be written conceptually as

$$\frac{e_{i,n+1} - e_{i,n}}{\Delta t_n} = \text{function of } e_{i,n+1},\ E_{i,n+1}, \tag{4.19}$$

$$\frac{E_{i,n+1} - E_{i,n}}{\Delta t_n} = \text{function of } e_{i,n+1},\ E_{i-1,n+1},\ E_{i,n+1},\ E_{i+1,n+1}, \tag{4.20}$$

$$F_{i,n+1} = \text{function of } E_{i-1,n+1},\ E_{i,n+1}. \tag{4.21}$$

From Eq. (4.19), $e_{i,n+1}$ can be regarded as a function of $E_{i,n+1}$ as like $e_{i,n+1} = g_i(E_{i,n+1})$. Equation. (4.20) also can be written as

$$f_i(E_{i-1,n+1}, E_{i,n+1}, E_{i+1,n+1}, e_{i,n+1}) = 0, \tag{4.22}$$

which are N-dimensional simultaneous equations ($i = 1, \cdots, N$). Since the $e_{i,n+1}$ are non-linear in the function f_i, the simultaneous equations are solved by the Newton-Raphson method.

$$J_{ij} \begin{pmatrix} \delta E_1 \\ \delta E_2 \\ \vdots \\ \delta E_N \end{pmatrix} = - \begin{pmatrix} f_1 \\ f_2 \\ \vdots \\ f_N \end{pmatrix}, \tag{4.23}$$

where J_{ij} is a Jacobian matrix defined as

$$J_{ij} \equiv \frac{\partial f_i}{\partial E_{j,n+1}} \begin{cases} \neq 0 & \text{for } j = i-1, i, i+1 \\ = 0 & \text{otherwise} \end{cases}, \tag{4.24}$$

therefore, J_{ij} is a tridiagonal matrix.

4.4 Test problems

In this section, we present the test problems, which have the analytic solutions, to check the validity of our numerical code. Each part of the source code is tested individually. The hydrodynamics test is given in § 4.4.1, the energy equations solver test is given in § 4.4.2, and the RT solver test is given in § 4.4.3.

4.4.1 Blast wave

We consider that conditions in which the high energy is released at a point in the uniform media. A wave originated by the released energy spreads outwardly with compressing the surrounding gas to form a shock. The analytic solution of this problem is known as the Sedov's solution (see Landau & Lifshitz [12]). The calculations of such the point explosion problem were carried out as a hydrodynamics test using the spherical coordinates. The adiabatic process is assumed so the radiative transfer equation is not solved.

Numerical results as well as the analytic solutions are shown in Figs. 4.6–4.8. It can be seen that the numerical results have a good agreement with the analytic solutions.

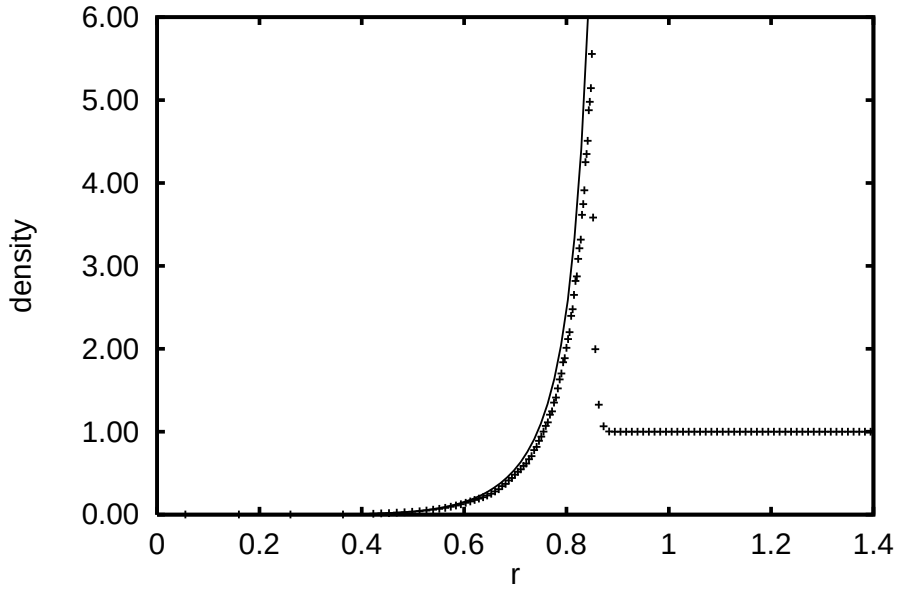

Figure 4.6: The result of the Sedov problem. The density distribution is displayed by crosses. A solid curve denotes the analytic solution.

4.4.2 Static radiative diffusion

The time evolution of the energy distribution in a static and optically thick medium is simulated. This calculation checks only the energy equations solver. There is no need to solve the equation of motion since the medium is static, and there is no need to solve the radiative transfer equation, since the Eddington factors become $f_{rr} = f_{zz} = f_{\Phi\Phi} = 1/3$ and constant.

We suppose that the media are static and optically thick and that the radiation energy E is much greater than the gas energy $\rho e_{\rm gas}$. What is the

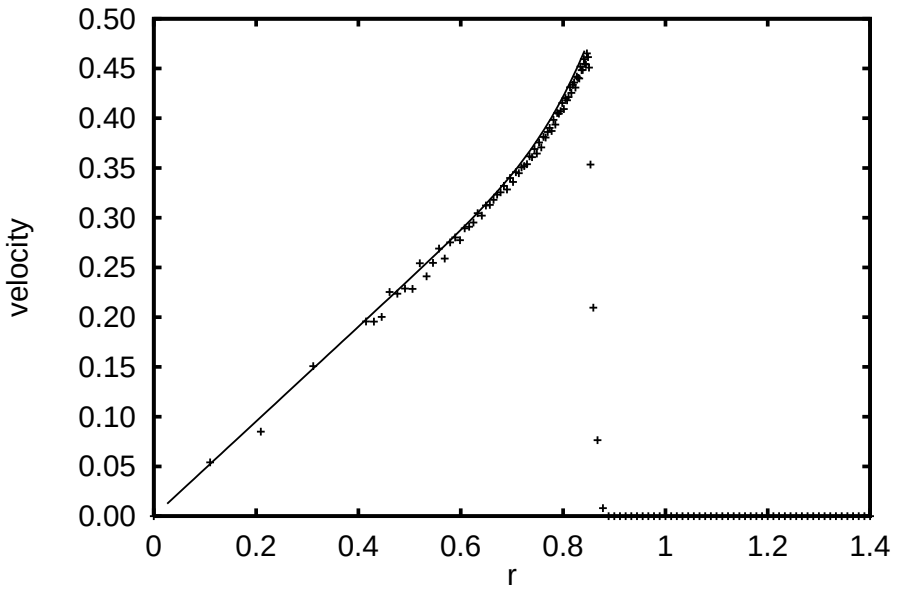

Figure 4.7: The result of the Sedov problem. The velocity distribution is displayed by crosses with a solid curve denoting the analytical solution.

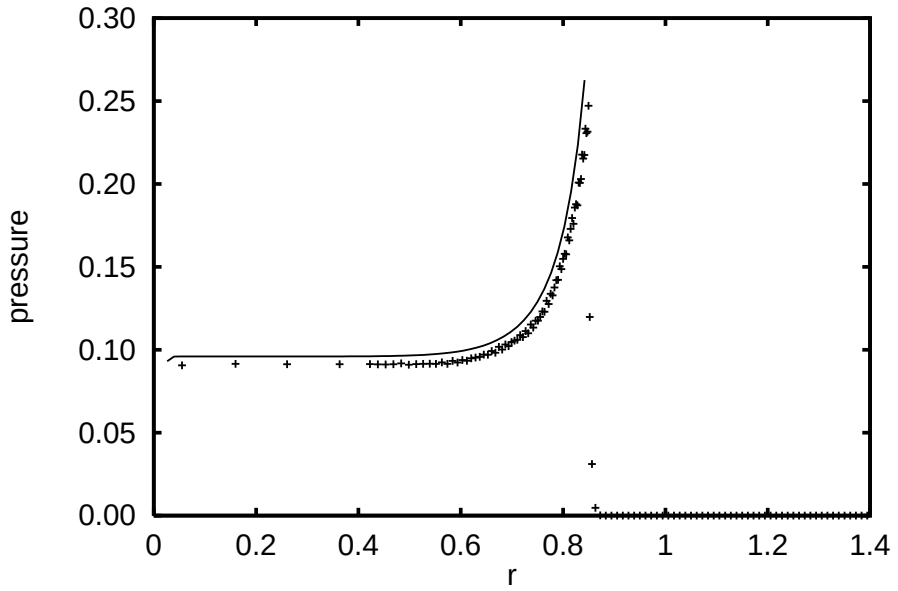

Figure 4.8: The result of the Sedov problem. The pressure distribution is shown.

meanings of the last condition? In the thick media, $E = aT^4$ is established, thus,

$$E \gg \rho e_{\rm gas} \Longrightarrow \frac{T^3}{\rho} \gg \frac{k_B}{(\gamma - 1)\mu m_{\rm H} a}. \tag{4.25}$$

The above condition is satisfied in the low density and high temperature media. Though the optically thick media in spite of low density may seem to be strange, it is possible if the spatial scale is large enough. Under these conditions, the basic equations are reduced to a radiative diffusion equation,

$$\frac{\partial E}{\partial t} = \nu \nabla^2 E, \tag{4.26}$$

where ν is a constant $\nu = c/(3\chi)$.

We put the energy distribution which has initially a Gaussian peak in the medium. Then it is expected that the peak of the energy distribution will be smoothed out gradually. The energy distribution at $t = 0$ is assumed by a following equation,

$$E(r, 0) = E_0 \exp\left[-(r/L)^2\right], \tag{4.27}$$

where L is a characteristic length. It is convenient to use the normalized variables defined by

$$r' = r/L, \quad t' = \nu t/L^2, \quad E' = E/E_0. \tag{4.28}$$

Then, the analytic solution at any time in the cylindrical coordinates is given by

$$E'(r', t') = \frac{1}{4t' + 1} \exp\left[-\frac{r'^2}{4t' + 1}\right], \tag{4.29}$$

and

$$F' = -\frac{\partial E'}{\partial r'}. \tag{4.30}$$

The results which show a good agreement with the analytic solutions are presented in Fig. 4.9 and Fig. 4.10, where the energy and the flux at $t' = 0$, $t' = 1/8$, $t' = 3/8$, and $t' = 1/2$ are plotted. The number of all steps is only 8 when the step-size of time is fixed to $\Delta t' = 1/16$. In spite of the rough step-size, the results are good. The calculations with more rough step-size $\Delta t' = 1/8$ also performed, then these results slightly depart from the exact solutions.

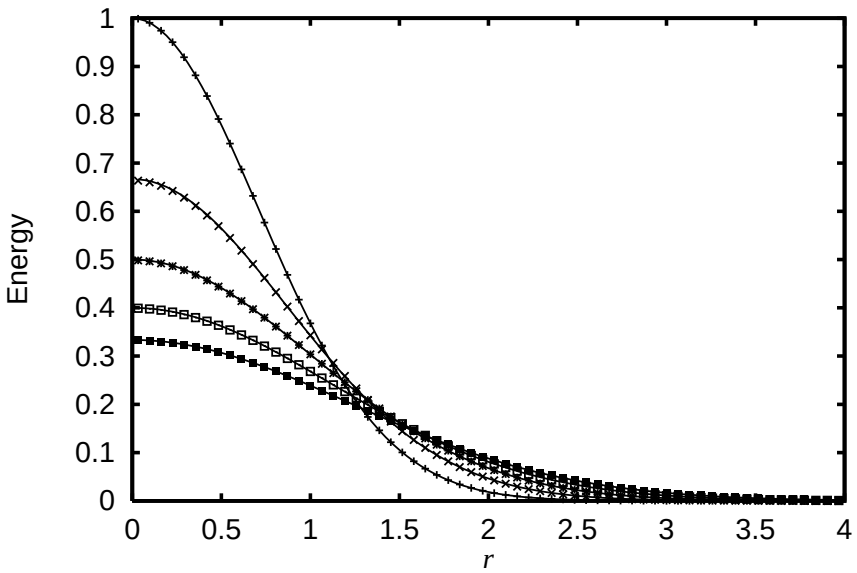

Figure 4.9: Results of a static radiative diffusion test. The radiative energy distributions are shown at the time $t' = 0$, $1/8$, $1/4$, $3/8$, and $1/2$. Crosses represent the numerical results and the solid curves correspond the analytical solutions.

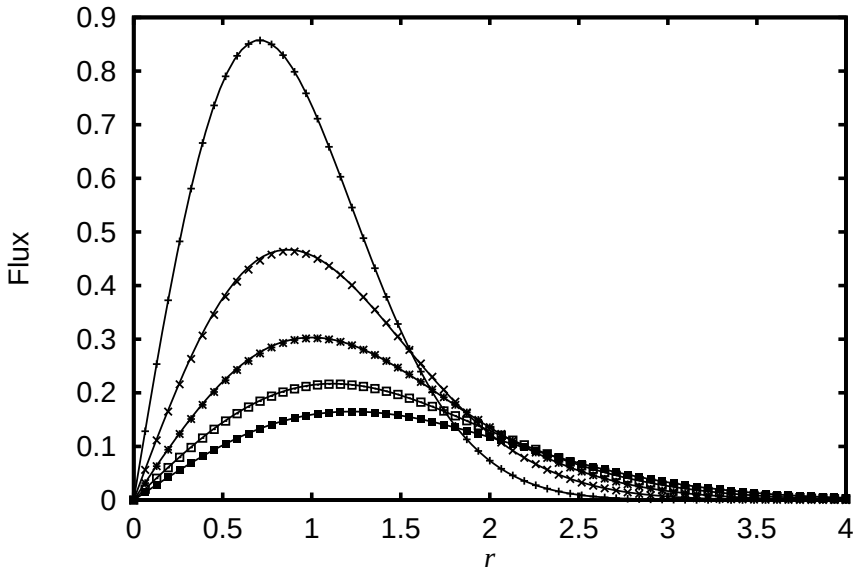

Figure 4.10: Flux distributions for the same conditions in Fig. 4.9.

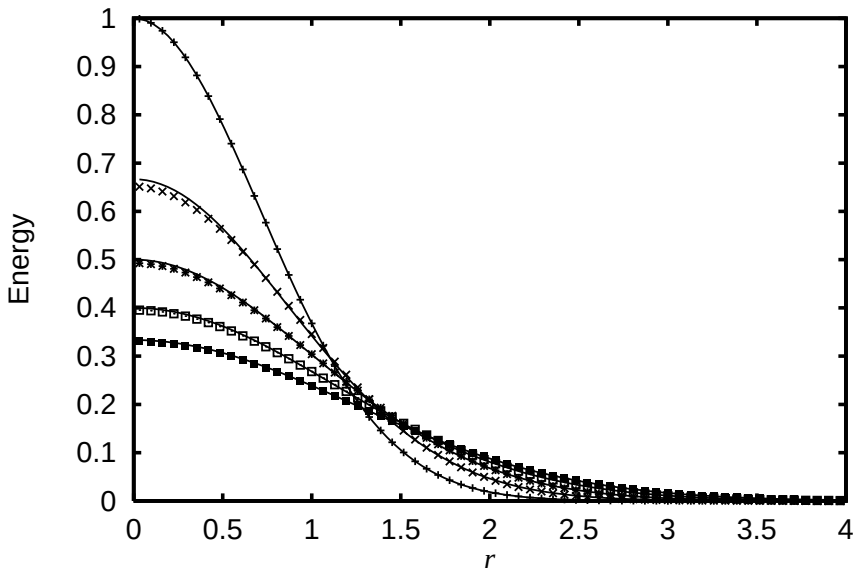

Figure 4.11: Radiation energy distributions at the $t' = 0$, 1/8, 1/4, 3/8, and 1/2. The step-size of time is taken to be 1/8.

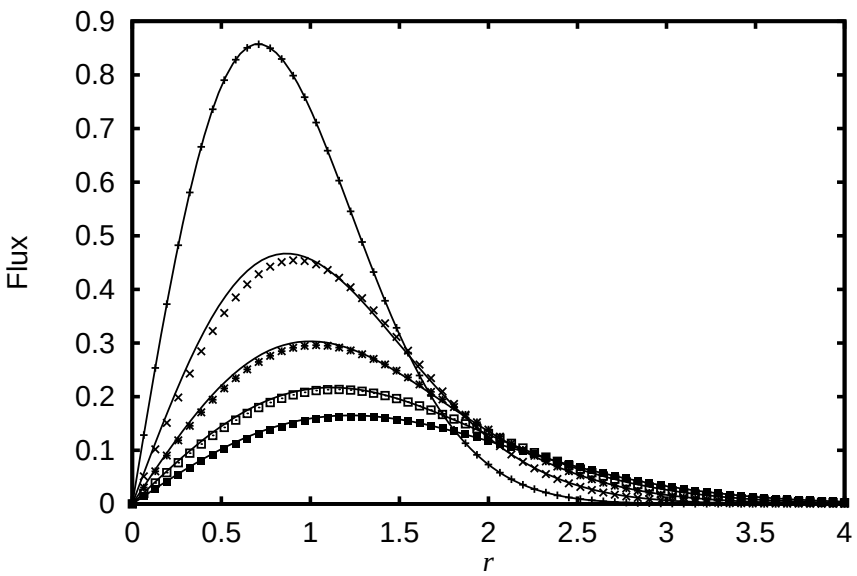

Figure 4.12: Flux distributions for the same conditions in Fig. 4.11.

4.4.3 RT solver test

We carried out a test for the RT solver. In this test, we concentrate on the precision for the azimuthal angle, which depend strongly on the distribution of the tangent planes.

We suppose that an optically thick cylindrical light source is located, and the space around it is vacuum (see Fig. 4.13). Then we calculate the Eddington Factors around the cylinder by solving the RT equation. We

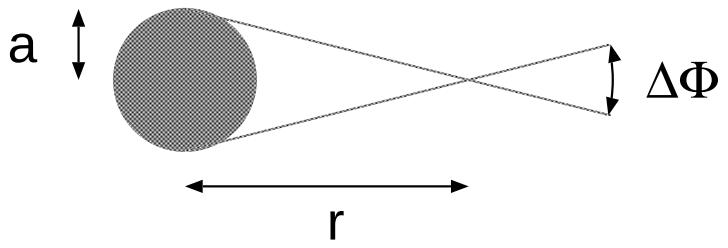

Figure 4.13: The left circle denotes the cylindrical light source (its radius is a) which are viewed from the axial direction. The angle of $\Delta\Phi$ is derived from $\sin(\Delta\Phi/2) = a/r$. The intensity is non-zero only for $|\Phi| \leq \Delta\Phi/2$.

change the number of tangent plane and examine the precision of numerical solutions comparing to the analytic solutions. The analytic solution of the Eddington factor f_{rr} is given as

$$f_{rr} = \begin{cases} \frac{1}{3}\left[1 + \frac{\xi(1-\xi^2)^{1/2}}{\arcsin\xi}\right] & (0 < \xi \leq 1) \\ \frac{1}{3} & (\xi > 1) \end{cases}, \tag{4.31}$$

where $\xi = a/r$.

Results are shown in figures 4.14 and 4.15. We can see that the precision for the azimuthal angle in the RT solver becomes better as the number of the tangent plane increases.

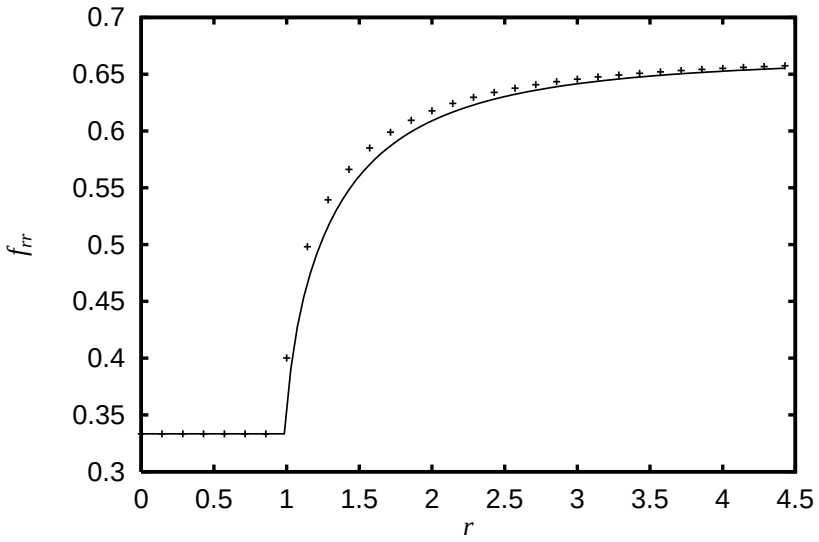

Figure 4.14: A solid curve denotes the analytic solution given by Eq. 4.31, and points are the results by the RT solver. The number tangent plane in this calculation is 31.

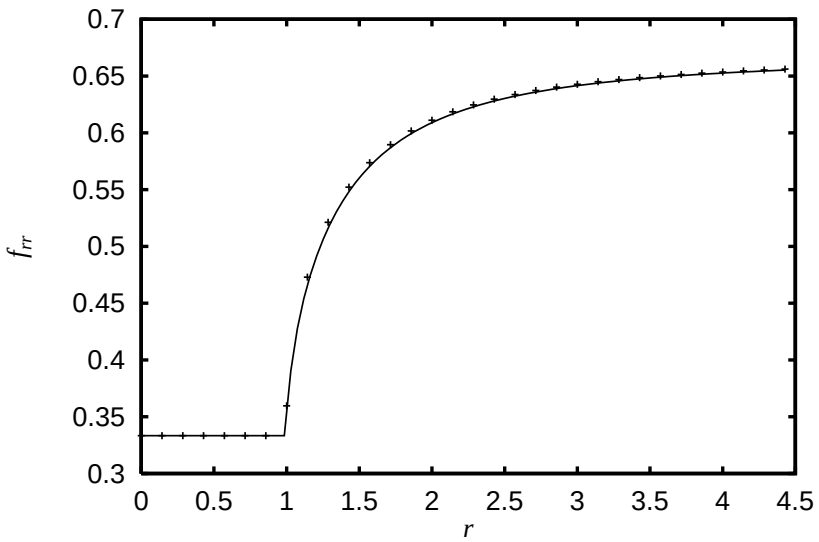

Figure 4.15: The number of tangent plane is 79. The results show the better accuracy than that of 31 tangent plane case.

Chapter 5

Numerical Results

We performed the RHD simulations of gravitationally collapsing filaments under several conditions. Physical parameters for the typical condition are $\rho_{\rm init} = 10^{-18}\,{\rm g\,cm^{-3}}$, $\mu = 2.3$, $h = \sqrt{2}$, $\kappa_{10} = 0.02\,{\rm g^{-1}\,cm^2}$, and $\beta = 2$. We take these parameters fixed except for special cases. The initial temperatures $T_{\rm init}$ are variable in the range of 8–60 K. The incident radiation $I = B(T_{\rm init})$ is included only for the standard model and the flat density model.

In the numerical code, all the variables are normalized by characteristic values, which are the initial density $\rho_{\rm init}$, the initial scale height $H(\rho_{\rm init}, T_{\rm init})$, and the sound speed at the initial temperature. In this and later chapters, results for which no unit is specified are presented in the normalized unit.

The characteristic values are following:

$$H_0 \approx 3.9 \times 10^3 \left(\frac{\rho_{\rm init}}{10^{-18}\,{\rm g\,cm^{-3}}}\right)^{-1/2} \left(\frac{T_{\rm init}}{10\,{\rm K}}\right)^{1/2} {\rm AU}, \tag{5.1}$$

$$v_0 \approx 0.19 \left(\frac{T_{\rm init}}{10\,{\rm K}}\right)^{1/2} {\rm km\,s^{-1}}, \tag{5.2}$$

$$t_0 \equiv \frac{H_0}{v_0} \approx 1.0 \times 10^5 \left(\frac{\rho_{\rm init}}{10^{-18}\,{\rm g\,cm^{-3}}}\right)^{-1/2} {\rm yr}, \tag{5.3}$$

$$\Gamma_0 \equiv \frac{v_0^2}{t_0} \approx 1.2 \times 10^{-4} \left(\frac{\rho_{\rm init}}{10^{-18}\,{\rm g\,cm^{-3}}}\right)^{1/2} \left(\frac{T_{\rm init}}{10\,{\rm K}}\right) {\rm erg\,g^{-1}\,s^{-1}}. \tag{5.4}$$

5.1 Standard model

Results of the standard model are presented in this section. Also, some related figures are displayed in Appendix B.

5.1.1 Density and velocity

As described in Chapter 2, the initial density distribution of the filaments is given by

$$\rho(r) = \rho_{\rm init} \left[1 + \left(\frac{r}{hH(\rho_{\rm init}, T_{\rm init})}\right)^2\right]^{-2}. \tag{5.5}$$

The parameter h is taken to be larger than unity. The filaments are also assumed to be static at an initial time $t = 0$. The density distributions of the collapsing filament are plotted in Fig. 5.1. The density in the inner region evolves drastically. On the other hand, the outer envelope does not change significantly. The time evolution of the central density ρ_c is plotted in Fig. 5.2. Though the filaments are non-equilibrium at the initial time as long as $h \neq 1$, the central region approaches the equilibrium after a while.

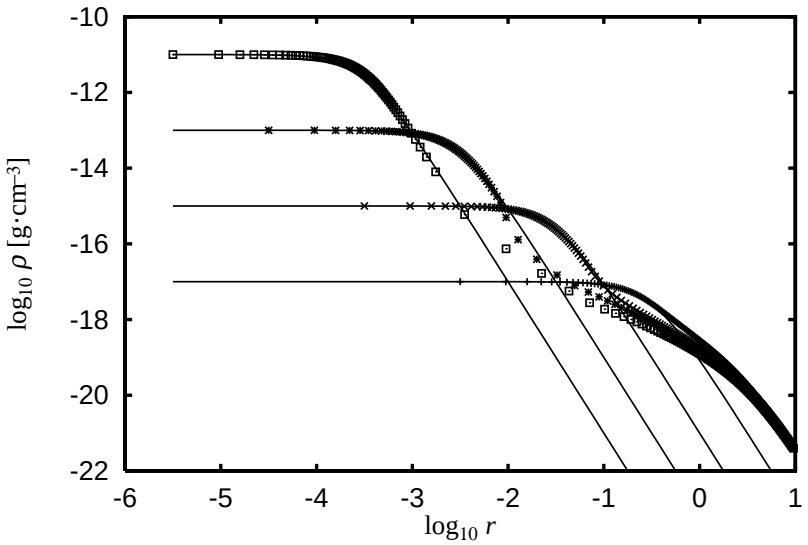

Figure 5.1: Each set of points denotes the density distribution ($T_{\rm init} = 10$ K and $h^2 = 2$) at the time, $t = 0.9112$, $t = 1.174$, $t = 1.217$, and $t = 1.301$ (see also Fig. 5.2). Solid curves denote the equilibrium distributions $\rho_{\rm eq}(r)$ for $\rho_c = 10^{-17}$, 10^{-15}, 10^{-13}, and $10^{-11}\,{\rm g\,cm^{-3}}$, see Eq. (5.6).

Thus, the density distribution near the center can be approximated by

$$\rho_{\rm eq}(r) = \rho_c \left[1 + \left(\frac{r}{H(\rho_c, T)}\right)^2\right]^{-2}, \tag{5.6}$$

where ρ_c is the central density.

The equilibrium density distribution $\rho_{\rm eq}$ given by Eq. (5.6) has no information as to time evolution. On the other hand, a similarity solution (Kawachi & Hanawa 1998 [11]) can inform us the time evolution of collapsing filaments, approximately. The similarity solution is given as

$$\rho_{\rm SS}(r,t) = \frac{1}{2\pi G'(t-t_0)^2}\, \varrho\left(\frac{r}{|t-t_0|}\right), \tag{5.7}$$

$$\varrho(x) = \varrho_0 \left(1 + \frac{\varrho_0 x^2}{4}\right)^{-2}, \tag{5.8}$$

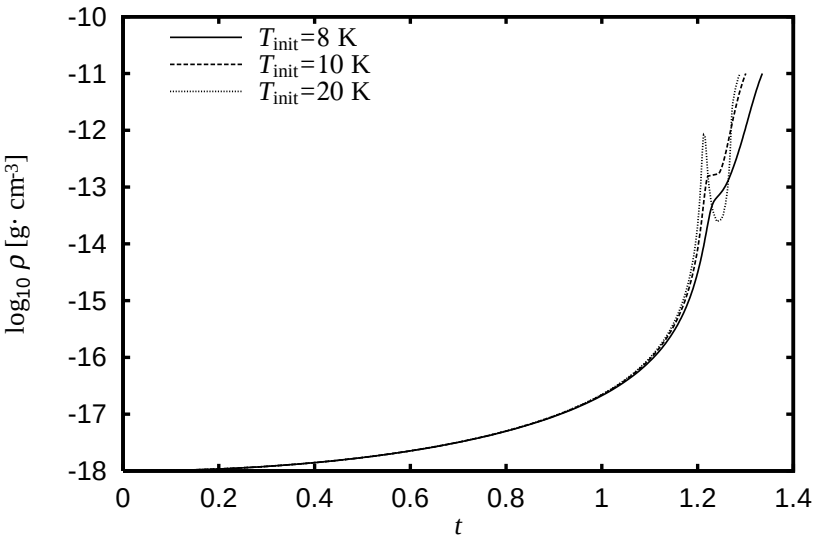

Figure 5.2: The time evolution of central densities for several initial temperatures in the case of $h^2 = 2$ model.

$$v_{\rm SS}(r,t) = -\frac{r}{|t-t_0|}. \tag{5.9}$$

Notice that all the variables in these equations are normalized, e.g., the gravity constant G' in Eq. (5.7) is equal to $2/\pi$.

Though the similarity solution is adequate only for $0 < \gamma_p < 1$, it can approximate the time evolution of the RHD calculation as long as the filaments are nearly isothermal. It is useful to analyze numerical results. Comparisons between the results of the RHD calculations and the similarity solution are presented in Figs. 5.3–5.6, and these figures show the agreement. The parameters which appear in the similarity solution (t_0 and ϱ_0) depend on h (see Table. 5.1). However, we must keep in mind that the approximation becomes inaccurate as the parameter h becomes greater than unity. Indeed, the case of $h^2 = 2$ is not accurate as the case of $h^2 = 1.2$.

h^2	t_0	ϱ_0
1.2	2.844	21.2
1.4	1.877	16.0
2.0	1.194	11.6
4.0	0.8381	6.76

Table 5.1: The parameters in the similarity solution. They are determined by some numerical experiments.

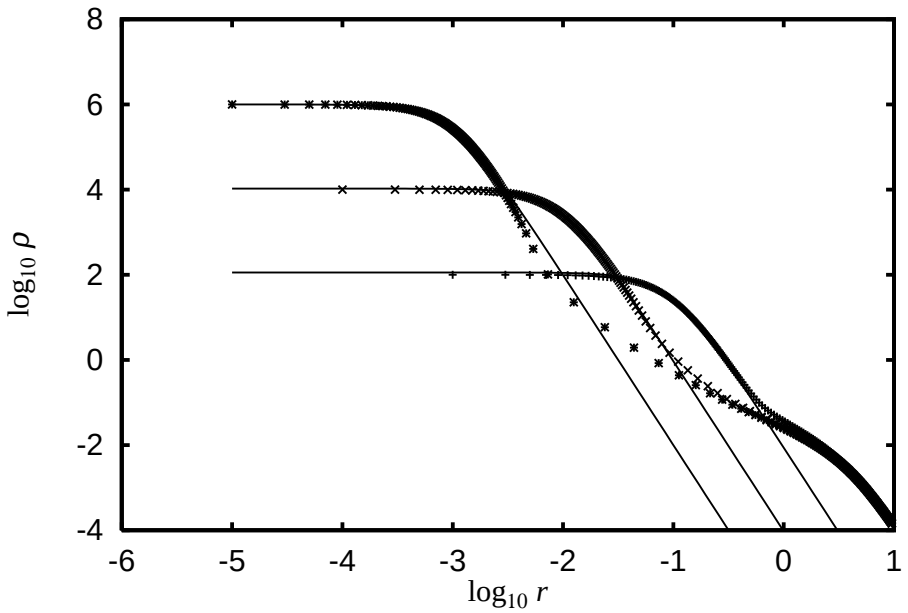

Figure 5.3: The density distributions for $T_{\rm init} = 60$ K and $h^2 = 1.2$ model. Solid curves denote the similarity solutions $\rho_{\rm SS}$ of $t_0 = 2.844$ and $\varrho_0 = 21.2$. Notice that this figure is similar to Fig. 5.1, but the plotted function as solid curves is different between Fig. 5.1 and this figure.

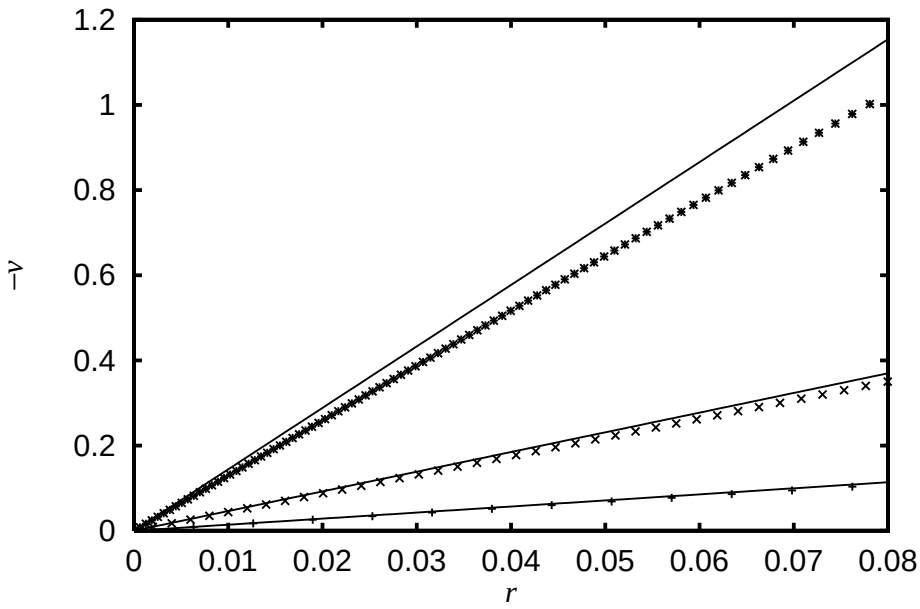

Figure 5.4: The velocity distributions near the center in the case of $T_{\rm init} =$ 60 K and $h^2 = 1.2$ model. Solid lines denote the similarity solutions $v_{\rm SS}$ of $t_0 = 2.844$ and $\varrho_0 = 21.2$.

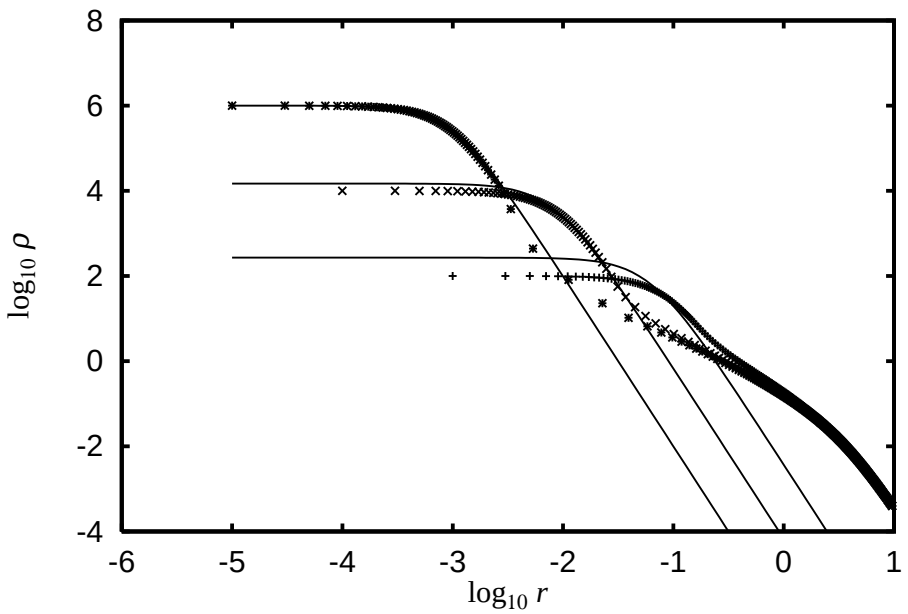

Figure 5.5: The density distributions in the case of $T_{\rm init} = 60$ K and $h^2 = 2.0$ model. Solid curves denote the similarity solutions $\rho_{\rm SS}$ of $t_0 = 1.194$ and $\varrho_0 = 11.6$.

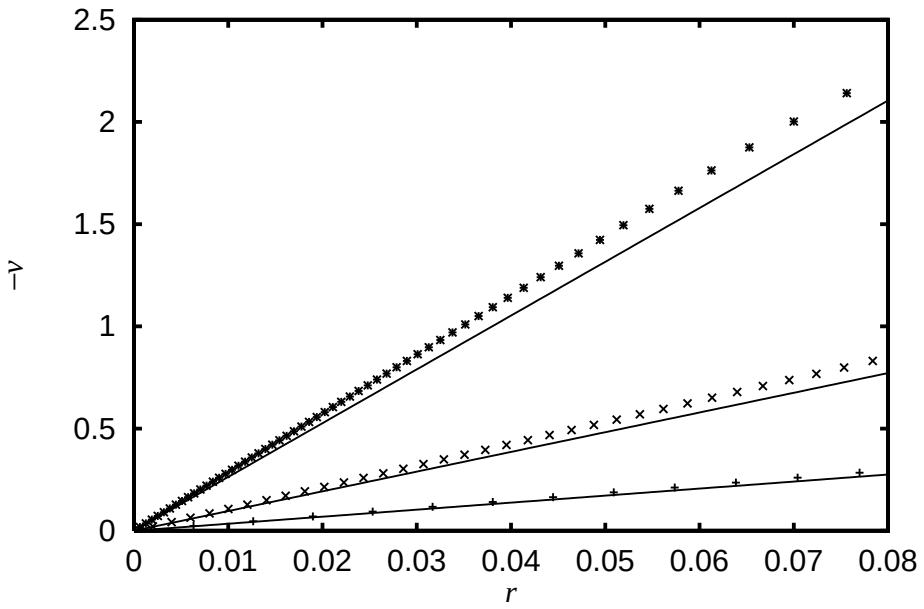

Figure 5.6: The velocity distributions near the center in the case of $T_{\rm init}$ = 60 K and $h^2 = 2.0$ model. Solid lines denote the similarity solutions $v_{\rm SS}$ of $t_0 = 1.194$ and $\varrho_0 = 11.6$.

5.1.2 Gas temperature

The gas temperature distributions at $t = 1.10$ and $t = 1.20$ are plotted in Fig. 5.7 and Fig. 5.8. These figures show that the evolution of the gas temperature distribution has a strong dependence on the initial temperature, while the evolution of the density and velocity distribution has merely a weak dependence.

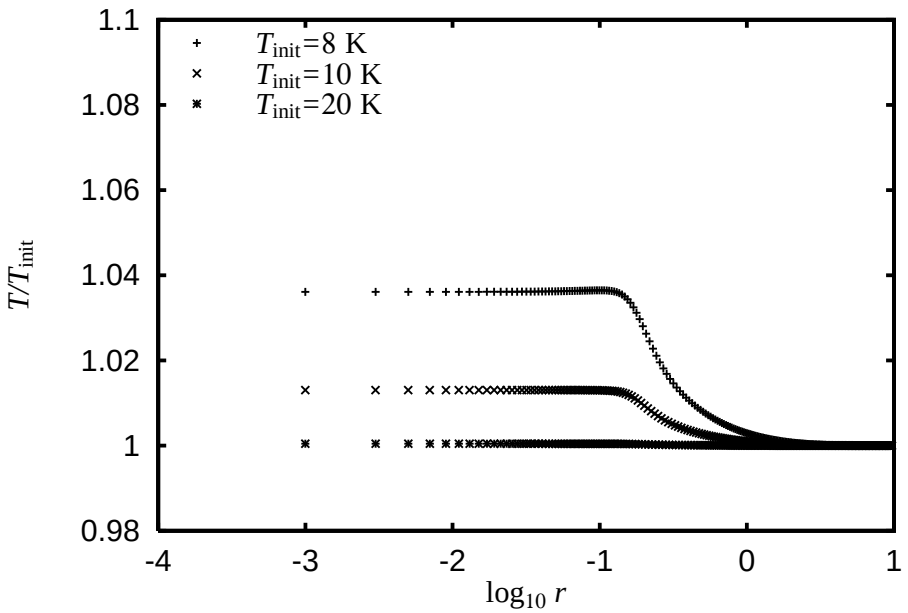

Figure 5.7: Gas temperature distributions in unit of $T_{\rm init}$ for $h^2 = 2$ model are plotted for the cases of $T_{\rm init} = 8,\ 10,\ 20$ K at the time of $t = 1.10$. See also Fig. 5.8.

The relation between the gas temperature and the central density during the gravitational collapse for several initial temperatures are displayed on T–ρ plane (see Fig. 5.9). The T–ρ plane diagrams are most meaningful in our study.

The tracks in the diagram are the loci of the density and gas temperature

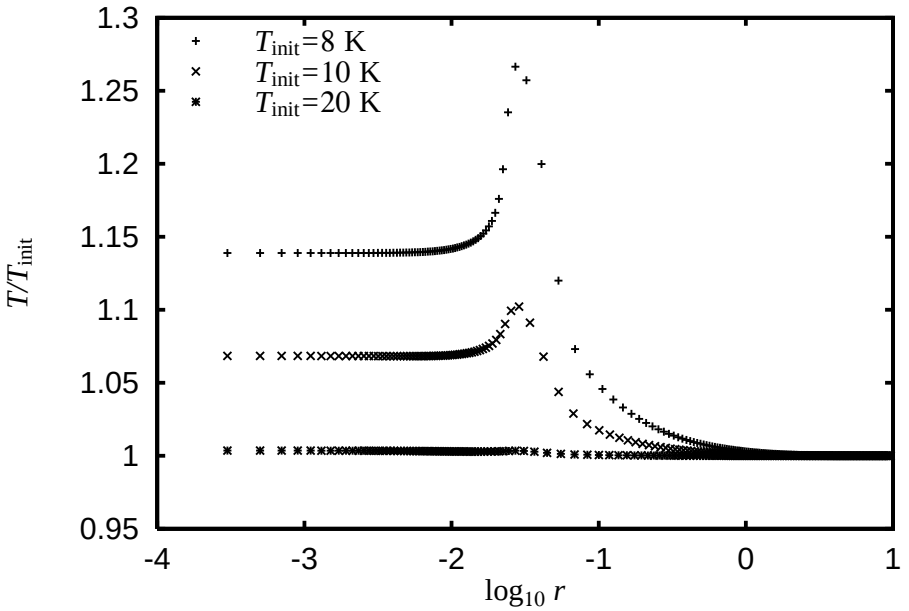

Figure 5.8: Gas temperature distributions at the time of $t = 1.20$.

at the center. At the initial time, the state situates at the lowest point of each track on the diagram. The tracks rise up vertically during the isothermal collapse and turn to the right when the isothermality breaks down. Loops seen on the tracks of $T_{\rm init} = 20, 40, 60$ K in Fig. 5.9 correspond to bounces of the collapse. We will discuss some interesting features which are shown in the diagram in the next chapter.

5.1.3 Heating and cooling rates

The heating and cooling rates, which are given in Eqs. (3.19)–(3.23), have important meanings for the RHD calculations. Thus, the evolution of each rate is shown in Figs. 5.10–5.13. These figures generally show that the compressional heating rate $\Gamma_{\rm dyn}$ is much smaller than $\Lambda_{\rm dust}$ in an early phase, but it becomes an important heating source in a later phase.

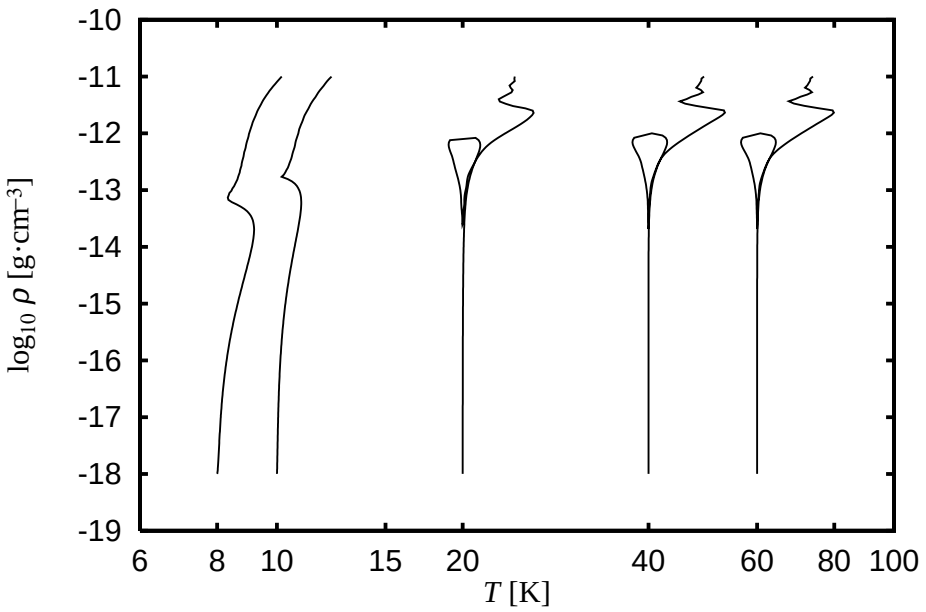

Figure 5.9: The T–ρ plane diagram. The evolutional tracks for several initial temperatures are plotted. Initial temperatures are $T_{\rm init} = 8, 10, 20, 40, 60\,{\rm K}$ for each. The h-parameter is taken as $h^2 = 2$.

The compressional heating rate $\Gamma_{\rm dyn}$ is given as

$$\Gamma_{\rm dyn} \equiv -\frac{p}{\rho}\nabla\cdot\boldsymbol{v} = -\frac{p}{\rho}\left(\frac{\partial v}{\partial r}+\frac{v}{r}\right). \tag{5.10}$$

From the equation (5.9), the normalize $\Gamma_{\rm dyn}$ can be expressed as

$$\Gamma'_{\rm dyn} = \frac{2}{|t-t_0|} = \frac{4}{\varrho_0^{1/2}}\rho_c^{1/2}. \tag{5.11}$$

However, the relation of $\Gamma'_{\rm dyn} \propto \rho_c^{1/2}$ is not completely satisfied since the actual evolution of the density and velocity distributions are slightly different from the similarity solution. We define the coefficient α as

$$\alpha = \Gamma'_{\rm dyn}/\rho_c^{1/2}. \tag{5.12}$$

This is evaluated at the center of the filament. Values of α are plotted in Fig. 5.15 for several h parameter models. Though the coefficient α is not a constant exactly, we regard the α as a constant for simplicity by averaging the values over the range from $10^{-17}\,{\rm g\,cm^{-3}}$ to $10^{-13}\,{\rm g\,cm^{-3}}$. The averaged values for some h are plotted in Fig. 5.16. The dependence can be fitted as $\alpha = 1.9\sqrt{h^2-1}$.

5.1.4 Gravity and pressure forces

The distributions of the gravity and the pressure gradient force are plotted in Figs. 5.17–5.20. We can see that two forces approach each other and the force balance is realized in an inner region.

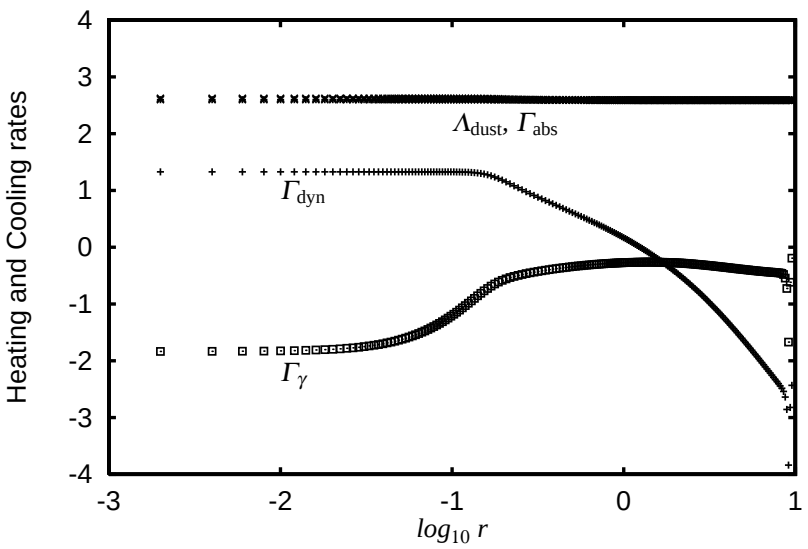

Figure 5.10: The heating and cooling rates (per unit mass) in the case of $T_{\rm init} = 10$ K at the stage of $\log_{10}(\rho_c/\rho_{\rm init}) = 2$. The dust cooling rate $\Lambda_{\rm dust}$ and the radiative absorption rate $\Gamma_{\rm abs}$ are dominant with the balance between $\Lambda_{\rm dust}$ and $\Gamma_{\rm abs}$.

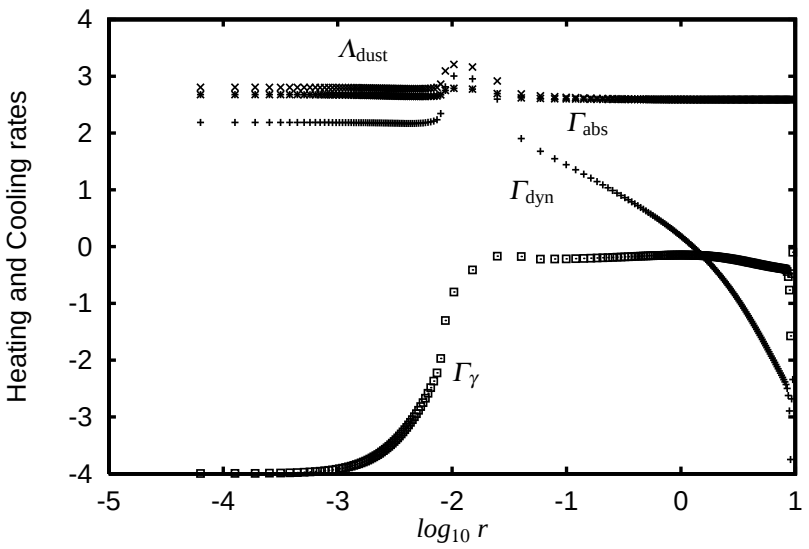

Figure 5.11: The same as Fig. 5.10 except for $\log_{10}(\rho_c/\rho_{\rm init}) = 5$. The compressional heating rate $\Gamma_{\rm dyn}$ near the center becomes the same order to $\Lambda_{\rm dust}$. The balance between $\Lambda_{\rm dust}$ and $\Gamma_{\rm abs}$ is lost near the center, especially at $\log_{10} r \sim -2$.

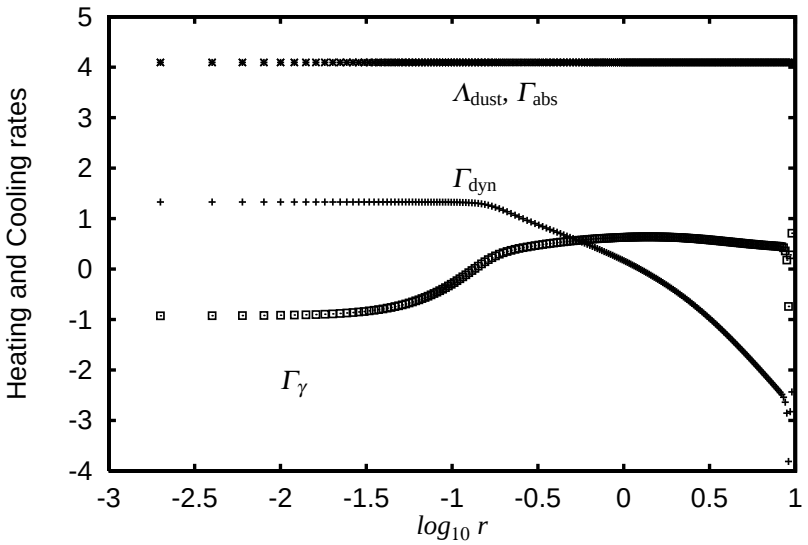

Figure 5.12: The heating and cooling rates in the case of $T_{\rm init} = 20$ K at the stage of $\log_{10}(\rho_c/\rho_{\rm init}) = 2$.

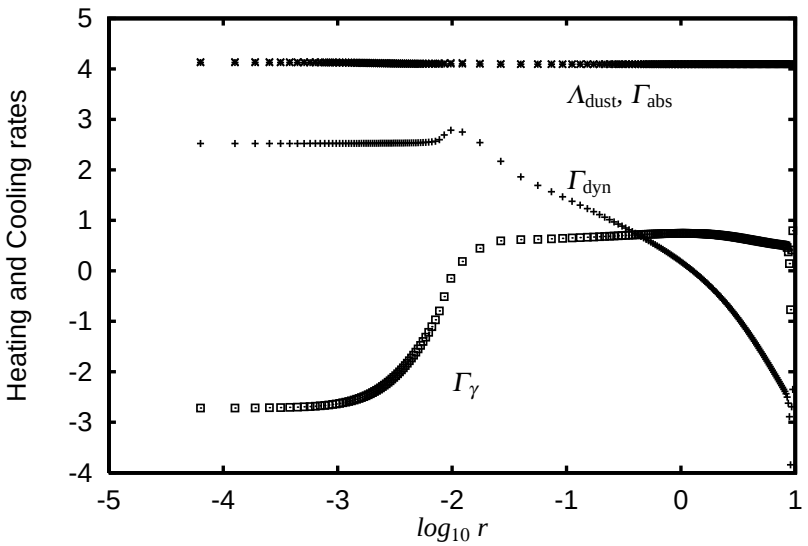

Figure 5.13: The same as Fig. 5.12 except for $\log_{10}(\rho_c/\rho_{\rm init}) = 5$.

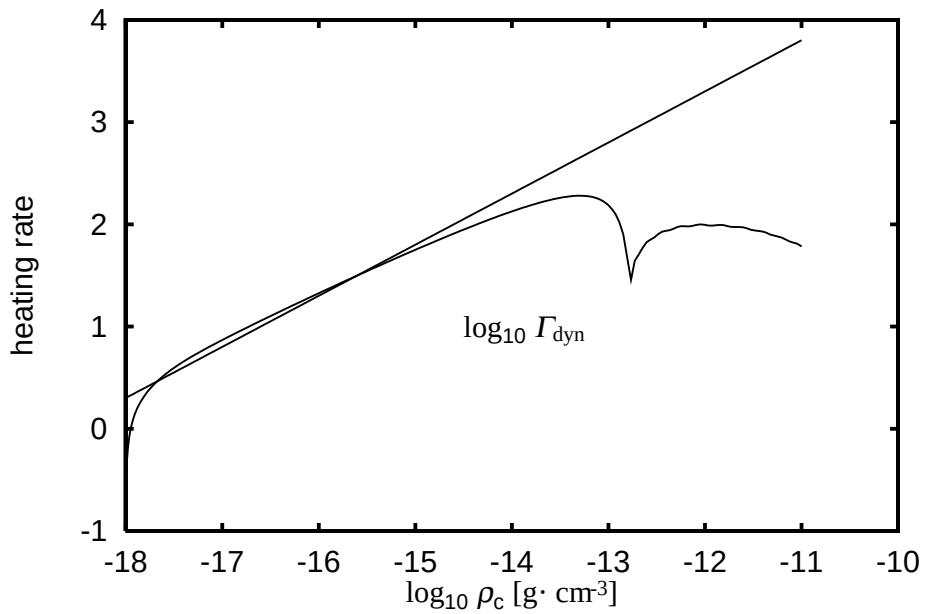

Figure 5.14: The compressional heating rate at the center in the case of $T_{\rm init} = 10$ K is plotted against the central density. A solid line represents an approximated value given by the Eq. (5.12) with $\alpha = 2$. The $\Gamma_{\rm dyn}$ begins to decrease at the onset of a bounce about $10^{-13} - 10^{-12}\,{\rm g\,cm^{-3}}$.

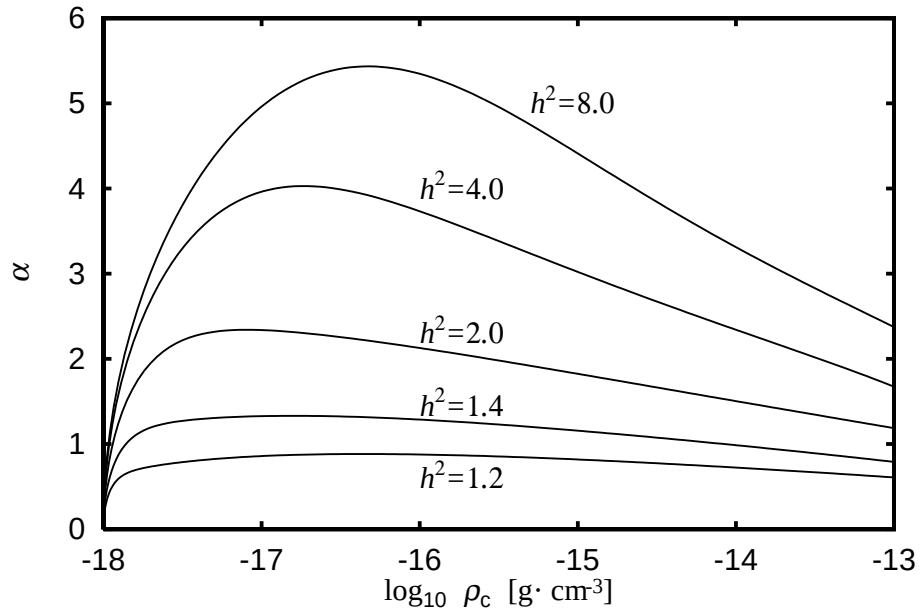

Figure 5.15: The coefficient α defined by Eq. (5.12).

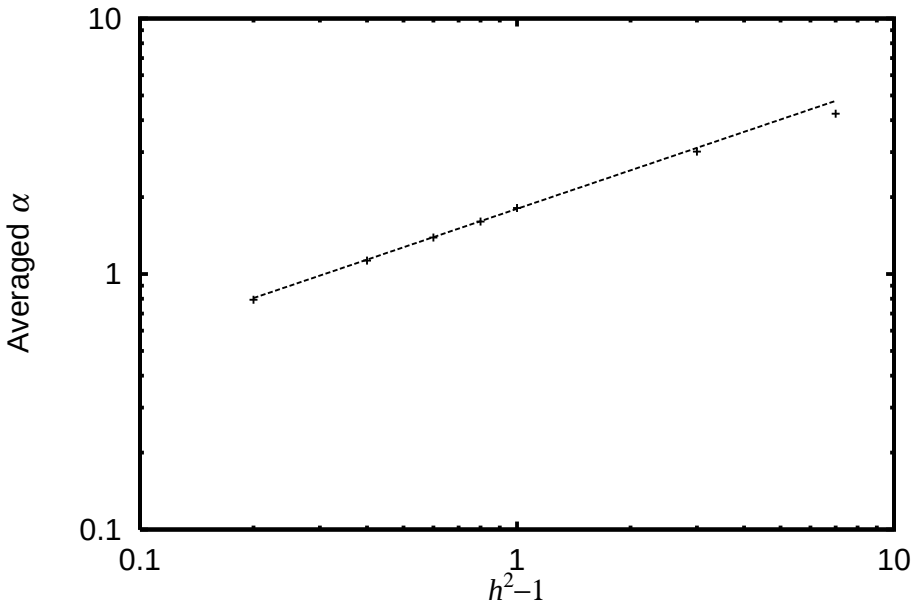

Figure 5.16: Averaged α as a function of the parameter h. The averaged α can be fitted as $\alpha = 1.9\sqrt{h^2 - 1}$.

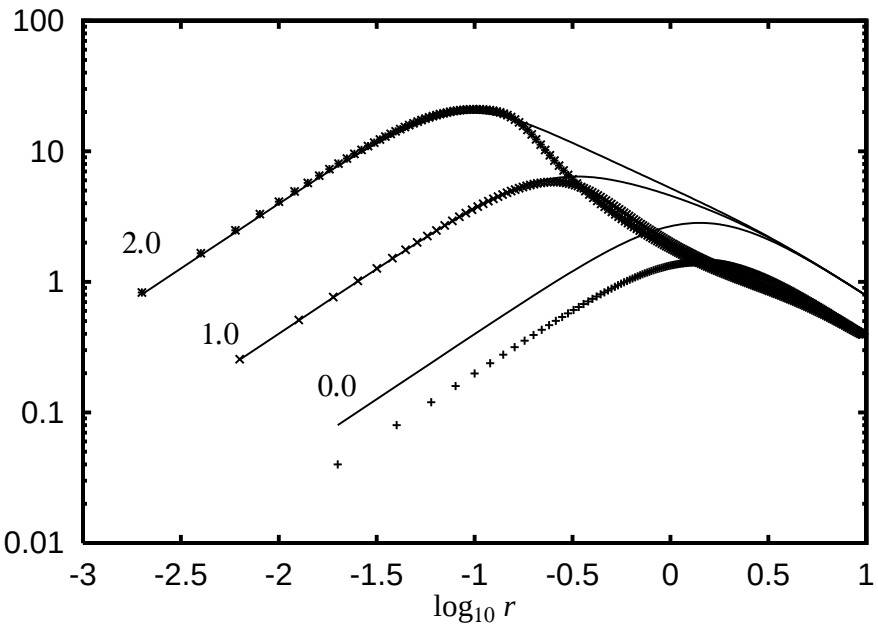

Figure 5.17: Solid curves denote $|g_r|$ and sets of points denote $-\frac{1}{\rho}\frac{dp}{dr}$ in the case of $h^2 = 2.0$. Numbers in the figure, 0.0, 1.0, and 2.0, denote $\log_{10}(\rho_c/\rho_{\rm init})$ at that time.

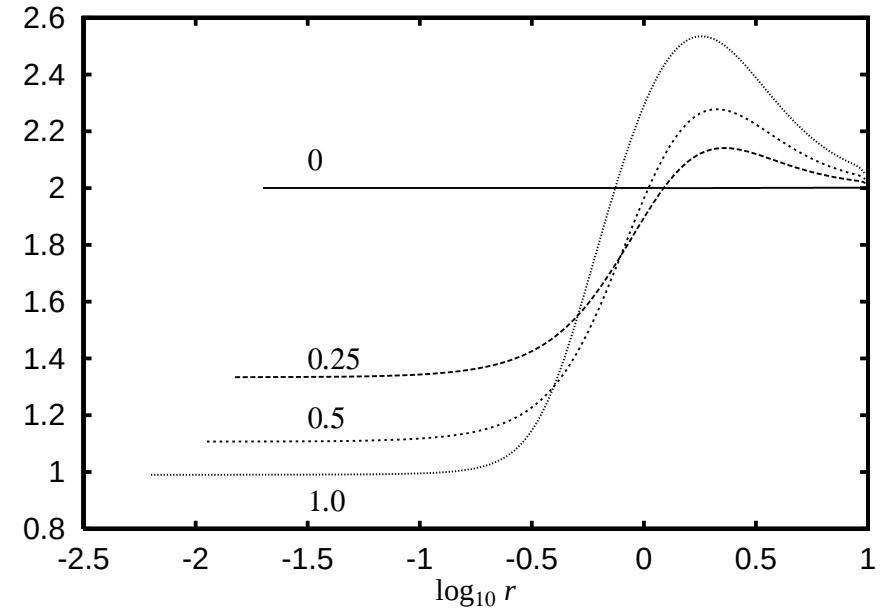

Figure 5.18: Ratio of $|g_r|$ to $-\frac{1}{\rho}\frac{dp}{dr}$ in the case of $h^2 = 2.0$. Numbers in the figure denote $\log_{10}(\rho_c/\rho_{\rm init})$ at that time.

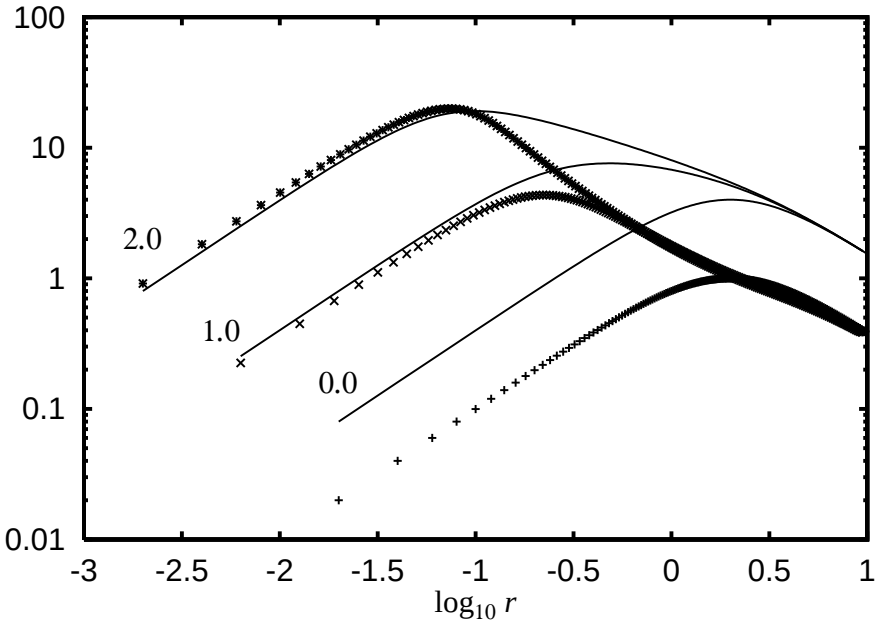

Figure 5.19: The same as Fig. 5.17 except for $h^2 = 4.0$.

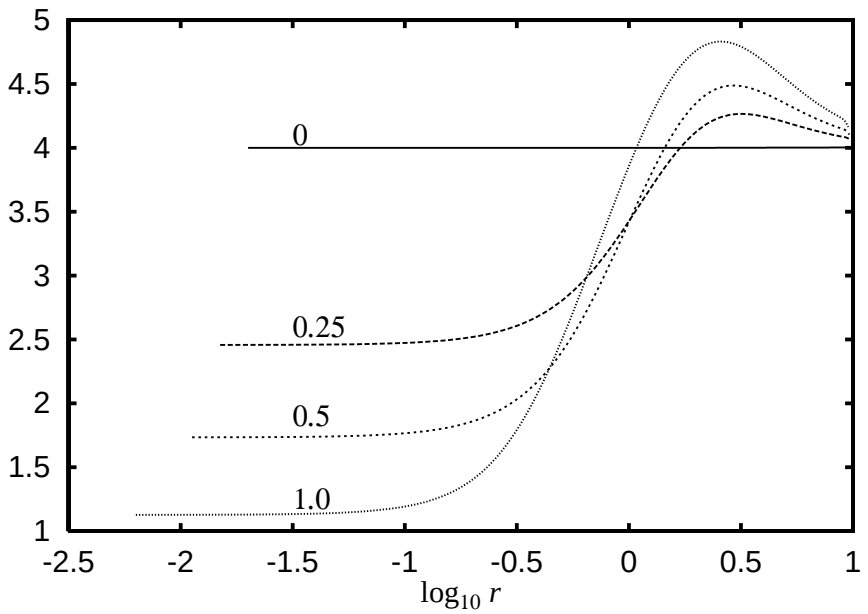

Figure 5.20: The same as Fig. 5.18 except for $h^2 = 4.0$.

5.1.5 Optical depth

The optical depth is an important measure for the efficiency of the radiative transfer. Thus, it is useful to obtain an analytic expression of the optical depth of a filament. Fortunately, the density distribution of filaments is very close to the equilibrium distribution $\rho_{\rm eq}$, as seen in Fig. 5.1. Therefore, the optical depth τ can be obtained as a function of the central density ρ_c,

$$\begin{aligned} \tau &\equiv \int_0^\infty \kappa_P \rho(r)\, dr \\ &\simeq \int_0^\infty \kappa_P \rho_{\rm eq}(r)\, dr = \frac{\pi}{4} \rho_c \kappa_P H(\rho_c, T). \end{aligned} \tag{5.13}$$

As shown in Fig. 5.21, the approximation of Eq. (5.13) has a good agreement with the real optical depth.

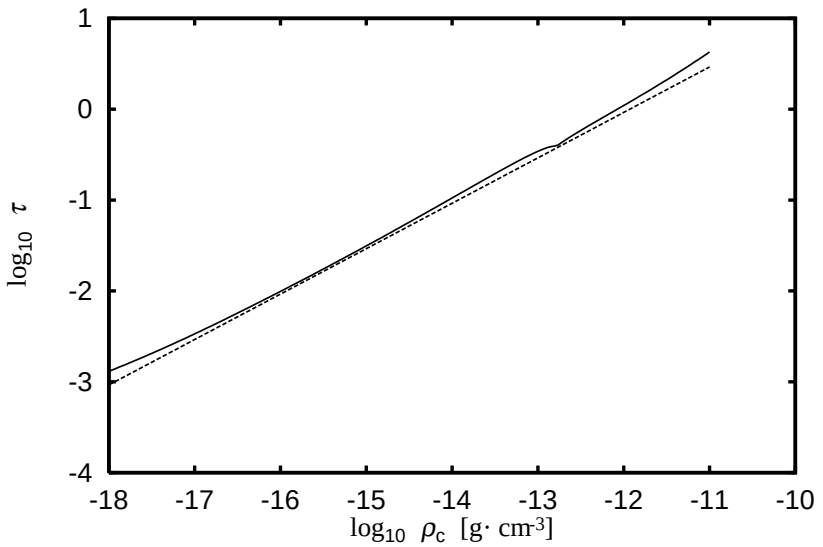

Figure 5.21: The comparison between the real optical depth τ of the filaments (solid curve) and the approximated τ given by the Eq. (5.13) (dotted line) for $T_{\rm init} = 10$ K and $\kappa_{10} = 0.02\,{\rm g}^{-1}\,{\rm cm}^2$ model.

5.1.6 Radiative flux

At the initial time, the radiative flux is nearly equal to zero at all positions since the optically thin filaments are embedded in the isotropic radiation field. The radiative flux distribution, however, forms a peak at the radius of the scale height and a slope as $F_r \propto r^{-1}$ in the outer envelope, as seen in Fig. 5.22.

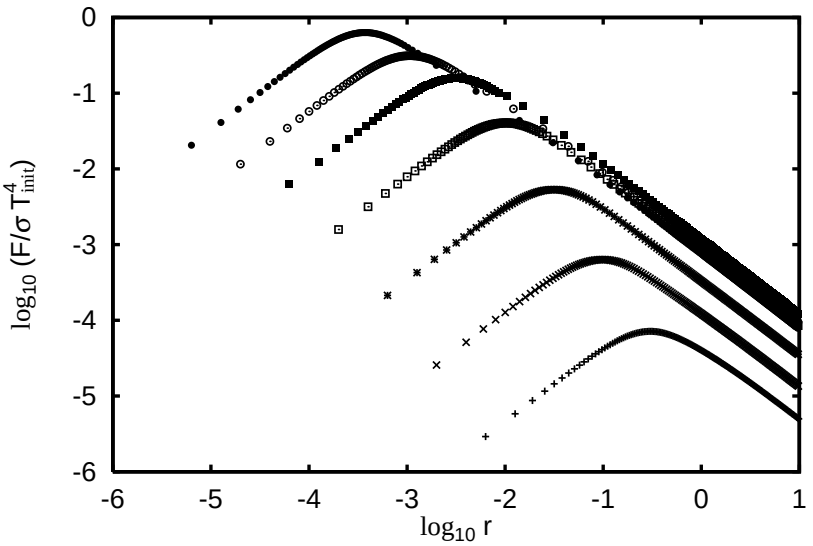

Figure 5.22: The evolution of the radiative flux in the case of $T_{\rm init} = 10$ K and $h^2 = 2$ model. A peak of the radiative flux in each phase is at near the scale height in that time.

5.2 Flat density model

This section gives results of the calculations for the flat density model. Also, some related results are presented in Appendix C.

Though the initial density distribution is different from the standard model, it approaches to the equilibrium distribution like the cases of the standard model (Fig. 5.23). The time-scale of the collapse, however, is shorter than that of the standard model as shown in Fig. 5.24. The T–ρ plane diagram, Fig. 5.25, is similar to the case of the standard model.

Calculations with other h values are also performed, and their time evolution of the central density is shown in Fig. 5.28.

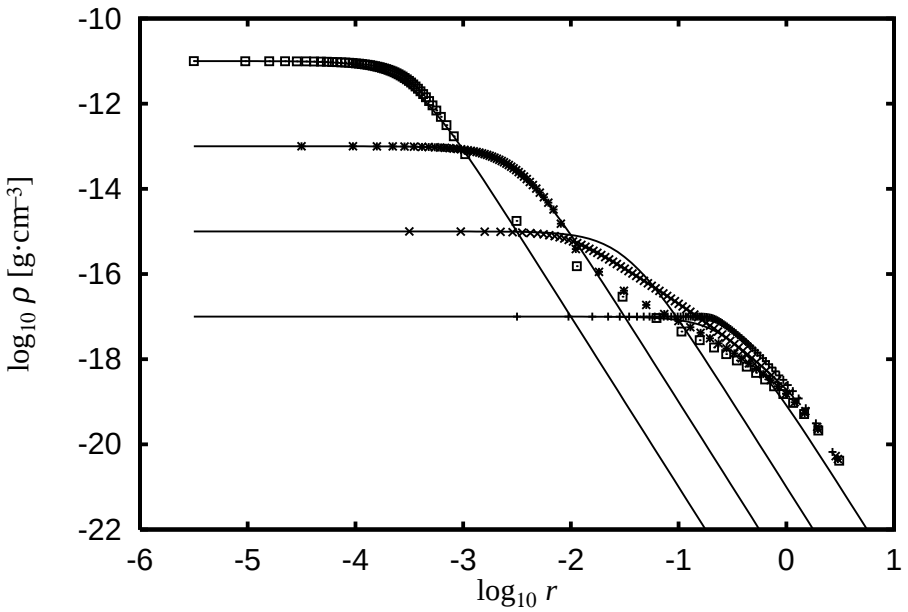

Figure 5.23: The development of the density distributions on the flat model. Each set of points denotes the density at the time of $t = 0.546$, 0.626, 0.685, 0.722. See also Fig. 5.24.

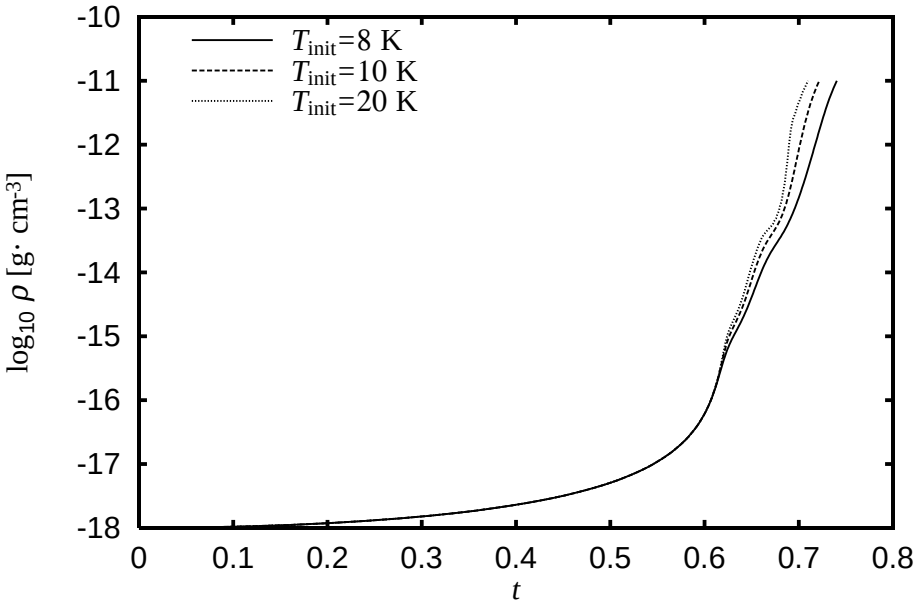

Figure 5.24: The central densities for $T_{\rm init}$ = 8 K, 10 K, and 20 K models.

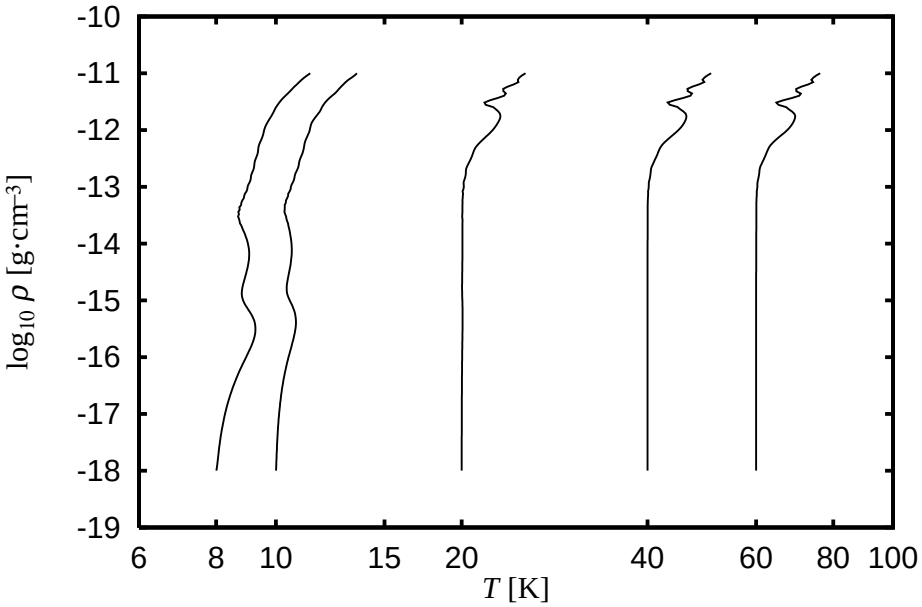

Figure 5.25: The T–ρ plane diagram for the flat density model.

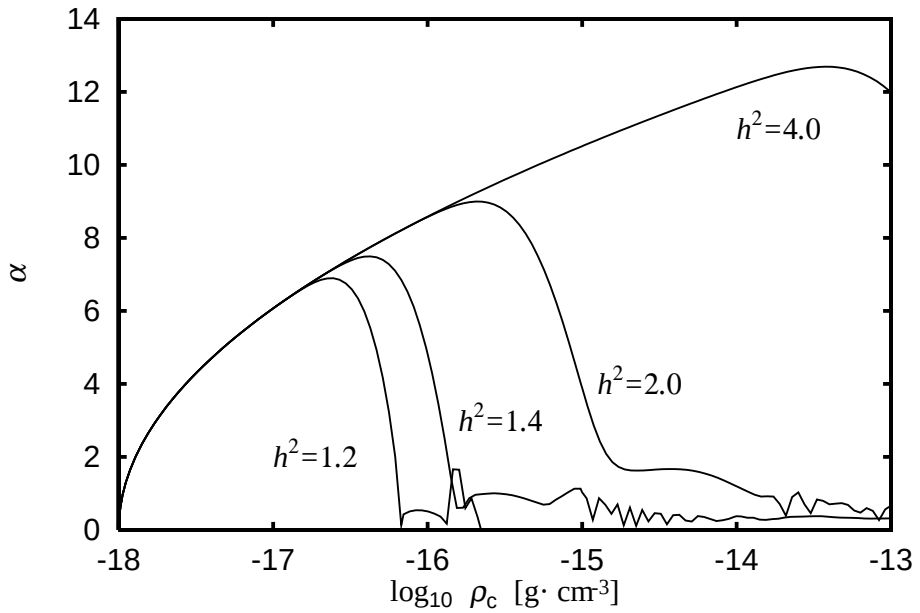

Figure 5.26: The α for the flat density model.

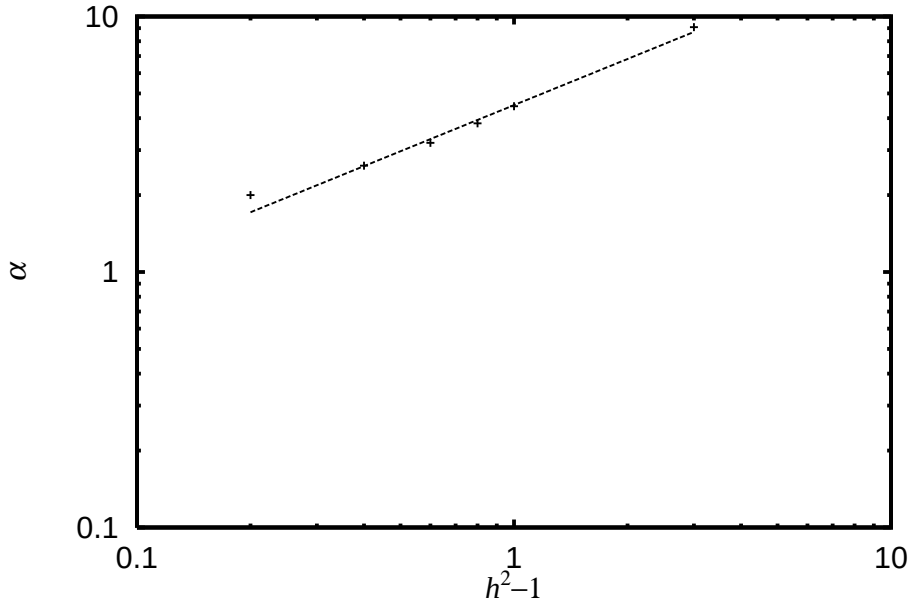

Figure 5.27: The averaged α as a function of the h parameter.

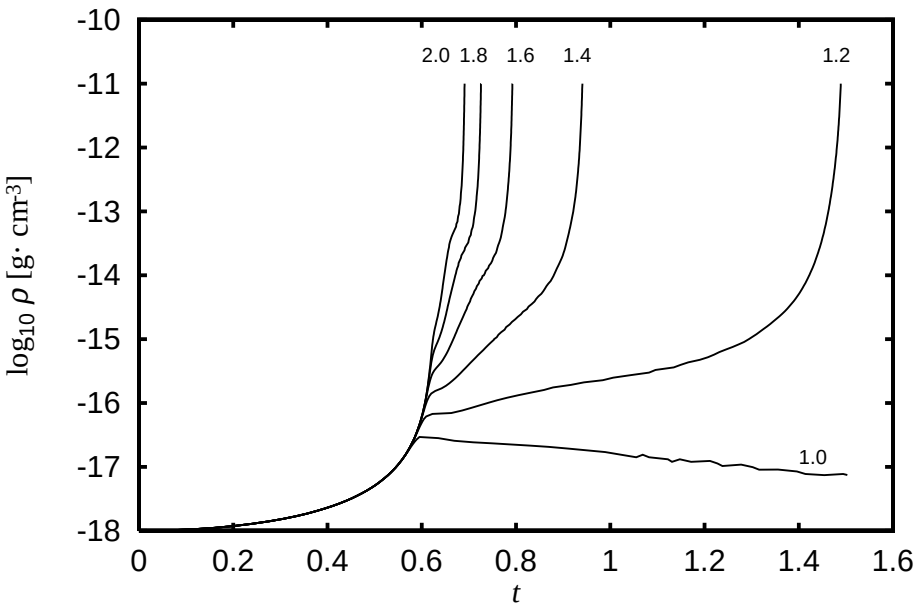

Figure 5.28: The time evolution of the central density with several h parameters.

5.3 Cosmic ray heating model

This section gives results of calculations for the cosmic rays model. Also, some related figures are presented in Appendix D.

In this model, it is assumed that in the initial stage the energy balance is established between the dust cooling and the cosmic rays heating, and that there is no incident radiation. The main heating source in the early phase is the cosmic rays heating. The last term of the RHS of energy equations ($\Gamma_{\rm ext}$), which is zero in the standard model, is not zero, while $\Gamma_{\rm abs}$ is negligible in the early phase. Results of this model, which are shown in Fig. 5.29 and Fig. 5.30, have great differences from those of the standard model. The reason of these differences will be discussed in Chapter 6.

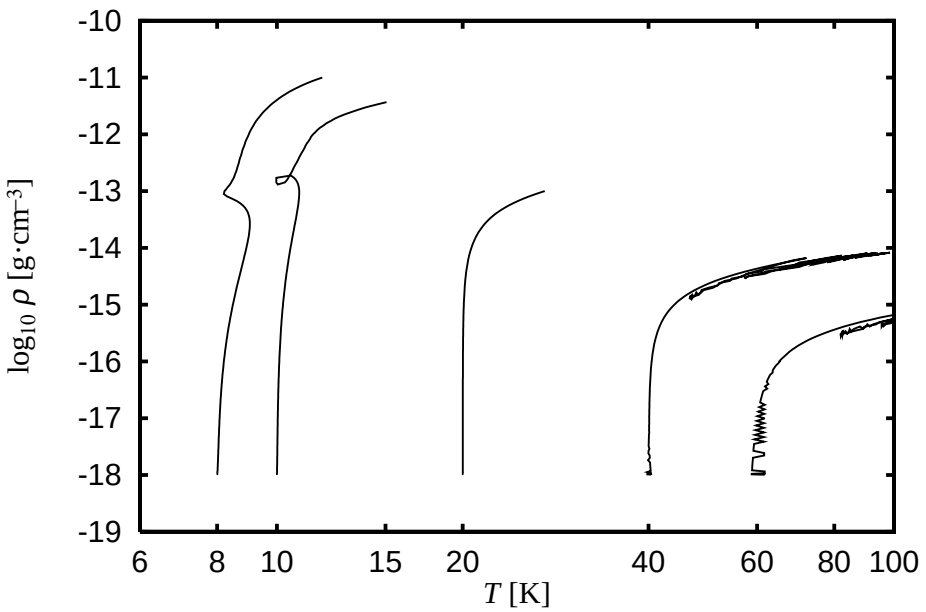

Figure 5.29: The T–ρ plane diagram of the cosmic rays model.

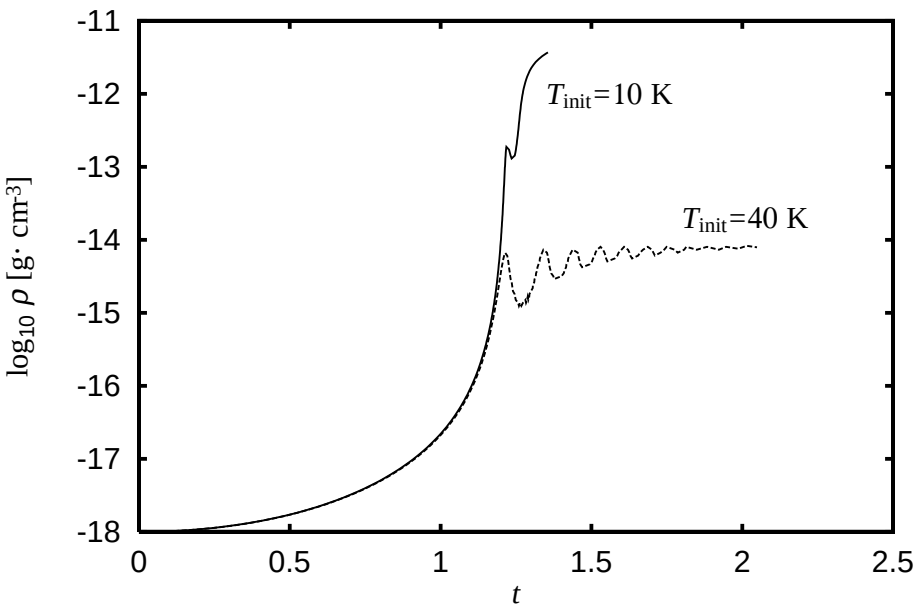

Figure 5.30: The central densities of the cosmic ray heating model for the cases of $T_{\rm init} = 10$ K and $T_{\rm init} = 40$ K.

Chapter 6

Discussion

As seen in the T–ρ plane diagram in the previous chapter (see Fig. 5.9), the gravitationally collapsing filaments are isothermal in the early phase, but a breakdown of the isothermality takes place at a certain time. Then the filaments enter the non-isothermal phase. In other words, the thermodynamical transition occurs at some time during the gravitational collapse.

The transition have a great influence on the dynamics of the collapsing filaments, e.g., bounces and fragmentation are caused. Moreover, the thermodynamical properties strongly depend on the radiative transfer since it is a main process which transports energies in the clouds. Therefore, we focus our attention on the radiative transfer effects.

Masunaga, Miyama, & Inutsuka (1998 [17]) also studied collapsing spherical clouds with the RHD code using the VEF algorithm. The main difference from our calculation is in its geometry. The dynamics of self-gravitational collapse in the cylindrical geometry is more sensitive to the thermodynamical properties than that in the spherical geometry.

Nakamura (1998 [26]) also studied the self-gravitational collapse of the filaments as well as our calculation. However, the simulated stage of collapsing

filaments is earlier than ours. His calculation starts at $n_c = 10^3\,\mathrm{cm}^{-3}$ ($\rho_c \approx 3.8 \times 10^{-21}\,\mathrm{g\,cm}^{-3}$) and ends at $n_c = 10^{10}\,\mathrm{cm}^{-3}$ ($\rho_c \approx 3.8 \times 10^{-14}\,\mathrm{g\,cm}^{-3}$), where n_c is the central number density. The established energy balance in the isothermal phase is also different. The main heating source which is balanced with the cooling is not the external heating due to the cosmic ray or the incident radiation but the gas compressional heating. Namely, the environment that the external heating is not very high is considered in Nakamura's work.

We carried out calculations under widely various conditions, and analyzed these results.

6.1 Criterion of the isothermality

It is a meaningful problem when the transition occurs during the gravitational collapse. The timing can be specified by a central density at that time since the density distributions of collapsing filaments are close to the equilibrium distribution given in Eq. (5.6).

The first point that requires clarification is why the filaments are isothermal in the early phase. Before the gravitational collapse starts, the balance between the heating and cooling processes is assumed, i.e., the RHS of the gas energy equation (3.18) is zero under the condition of $\Gamma_{\mathrm{dyn}} = 0$. Moreover, the filaments can also keep their isothermality during gravitational collapse if the cooling processes can efficiently convey the newly released gravitational energy far away. However, the released energy increases and the time-scale of collapse decreases as the collapse proceeds. Then, the cooling process is overloaded and the filaments can keep their isothermality no longer. In other words, the collapsing filament remains isothermal as long as the cooling time-scale is shorter than the dynamical time-scale; this is the condition for

the isothermality. In the following sub-sections, some necessary equations such as a cooling rate and time-scales are derived and finally an analytic expression of the criterion is derived.

6.1.1 Effective cooling rate

In order to cool the filaments by the dust-cooling, the radiative energy emitted by the dust grains should be transported to the outside of the filament. It is expected that an effective cooling rate in optically thick media is reduced since the emitted photons are trapped again in the filaments. The effective cooling rate $\Lambda_{\rm eff}$, which depends on the optical depth, is derived below.

Optically thin cases The emitted radiation at any position in a volume element can escape freely. Then the effective cooling rate can be written as

$$\Lambda_{\rm eff} = \frac{1}{\rho \Delta V} \int_{\Delta V} dV \oint \eta \, d\Omega = \frac{1}{\rho} \oint \rho \kappa_P B \, d\Omega, \tag{6.1}$$

therefore,

$$\Lambda_{\rm eff} = 4\pi \kappa_P B = 4\sigma \kappa_P T^4 = \Lambda_{\rm dust}. \tag{6.2}$$

Optically thick cases The optically thick media can radiate away only from near the surface. Thus, the effective cooling rate is reduced.

The diffusion approximation is valid in thick media;

$$\Lambda_{\rm eff} = \frac{1}{\rho} \nabla \cdot \boldsymbol{F}, \quad \boldsymbol{F} = -\frac{c}{3\rho\kappa_P} \nabla E, \quad E = aT^4. \tag{6.3}$$

Therefore,

$$\Lambda_{\rm eff} = \frac{1}{\rho} \nabla \cdot \left(-\frac{c}{3\rho\kappa_P} \nabla E \right). \tag{6.4}$$

Assuming a convex energy distribution ($\nabla^2 E < 0$), the equation above can be roughly estimated as

$$\Lambda_{\rm eff} \sim \frac{c\kappa_P a T^4}{3(\rho\kappa_P)^2 H^2}, \tag{6.5}$$

where H is a characteristics scale. Substituting τ^2 for $3(\rho\kappa_P H)^2$, the following equation is obtained,

$$\Lambda_{\rm eff} \sim \frac{\Lambda_{\rm dust}}{\tau^2}, \tag{6.6}$$

where τ is the optical depth.

Finally, the effective cooling rate for any optical depth case is given by

$$\Lambda_{\rm eff} = \frac{\Lambda_{\rm dust}}{\max(1, \tau^2)}. \tag{6.7}$$

6.1.2 Cooling time-scale and dynamical time-scale

A cooling time-scale is defined by

$$t_{\rm cool} \equiv \frac{e_{\rm gas}}{\Lambda_{\rm eff}}. \tag{6.8}$$

The $t_{\rm cool}$ can be expressed as a function of the central density and the temperature of filaments, since the analytic expression of the optical depth τ, which appears in Eq. (6.7), has been obtained as Eq. (5.13) and $\Lambda_{\rm dust}$ is simply equal to $4\kappa_P \sigma T^4$.

On the other hand, a dynamical time-scale $t_{\rm dyn}$ is defined by

$$t_{\rm dyn} \equiv \left. \frac{\rho}{\dot{\rho}} \right|_{r=0}. \tag{6.9}$$

From Eq. (3.14), the equation above can be rewritten as

$$t_{\rm dyn} = \frac{1}{-\nabla\cdot\boldsymbol{v}} = \frac{\frac{p}{\rho}}{-\frac{p}{\rho}\nabla\cdot\boldsymbol{v}} = \frac{(\gamma-1)e_{\rm gas}}{\Gamma_{\rm dyn}}, \tag{6.10}$$

all variables should be evaluated at $r = 0$. An analytic form of the $\Gamma_{\rm dyn}$ at the center has been obtained approximately as Eq. (5.12). Using the approximation form, the $t_{\rm dyn}$ can be expressed as a function of the central density and the temperature. However, the approximation form of $\Gamma_{\rm dyn}$ is only valid for the isothermal phase. Furthermore, we have to remember that even in the isothermal phase it is not as accurate as the approximation form of the optical depth τ.

Both the cooling time-scale and the dynamical time-scale have been obtained. The variations of these time-scales during the gravitational collapse are shown in Fig. 6.1 for $T_{\rm init} = 10$ K and in Fig. 6.2 for $T_{\rm init} = 20$ K.

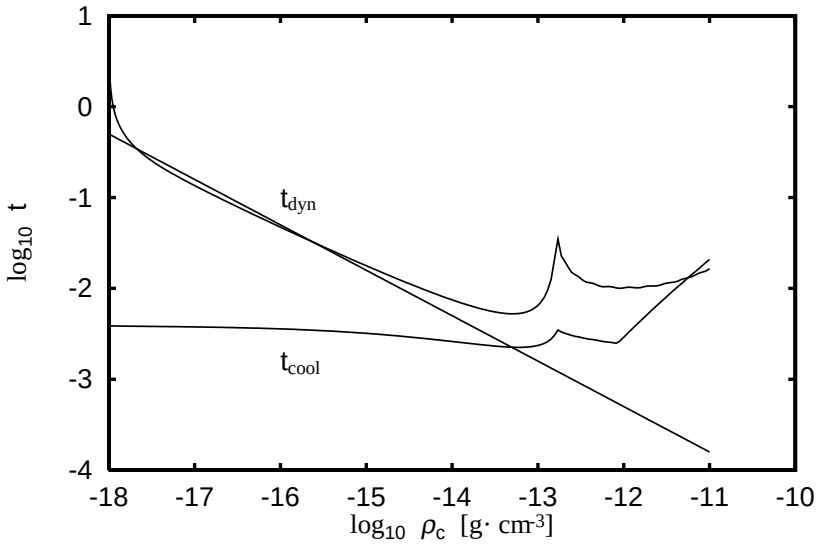

Figure 6.1: Time-scales in the case of $T_{\rm init} = 10$ K. Two curves correspond the dynamical time-scale $t_{\rm dyn}$ and the cooling time-scale $t_{\rm cool}$, respectively. A line represents an analytically estimated dynamical time-scale. A peak of $t_{\rm dyn}$ near $\rho_c \approx 10^{-13}\,{\rm g\,cm^{-3}}$ expresses that the collapse is slowed down due to the phase transition from the isothermal to the non-isothermal phase.

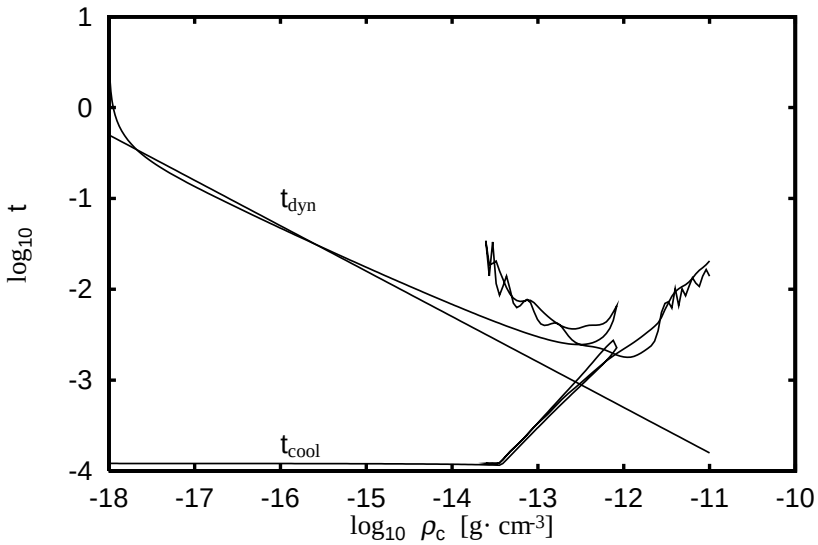

Figure 6.2: The time-scales in the case of $T_{\rm init} = 20$ K.

6.1.3 Characteristic densities

The ρ_τ is defined as a value of the central density when the filaments turn to be opaque. Then, ρ_τ just means a boundary between optically thin regime and thick regime. By using the Eq. (5.13),

$$\frac{\pi}{4}\rho_\tau \kappa_P H(\rho_\tau, T) = 1, \tag{6.11}$$

ρ_τ is derived by solving the equation above as

$$\rho_\tau = 1.18 \times 10^{-12} \left(\frac{\kappa_{10}}{0.02\,{\rm g}^{-1}\,{\rm cm}^2}\right)^{-2} \left(\frac{T}{10\,{\rm K}}\right)^{-(1+2\beta)} {\rm g\,cm}^{-3}. \tag{6.12}$$

The filaments whose central densities are higher than ρ_τ are opaque.

As discussed in the the beginning of this section, the condition for the isothermality is

$$t_{\rm cool} \lesssim t_{\rm dyn}. \tag{6.13}$$

In our problems, the dynamical time-scale is much longer than the cooling time-scale in the early phase. However, the dynamical time-scale $t_{\rm dyn}$ gets

short as the contraction proceeds and it approaches to the cooling time-scale $t_{\rm cool}$ (see Fig. 6.1 and Fig. 6.2). The critical density $\rho_{\rm crit}$ is defined as the central density when the dynamical time-scale $t_{\rm dyn}$ becomes equal to the cooling time-scale $t_{\rm cool}$. It is expected that the breakdown of the isothermality occurs when the central density exceeds the $\rho_{\rm crit}$.

The critical density $\rho_{\rm crit}$ can be derived analytically from $t_{\rm dyn} = t_{\rm cool}$. Since the effective cooling rate $\Lambda_{\rm eff}$ is switched at $\tau = 1$, the critical density is expressed as Eq. (6.14). The function of the critical density $\rho_{\rm crit}$, which depends on the gas temperature, is switched at the temperature $T = T_s$.

$$\rho_{\rm crit} = \begin{cases} \rho_s \left(\frac{T}{T_s}\right)^{6+2\beta} & \text{for } T \le T_s \\ \rho_s \left(\frac{T}{T_s}\right)^{(4-2\beta)/3} & \text{for } T \ge T_s \end{cases}, \tag{6.14}$$

where ρ_s and T_s are given as following,

$$\rho_s = 2.85 \times 10^{-13} \left(\frac{\alpha}{2}\right)^{-\frac{2(1+2\beta)}{7+4\beta}} \left(\frac{\kappa_{10}}{0.02\,{\rm g^{-1}\,cm^2}}\right)^{-\frac{10}{7+4\beta}} {\rm g\,cm^{-3}}, \tag{6.15}$$

$$T_s = 13.3 \times \left(\frac{\alpha}{2}\right)^{\frac{2}{7+4\beta}} \left(\frac{\kappa_{10}}{0.02\,{\rm g^{-1}\,cm^2}}\right)^{-\frac{4}{7+4\beta}} {\rm K}. \tag{6.16}$$

Figure 6.3 shows that the line of $\rho_{\rm crit}$ intersects the line of ρ_τ at $T = T_s$. Notice that filaments whose initial temperature is $T_{\rm init} > T_s$ become opaque before exceeding the critical density, and the filaments continue to be isothermal even if they are opaque. In the case of $\beta = 2$, the $\rho_{\rm crit}$ for $T > T_s$ has a remarkable property that the critical density is independent of the initial temperature of the filament.

An argument similar to this section is given by Masunaga, Miyama, & Inutsuka (1998 [17]). But they analyzed the case of spherically symmetric collapse. They did not take into account the effect of α, which represents the difference from the dynamical equilibrium state. Because the collapse of filaments is strongly affected by the thermodynamics, the conclusion for the

collapse of filaments has become slightly different from that of the spherically symmetric case, i.e., the critical density depends on the α.

6.1.4 Comparison with numerical results

Derived characteristic densities, ρ_τ and $\rho_{\rm crit}$, are compared with numerical results for various conditions. For example, in Fig. 6.3, ρ_τ and $\rho_{\rm crit}$ are plotted on the T–ρ plane with evolutional tracks of filaments, which are identical with those of Fig. 5.9. This figure shows that our analytic estimates have a good agreement with numerical results..

Other calculations with extreme values of κ_{10} are also performed to verify our estimates of the critical density (Fig. 6.4 and 6.5). As shown in these figures, evolutional tracks in these cases show expected behaviors though both ρ_τ and $\rho_{\rm crit}$ are different from previous cases.

In order to investigate the dependence of the critical density on the h-parameter, calculations with different values of h are carried out. Figure 6.6 and 6.7 show the results in the case of $h^2 = 1.2$ and $h^2 = 4.0$, respectively. The numerical coefficient α which appears in Eq. (5.12) weakly depends on the h-parameter, e.g., $\alpha = 0.8$ for $h^2 = 1.2$ and $\alpha = 3.0$ for $h^2 = 4.0$ for the standard model. The filaments of the flat density model is more gravitationally unstable than those of the standard model. So the parameter α becomes larger than those of the standard model, e.g., $\alpha = 9.1$ for $h^2 = 4.0$ (Fig. 6.8).

The results of the cosmic ray heating model show the different behavior from those of the standard model (see Fig. 6.9). The obvious differences appear in the cases of $T_{\rm init} = 20, 40, 60$ K. The non-isothermal transitions occur when the filaments become opaque, $\rho_c \simeq \rho_\tau$. Inutsuka & Miyama (1997 [9]) also considered that the critical density for $T > T_s$ is determined

by $\tau = 1$, that is ρ_τ. The consideration agrees with our cosmic ray heating model. However, in a real situation of star forming regions, the cosmic ray heating rate is too small to maintain the clouds to the high temperature as about 60 K. Thus, we consider that this model is unreal.

Why is the critical density of the cosmic ray heating model determined by the optical depth? In the early phase, the energy balance is established between the dust cooling and the cosmic ray heating, i.e., $\Lambda_{\rm dust} = \Gamma_{\rm ext}$. On the other hand, the heating due to the radiative absorption $\Gamma_{\rm abs}$ ($= c\kappa_E E$) is negligible since there is no incident radiation and the filaments are transparent. However, when the filaments become opaque, $\Gamma_{\rm abs}$ becomes comparable to $\Lambda_{\rm dust}$ (see Fig. D.3 and Fig. D.4), and the heating rate becomes greater than the cooling rate.

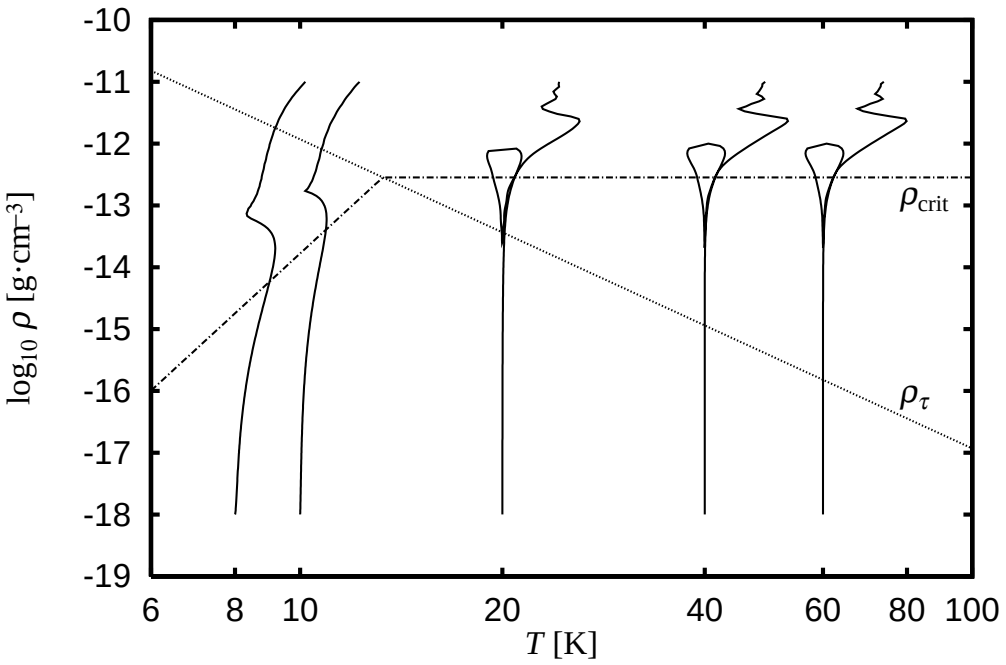

Figure 6.3: Lines of both ρ_τ and $\rho_{\rm crit}$ are overplotted on Fig. 5.9 in order to be compared with our numerical results for several initial conditions. Curves are identical with those in Fig. 5.9. The filaments are transparent when the central densities are lower than ρ_τ, and they become opaque when the densities exceed ρ_τ. The critical density $\rho_{\rm crit}$ is in good agreement with the breakpoints of isothermality. Notice that the filaments are isothermal even in optically thick regime, until exceeding $\rho_{\rm crit}$.

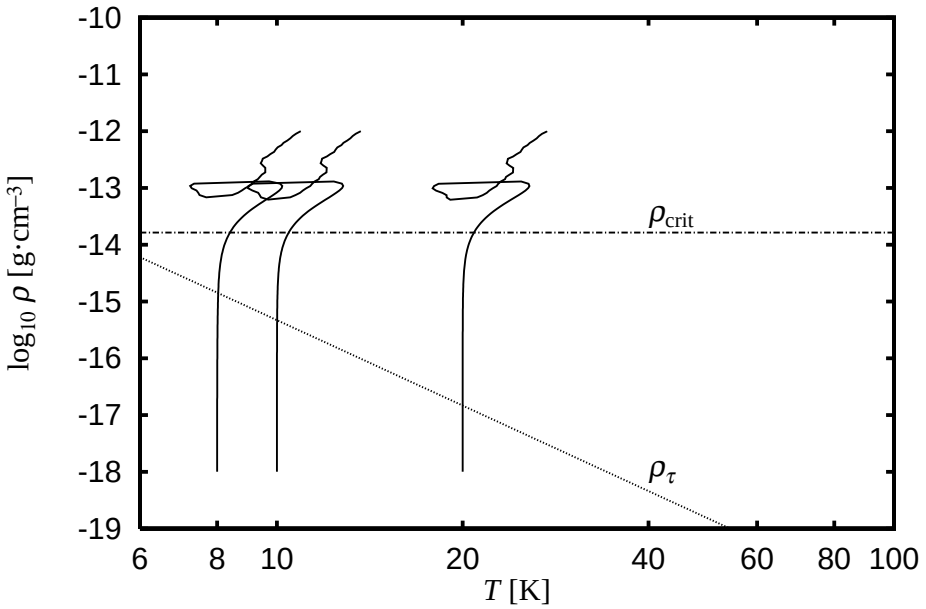

Figure 6.4: Evolutional tracks in the case of $\kappa_{10} = 1.0\,\mathrm{g}^{-1}\,\mathrm{cm}^2$ and $h^2 = 2$.

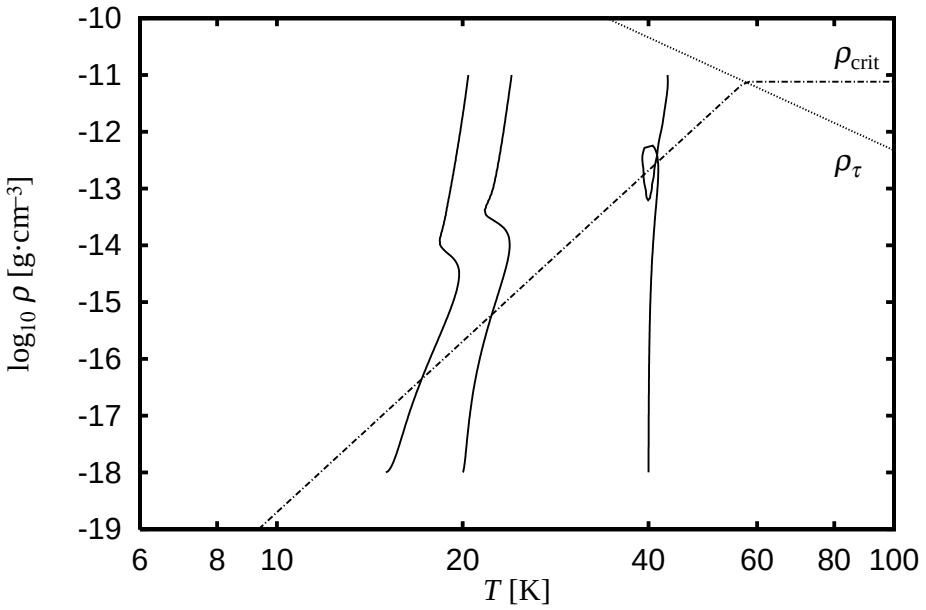

Figure 6.5: Evolutional tracks in the case of $\kappa_{10} = 10^{-4}\,\mathrm{g}^{-1}\,\mathrm{cm}^2$ and $h^2 = 2$.

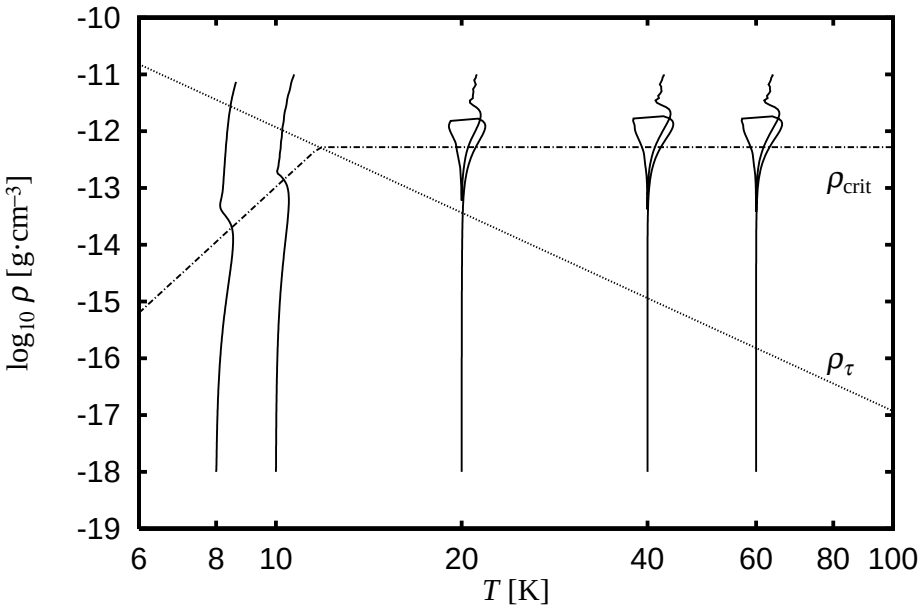

Figure 6.6: In the case of $h^2 = 1.2$. $\rho_{\rm crit}$ and ρ_τ are plotted by using $\alpha = 0.8$.

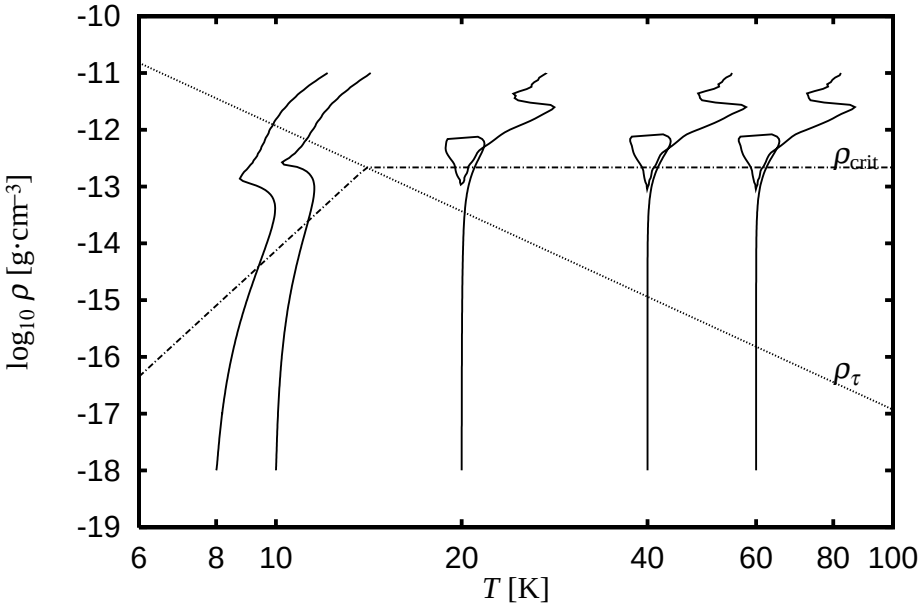

Figure 6.7: In the case of $h^2 = 4.0$. The α is taken to be $\alpha = 3.0$.

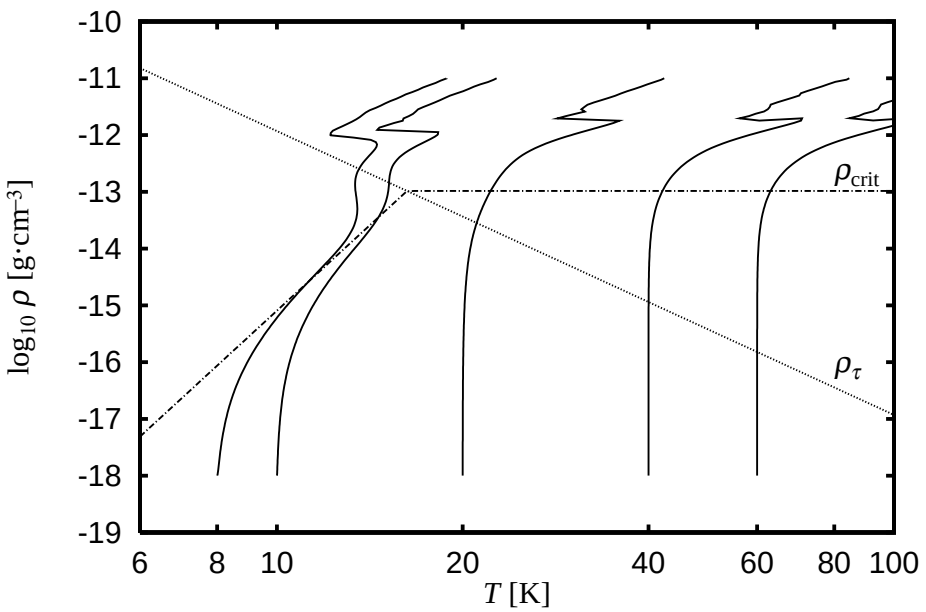

Figure 6.8: In the case of $h^2 = 4.0$ on flat density model. The α is taken to be $\alpha = 9.1$.

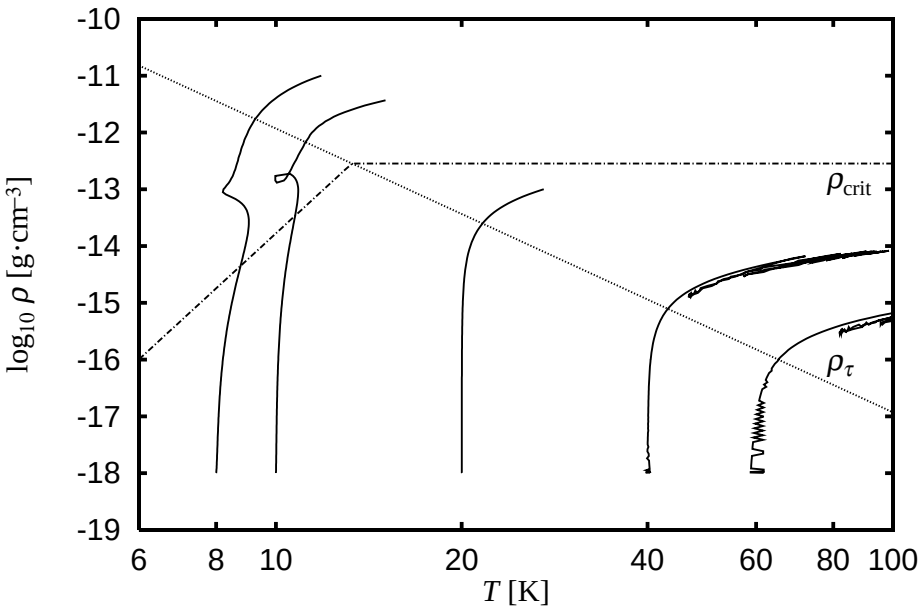

Figure 6.9: Evolutional tracks of cosmic ray heating models. Other condition are same with those of Fig. 6.3 models ($\kappa_{10} = 0.02\,\mathrm{g}^{-1}\,\mathrm{cm}^2$, $h^2 = 2$).

6.2 Fragmentation of filaments

Fragmentation of the filaments can occur due to the gravitational instability during the gravitational collapse. The mass of a fragmented core is meaningful to study the characteristic mass formed by the gravitational collapse and studied previously (e.g., Rees 1976 [34]; Silk 1977 [37]). Recently, Inutsuka & Miyama (1997 [9]) investigated the fragmentation processes of filaments by the smoothed particle hydrodynamics (SPH) simulations and showed the most unstable mode has a wavelength of 8 times as long as the scale height. Thus, if the fragmentation occurs, the mass of the core is expected as

$$\begin{aligned} M_{\rm frag} &\sim 8 m_{\rm eq}(T) H(\rho_{\rm frag}, T) \\ &\approx 0.008 M_\odot \left(\frac{\rho_{\rm frag}}{10^{-13}\,{\rm g\,cm^{-3}}} \right)^{-1/2} \left(\frac{T}{10\,{\rm K}} \right)^{3/2}, \end{aligned} \tag{6.17}$$

where $\rho_{\rm frag}$ is a value of the central density at which the fragmentation of filaments takes place.

When does the fragmentation occur? The thermodynamical transition can trigger the fragmentation, since the radial collapse is suddenly slowed down at that time, as previously shown in Fig. 6.1 and Fig. 6.2. The $t_{\rm dyn}$ gets larger than a time-scale to develop the perturbation. Then the filaments prefer to fragment into small cores. Though the discussion above is rather rough, we assume that the fragmentation of the filaments occurs at $\rho \sim \rho_{\rm crit}$. The $\rho_{\rm crit}$ is substituted for $\rho_{\rm frag}$ in Eq. (6.17), and the mass of a core is estimated as a function of the initial gas temperature,

$$M_{\rm frag} \approx 0.007 M_\odot \left(\frac{\alpha}{2} \right)^{\frac{2(2+\beta)}{7+4\beta}} \left(\frac{\kappa_{10}}{0.02\,{\rm g^{-1}\,cm^2}} \right)^{-\frac{1}{7+4\beta}} \begin{cases} \left(\frac{T}{T_s} \right)^{-\frac{3+2\beta}{2}} & \text{for } T \le T_s \\ \left(\frac{T}{T_s} \right)^{\frac{5+2\beta}{6}} & \text{for } T \ge T_s \end{cases}, \tag{6.18}$$

The mass given by Eq. (6.18) is meaningful as a minimum mass which can be formed due to the gravitational collapse of clouds. Since the fragments formed through the gravitational collapse are bound by the self-gravity, it seems hard to dissipate. Rather, we could expect that they collide and accumulate each other, and grows in mass. Therefore, it would be possible to explain the mass spectrum of low-mass objects such as brown dwarfs (whose mass is less than $0.08\,\mathrm{M}_\odot$). At least, we could expect that the mass derived from the Eq. (6.18) gives the minimum mass of objects which are formed through the gravitational collapse of clouds. The estimated masses are displayed in Fig. 6.10 and Fig. 6.11. These figures show lower limits of the mass as a function of the parent cloud temperature and the opacity of dust grains. For example, the minimum mass of a fragment formed in a $T = 60$ K cloud should be larger than that is formed from a $T = 10$ K cloud when the opacity is $\kappa_{10} = 0.02\,\mathrm{g}^{-1}\,\mathrm{cm}^2$. The M_{frag} has a minimum value at $T = T_s$ as long as β is taken to be a normal value ($0 \lesssim \beta \lesssim 2$). This minimum value of M_{frag} (about $0.01\,\mathrm{M}_\odot$) has only weak dependence on the opacity κ_{10}. This fact means that it is difficult to form cores which have lower mass than $0.01\,\mathrm{M}_\odot$ in any environment by the fragmentation of filaments.

Recently fainter objects has become detectable thanks to the development of observational technology. According to some recent observations, the mass of detected low-mass objects is as low as about $0.01\,\mathrm{M}_\odot$ (Martín *et al.* 1998 [15], Zapatero Osorio *et al.* 1999 [51]). Although it is difficult to say something about the mass spectrum of the low-mass objects at the moment because of the lack of the number of observations, it seems possible to consider that the lowest mass is about $0.01\,\mathrm{M}_\odot$ at most. If the observed objects are real brown dwarfs, their masses seem to be consistent with our analysis.

The $M_{\rm frag}$ is the minimum mass of a fragment formed by the gravitational collapse of a filamentary cloud. Thus, an object which is formed by a different manner such as planets could have a mass lower than the minimum mass. If an object whose mass is lower than $M_{\rm frag}$ is observed, it may be possible to consider that the object is a planet or something else which is formed through a mechanism except the gravitational collapse of a cloud.

Furthermore, the equation (6.18) may apply to a low metallicity cloud collapse case. When the metallicity is lower, the opacity κ_{10} is expected to be lower corresponding to the degree of the metallicity. For example, if the metallicity is 50 times as low as that of the solar value, then we could expect the opacity is $\kappa_{10} = 10^{-4}\,{\rm g}^{-1}\,{\rm cm}^2$. In that case, the minimum mass of a fragment could be larger than that of the star forming regions in our galaxy if the cloud temperature is lower than about 40 K, while it could be smaller if the temperature is higher than about 40 K (Fig. 6.10). However, it is not clear if this argument is valid or not at the moment because in our analysis molecular and atomic coolings are ignored and they must dominate in the low metallicity case. Also, it is not known which is the boundary value of the metallicity at which the dominant cooling mechanism changes. It may be worth pointing out, in passing, that the collapse of primordial gas clouds has been investigate by Uehara *et al.* (1996 [47]) and Nakamura & Umemura (1999 [29]) and found that the minimum mass is generally larger than that of the solar metallicity gas clouds.

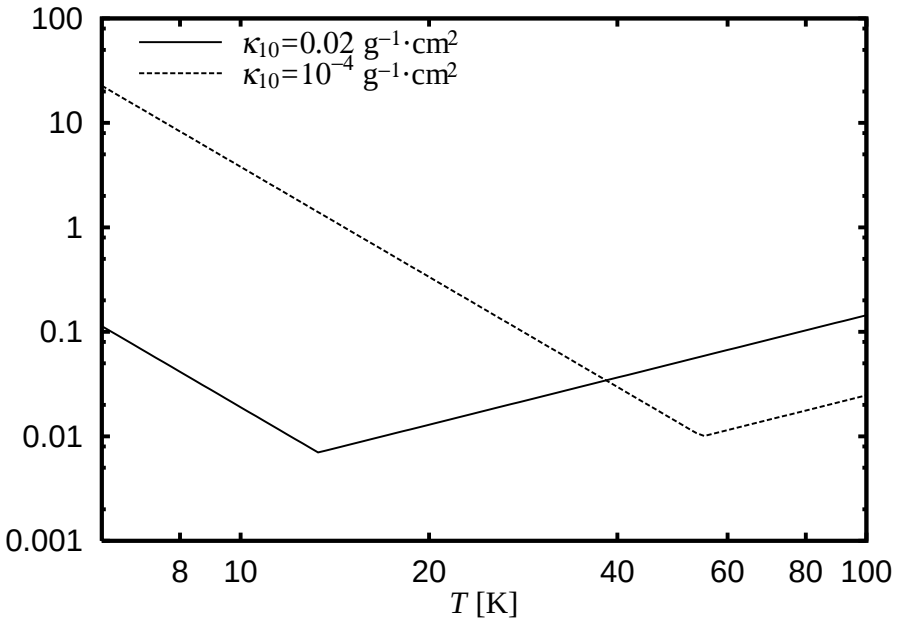

Figure 6.10: The estimated mass of a fragmented core is plotted as a function of the temperature of filaments in the case of $\beta = 2$. The unit of mass is the solar mass.

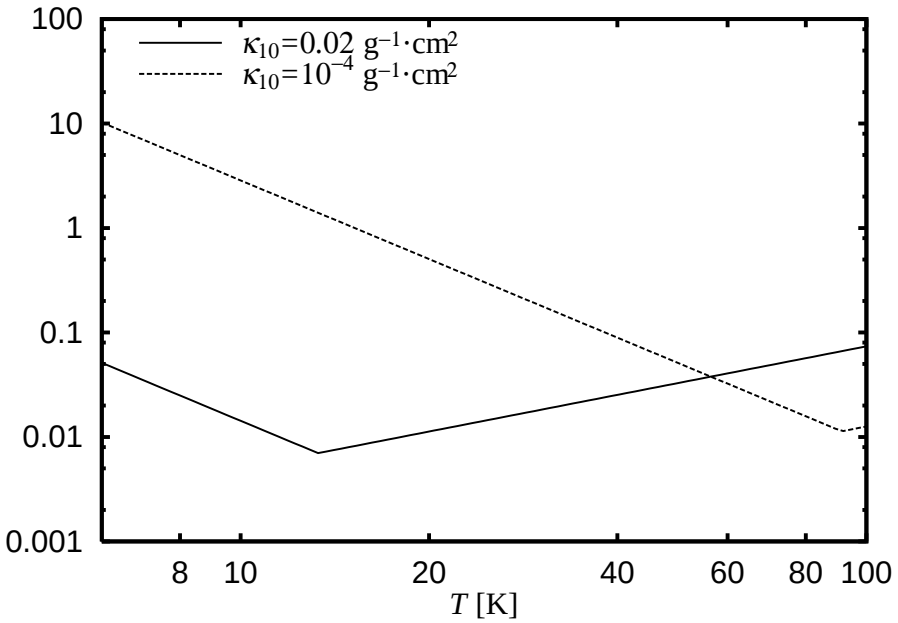

Figure 6.11: Identical with Fig. 6.10 except for $\beta = 1$.

Chapter 7

Conclusions

We performed radiation hydrodynamics (RHD) simulations to study the gravitational collapse of the filaments in molecular clouds. The followings are main conclusions of this study.

1. The filaments collapse isothermally in the early phase. The isothermality, however, breaks down when the dynamical time-scale becomes equal to the cooling time-scale.

2. Using semi-analytical considerations, the critical density $\rho_{\rm crit}$ for the thermodynamics transition is derived from $t_{\rm dyn} = t_{\rm cool}$. The transition takes place when the central density ρ_c exceeds $\rho_{\rm crit}$. The derived critical density is in a good agreement with numerical results.

3. Though it is widely considered that the filaments become adiabatic in the optically thick regime, we find that the filaments continue to collapse isothermally even if they are opaque, as long as $\rho_c < \rho_{\rm crit}$.

4. The dependence of the critical density is switched at T_s (about 13 K when $\kappa_{10} = 0.02\,{\rm g}^{-1}\,{\rm cm}^2$). The critical density for $T > T_s$ is independent of the gas temperature, when $\beta = 2$.

5. The radial contraction is slowed down at $\rho_c \sim \rho_{\rm crit}$. It is expected that the filaments will fragment into dense cores at that time. We estimated the mass of the fragments and found that the mass depends on the temperature of the parent cloud. When the opacity of dust grains is $0.02\,{\rm g}^{-1}\,{\rm cm}^2$, a cloud of the temperature $T = T_s$ ($\simeq$ 13 K) would have minimum mass fragments whose mass is about $0.01\,{\rm M}_\odot$.

Acknowledgments

We would like to thank M. Umemura and T. Nakamoto for careful reading our manuscripts and helpful discussion. We are grateful to the other members of astrophysics group in University of Tsukuba, especially to H. Susa and K. Ohsuga for many useful comments. The algorithm used in the RHD energy solver was in part given by N. Kikuchi.

Appendix A

Scalars, Vectors, and Tensors

Vectors, tensors, and contractions of them which appear in the basic equations for the 1-D axisymmetric cylindrical geometry are presented here.

$$\frac{1}{\rho}\nabla\cdot\boldsymbol{v} = \frac{\partial(2\pi r v)}{\partial m_r}, \quad \frac{1}{\rho}\nabla\cdot\boldsymbol{F} = \frac{\partial(2\pi r F)}{\partial m_r} \tag{A.1}$$

$$\nabla\boldsymbol{v} = \begin{pmatrix} \frac{\partial v}{\partial r} & 0 & 0 \\ 0 & \frac{v}{r} & 0 \\ 0 & 0 & 0 \end{pmatrix} \tag{A.2}$$

$$\mathsf{f} = \begin{pmatrix} f_{rr} & 0 & 0 \\ 0 & f_{\Phi\Phi} & 0 \\ 0 & 0 & f_{zz} \end{pmatrix} \tag{A.3}$$

$$\mathsf{f}:\nabla\boldsymbol{v} = f_{rr}\frac{\partial v}{\partial r} + f_{\Phi\Phi}\frac{v}{r} \tag{A.4}$$

$$\nabla\cdot(\mathsf{f}E) = \begin{pmatrix} \frac{\partial(f_{rr}E)}{\partial r} + \frac{f_{rr}-f_{\Phi\Phi}}{r}E \\ 0 \\ 0 \end{pmatrix} \tag{A.5}$$

Appendix B

Results of the standard model

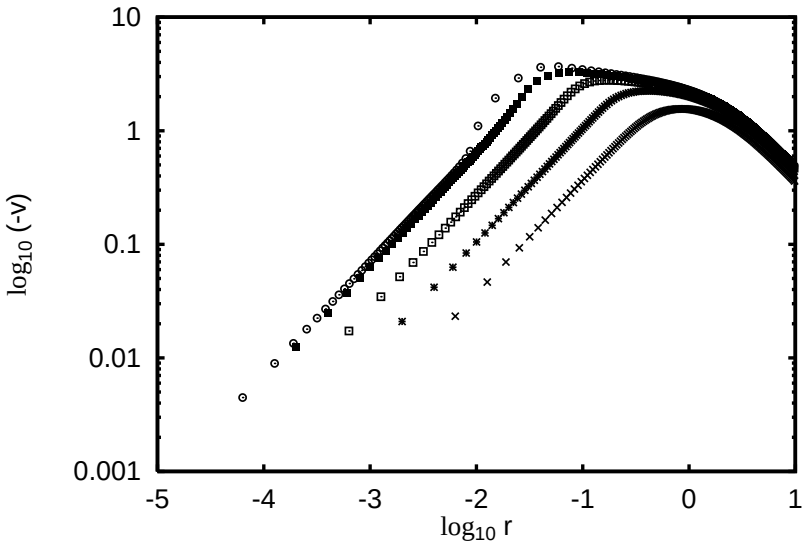

Figure B.1: The case of $T_{\rm init} = 10$ K. The velocity distributions are plotted when the central densities become to be $\log_{10}(\rho_c/\rho_{\rm init}) = 1, 2, 3, 4, 5$. See also Fig. B.2 and Fig. B.3

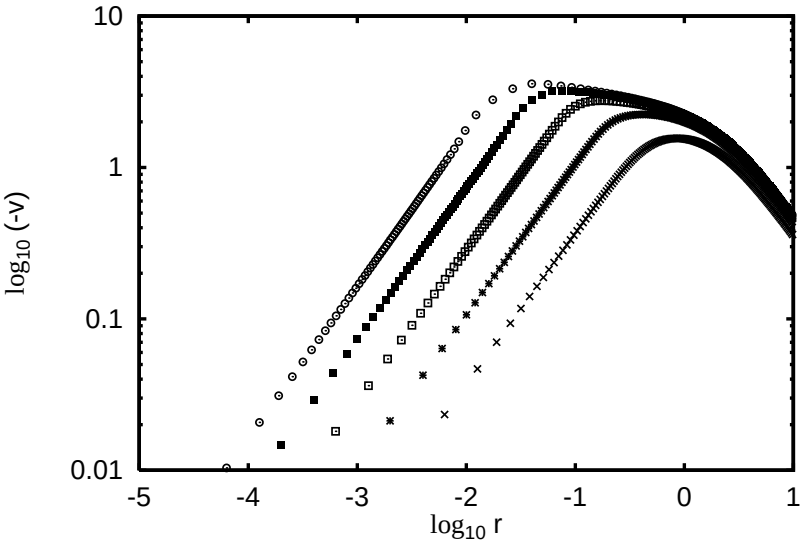

Figure B.2: The case of $T_{\rm init} = 20$ K.

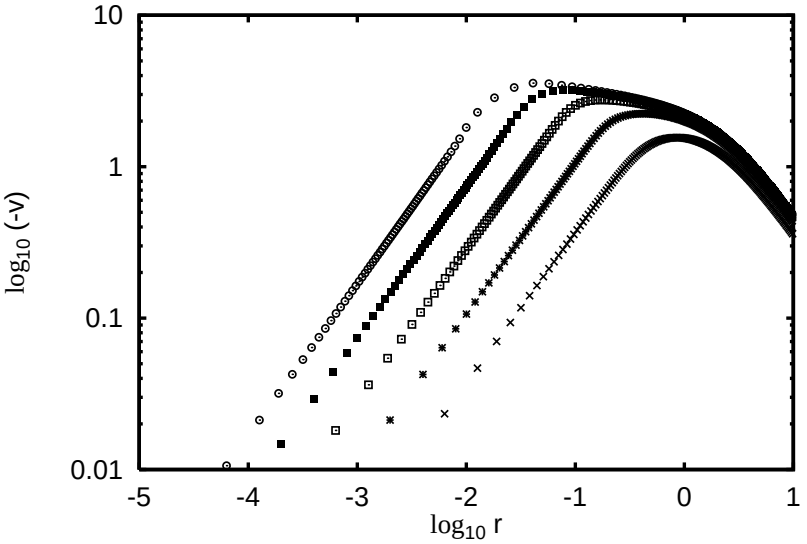

Figure B.3: The case of $T_{\rm init} = 40$ K.

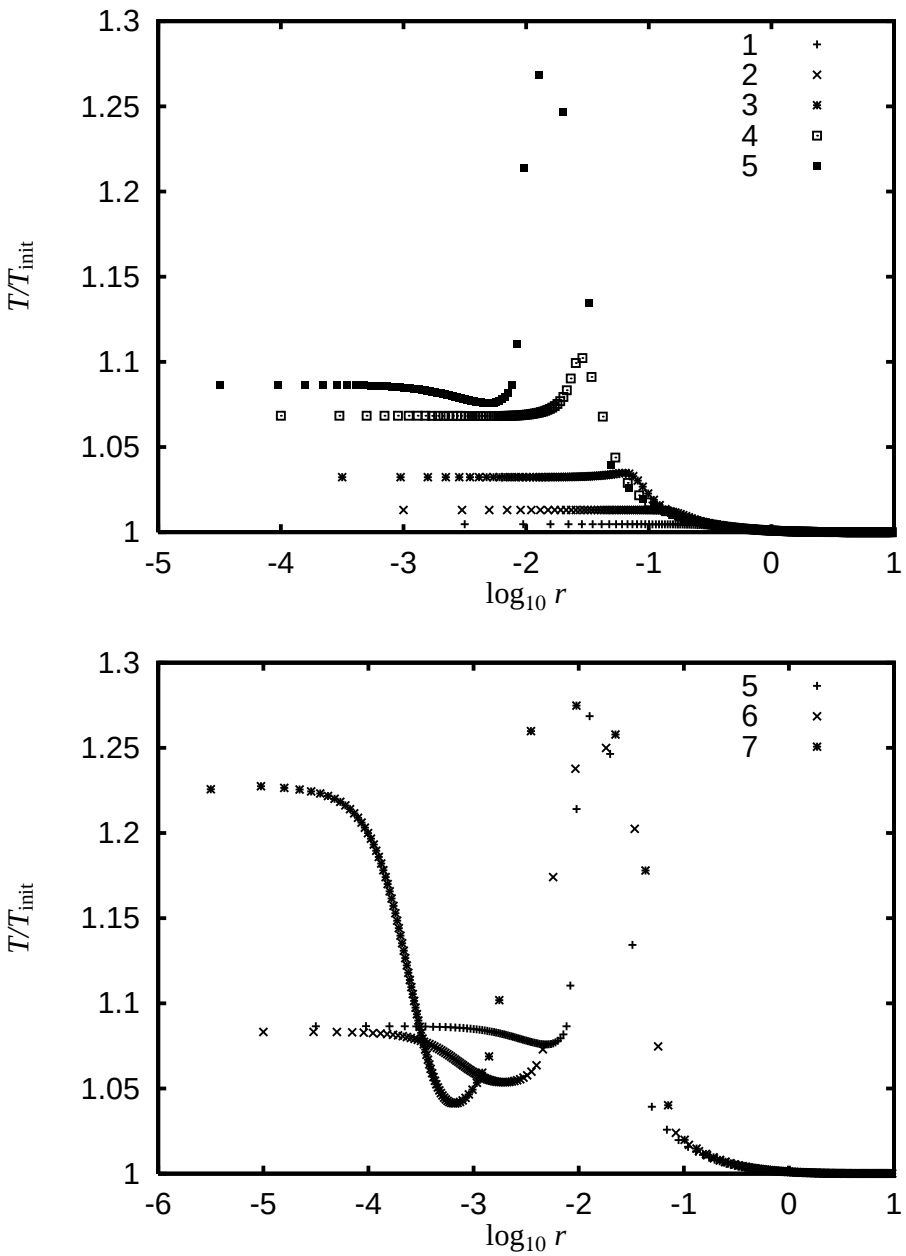

Figure B.4: The case of $T_{\rm init} = 10$ K. Numbers near symbols denote $\log_{10}(\rho_c/\rho_{\rm init})$. Peaks are derived from the shock heating.

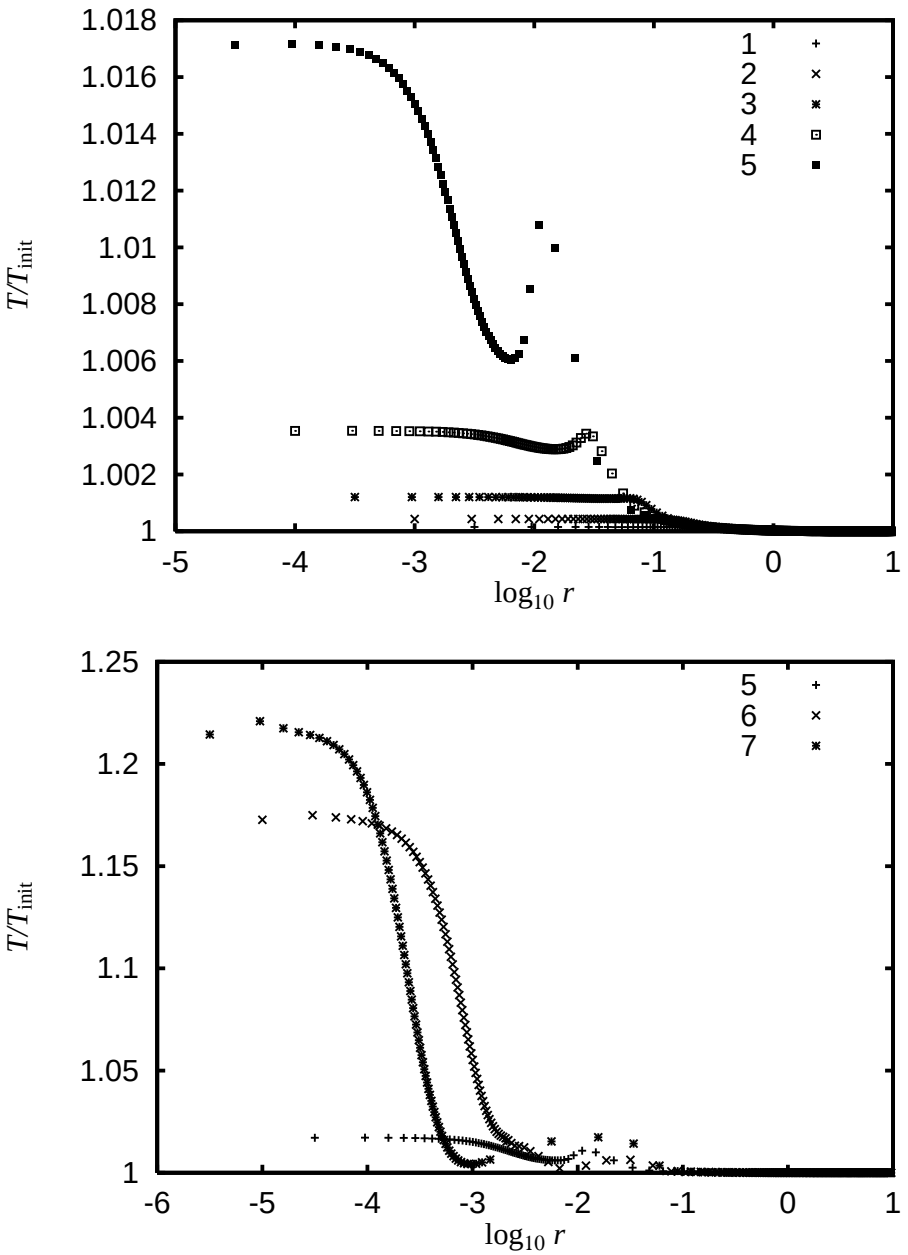

Figure B.5: The case of $T_{\rm init} = 20$ K.

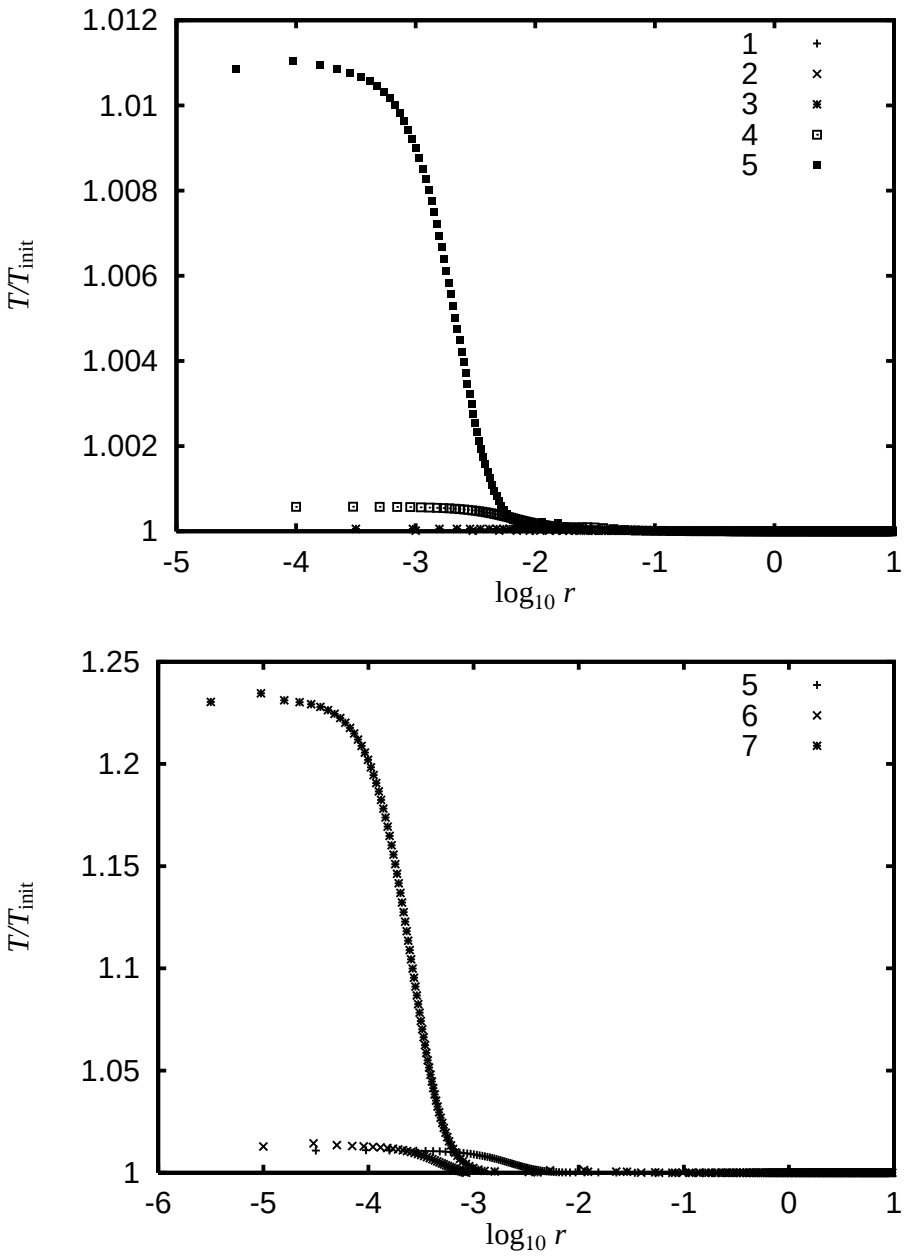

Figure B.6: The case of $T_{\rm init} = 40$ K.

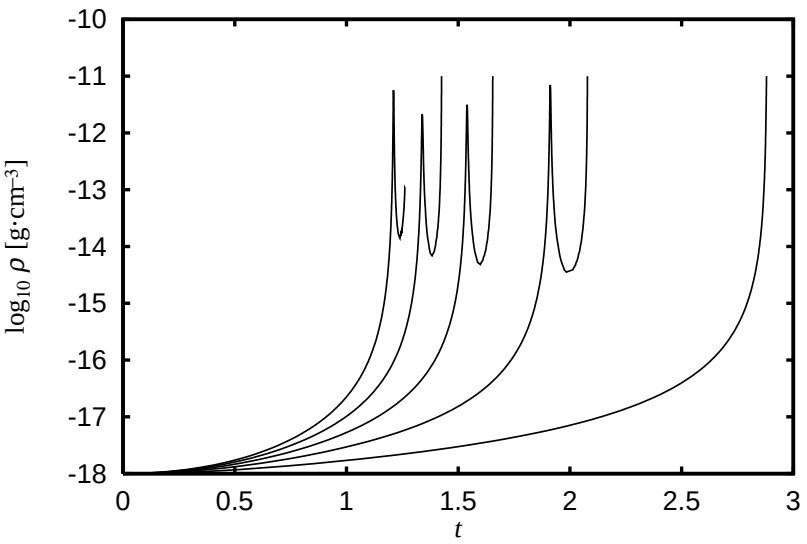

Figure B.7: The density evolution at the center with various h. Curves from left to right correspond to $h^2 = 1.2$, 1.4, 1.6, 1.8, 2.0.

Appendix C

Results of the flat density model

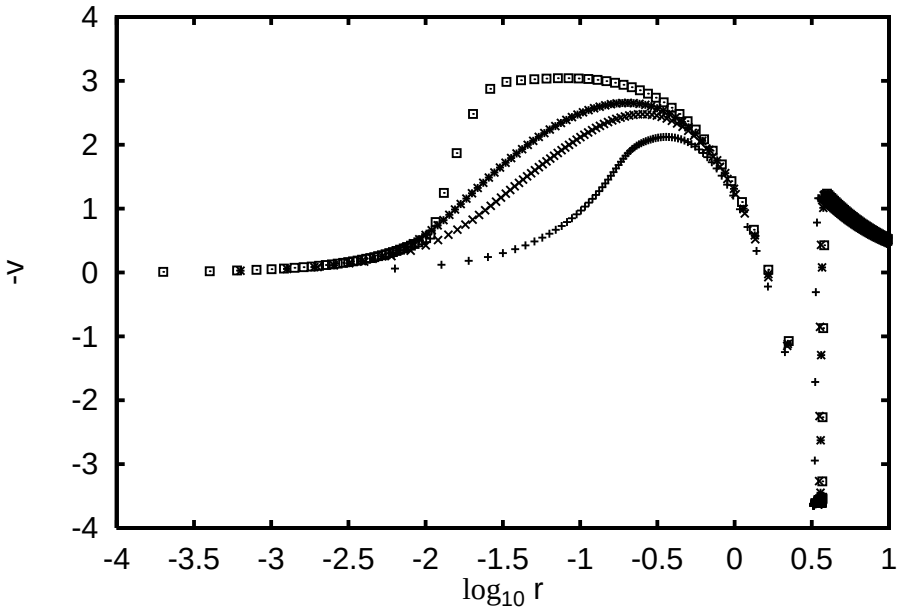

Figure C.1: The velocity field for 10 K.

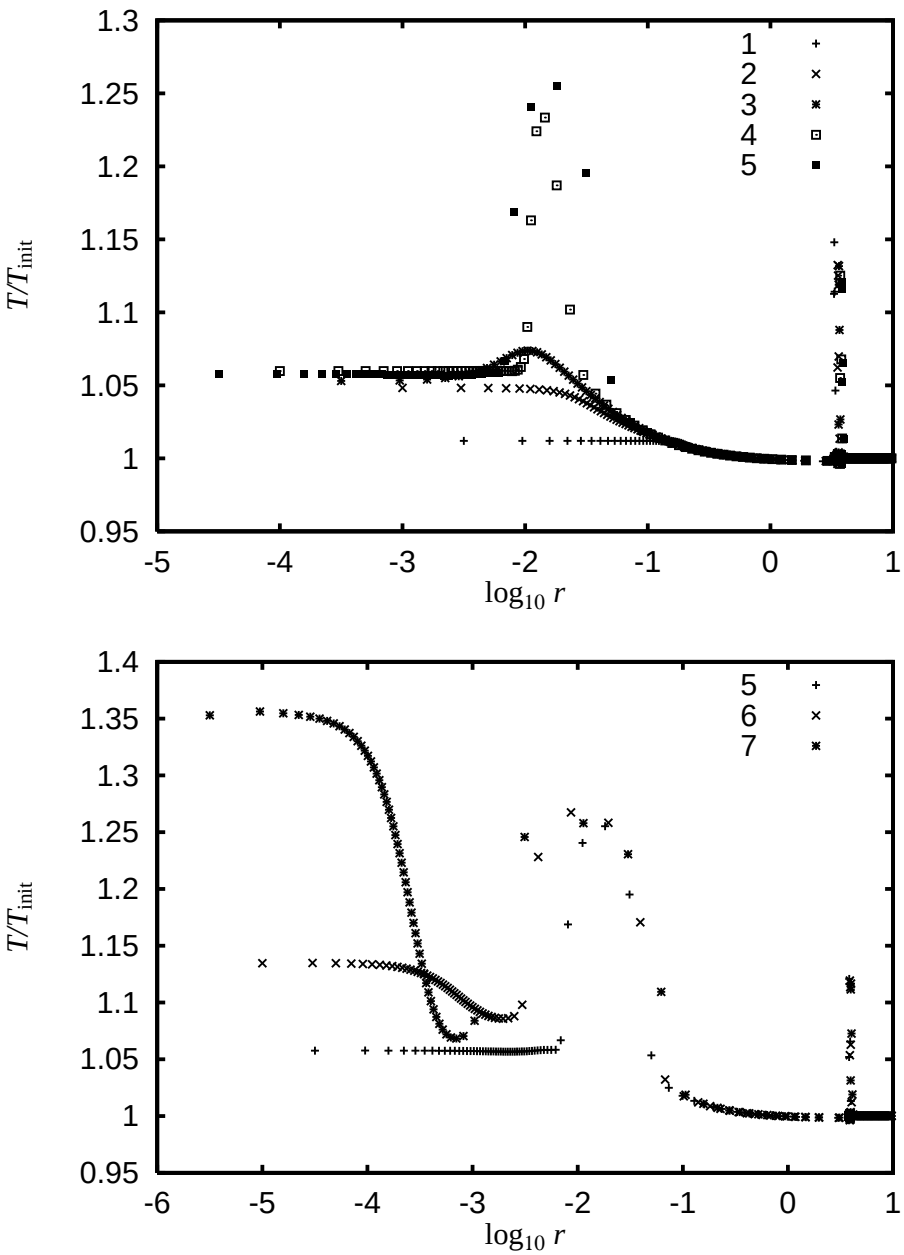

Figure C.2: The temperature for 10 K. Numbers denote $\log_{10}(\rho_c/\rho_{\rm init})$.

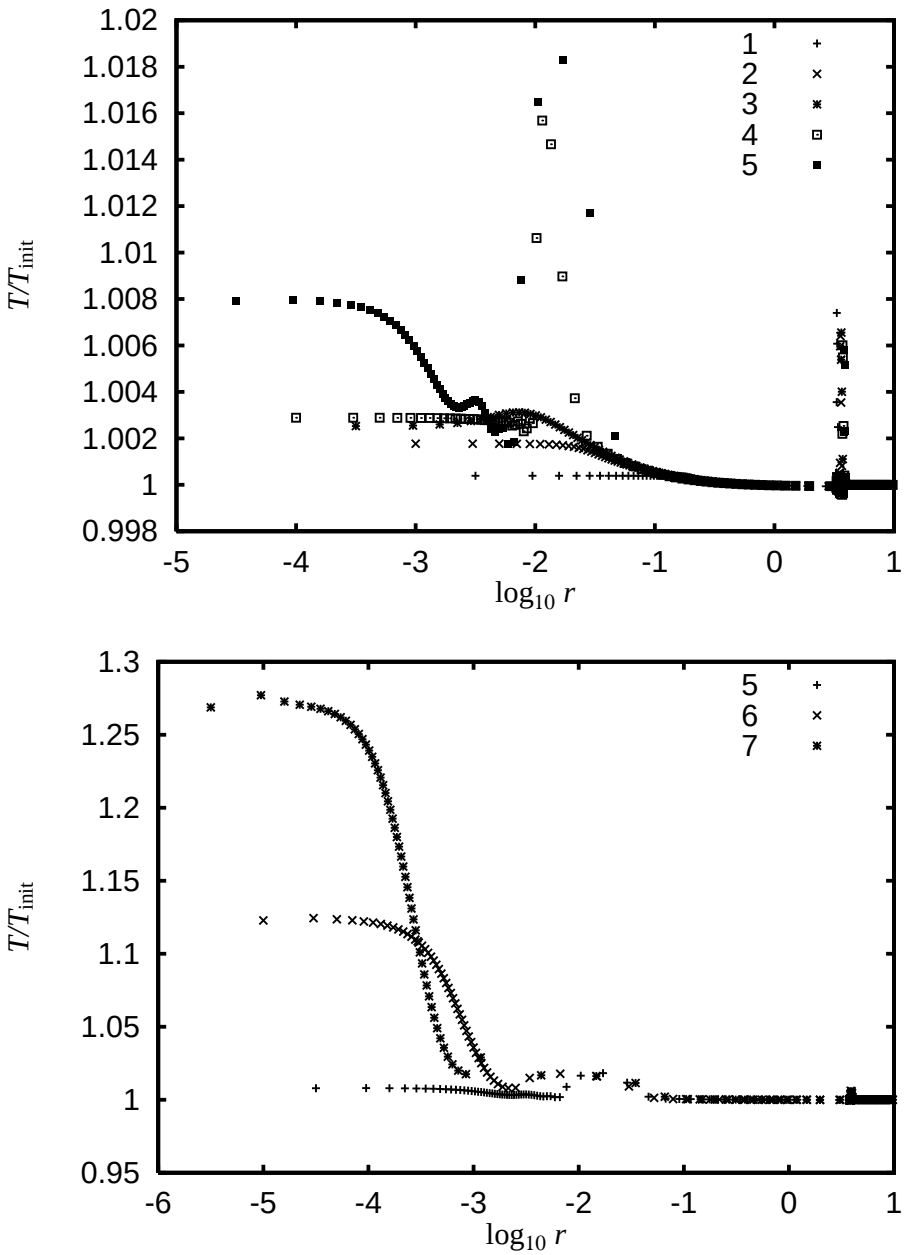

Figure C.3: The temperature for 20 K.

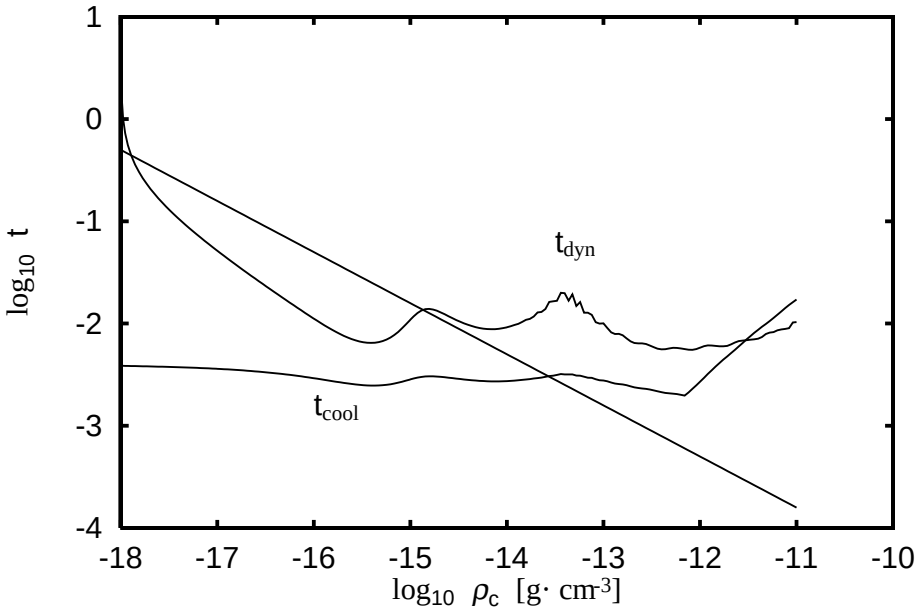

Figure C.4: Time-scales in the case of $T_{\rm init} = 10$ K.

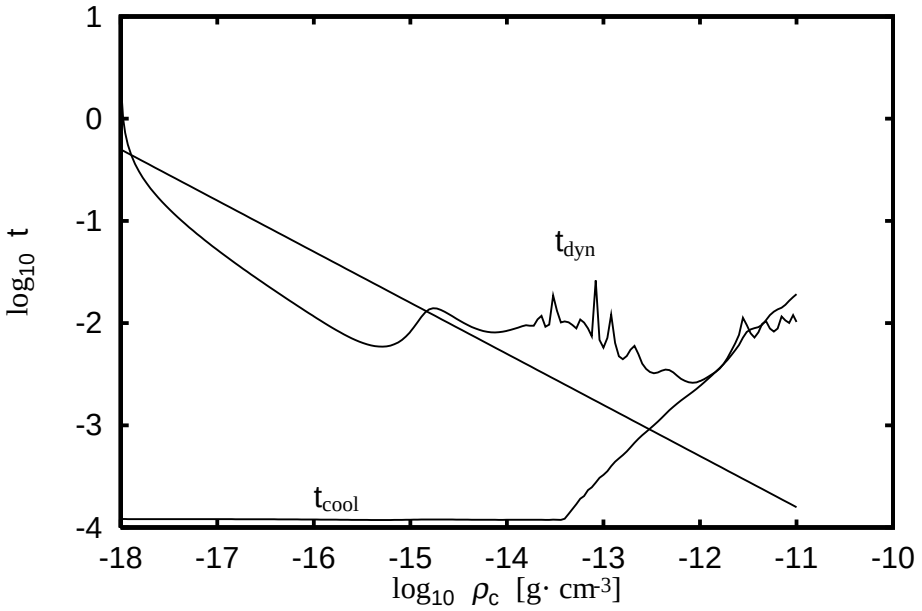

Figure C.5: Time-scale in the case of $T_{\rm init} = 20$ K.

Appendix D

Results of the cosmic ray heating model

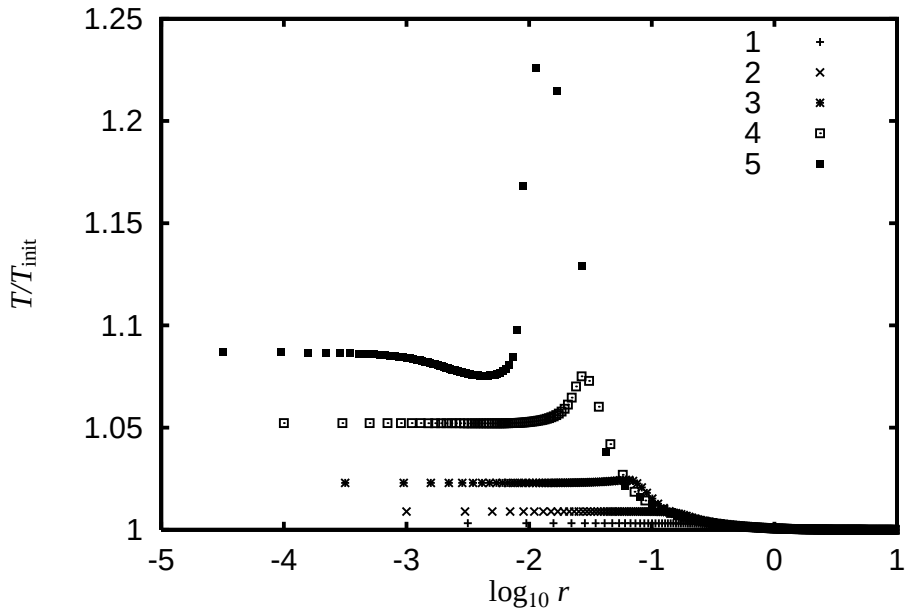

Figure D.1: The gas temperature in the case of $T_{\rm init} = 10$ K.

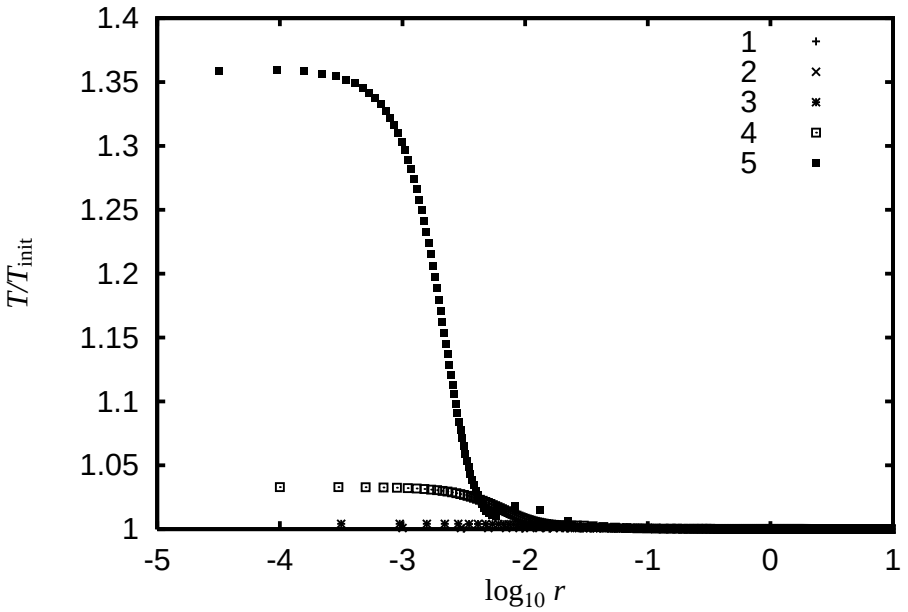

Figure D.2: The gas temperature in the case of $T_{\rm init} = 20$ K.

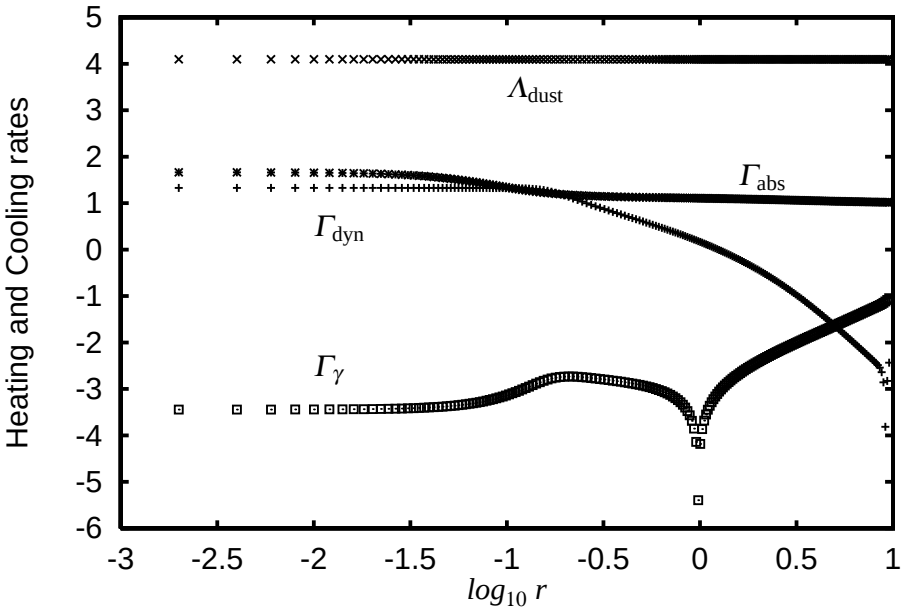

Figure D.3: The heating and cooling rates in the case of $T_{\rm init} = 20$ K at the stage of $\log_{10}(\rho_c/\rho_{\rm init}) = 2$.

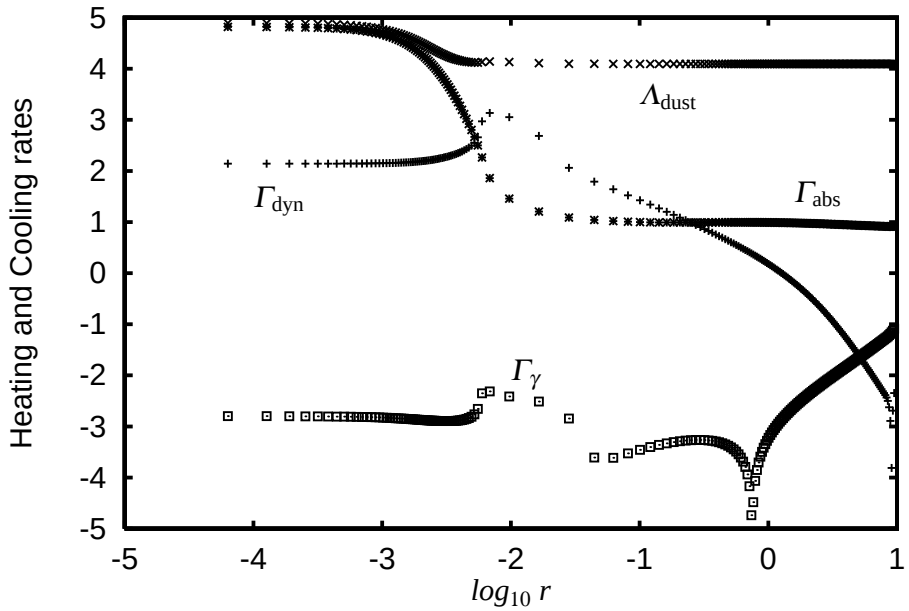

Figure D.4: The heating and cooling rates in the case of $T_{\rm init} = 20$ K. at the stage of $\log_{10}(\rho_c/\rho_{\rm init}) = 5$. The $\Gamma_{\rm abs}$ becomes close to $\Lambda_{\rm dust}$ near the center.

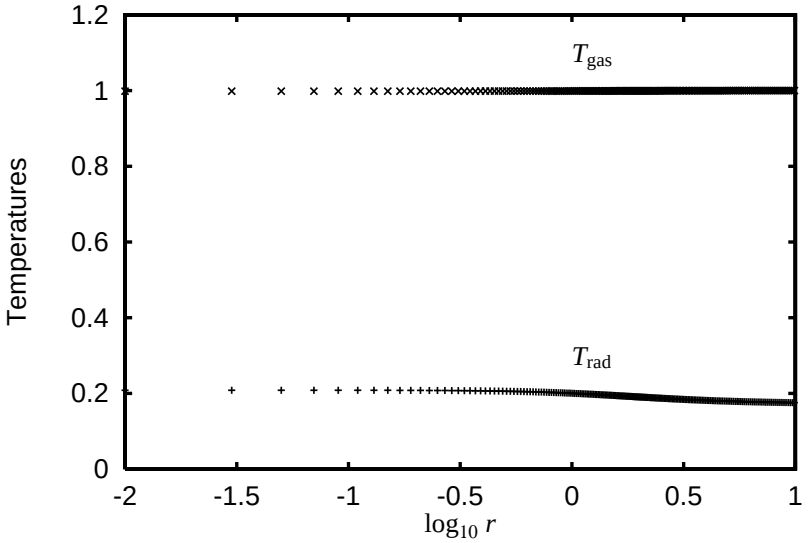

Figure D.5: The distribution of gas temperature and the radiation temperature at an initial time.

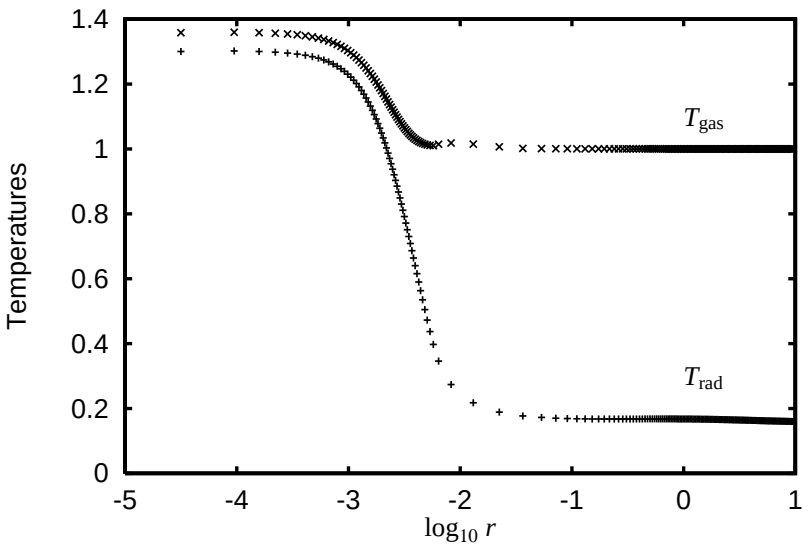

Figure D.6: The gas temperature and the radiation temperature.

Bibliography

[1] Basu, S., and Mouschovias, T. C. Magnetic braking, ambipolar diffusion, and the formation of cloud cores and protostars. 1: Axisymmetric solutions. *Astrophys. J. 432* (1994), 720–741.

[2] Beckwith, S. V. W., and Sargent, A. I. Particle emissivity in circumstellar disks. *Astrophys. J. 381* (1991), 250–258.

[3] de Jong, T., Dalgarno, A., and Boland, W. Hydrostatic models of molecular clouds. *Astron. Astrophys. 91* (1980), 68–84.

[4] Dickman, R. L. A survey of carbon monoxide emission in dark clouds. *Astrophys. J. 202* (1975), 50–57.

[5] Draine, B. T., and Lee, H. M. Optical properties of interstellar graphite and silicate grains. *Astrophys. J. 285* (1984), 89–108.

[6] Goldsmith, P. F., and Langer, W. D. Molecular cooling and thermal balance of dense interstellar clouds. *Astrophys. J. 222* (1978), 881–895.

[7] Hayashi, M., Ohashi, N., and Miyama, S. M. A dynamically accreting gas disk around HL Tauri. *Astrophys. J. Letters 418* (1993), L71–L74.

[8] Inutsuka, S.-i., and Miyama, S. M. Self-similar solutions and the stability of collapsing isothermal filaments. *Astrophys. J. 388* (1992), 392–399.

[9] Inutsuka, S.-i., and Miyama, S. M. A production mechanism for clusters of dense cores. *Astrophys. J. 480* (1997), 681–693.

[10] Kaifu, N., Hasegawa, T., Morimoto, M., Inatani, J., Nagane, K., Miyazawa, K., Chikada, Y., Kanzawa, T., Akabane, K., and Suzuki, S. Rotating gas disk around L1551 IRS-5. *Astron. Astrophys. 134* (1984), 7–12.

[11] Kawachi, T., and Hanawa, T. Gravitational collapse of filamentary clouds. *Publ. Astron. Soc. Japan 50* (1998), 577–586.

[12] Landau, L. D., and Lifshitz, E. M. *Fluid Mechanics.* Addison-Wesley, 1959.

[13] Larson, R. B. Numerical calculations of the dynamics of a collapsing proto-star. *Mon. Not. R. Astron. Soc. 145* (1969), 271–295.

[14] Lis, D. C., Serabyn, E., Keene, J., Dowell, C. D., Benford, D. J., Phillips, T. G., Hunter, T. R., and Wang, N. 350 micron continuum imaging of the Orion a molecular cloud with the submillimeter high angular resolution camera. *Astrophys. J. 509* (1998), 299–308.

[15] Martín, E. L., Basri, G., Zapatero-Osorio, M. R., Rebolo, R., and García López, R. J. The first L-type brown dwarf in the Pleiades. *Astrophys. J. Letters 507* (1998), L41–L44.

[16] Masunaga, H., and Inutsuka, S.-i. Does "$\tau \approx 1$" terminate the isothermal evolution of collapsing clouds? *Astrophys. J. 510* (1999), 822–827.

[17] Masunaga, H., Miyama, S. M., and Inutsuka, S.-i. A radiation hydrodynamic model for protostellar collapse. I. The first collapse. *Astrophys. J. 495* (1998), 346–396.

[18] Mathis, J. S., Mezger, P. G., and Panagia, N. Interstellar radiation field and dust temperatures in the diffuse interstellar matter and in giant molecular clouds. *Astron. Astrophys. 128* (1983), 212–229.

[19] Matsumoto, T., Hanawa, T., and Nakamura, F. Gravitational contraction of rotating clouds: Formation of self-similarly collapsing disks. *Astrophys. J. 478* (1997), 569.

[20] Matsumoto, T., Nakamura, F., and Hanawa, T. Fragmentation of a magnetized filamentary molecular cloud rotating around its axis. *Publ. Astron. Soc. Japan 46* (1994), 243–255.

[21] Mihalas, D., and Mihalas, B. W. *Foundations of Radiation Hydrodynamics*. New York: Oxford Univ. Press, 1984.

[22] Miyake, K., and Nakagawa, Y. Effects of particle size distribution on opacity curves of protoplanetary disks around T Tauri stars. *Icarus 106* (1993), 20.

[23] Miyama, S. M., Narita, S., and Hayashi, C. Fragmentation of isothermal sheet-like clouds. I. Solutions of linear and second-order perturbation equations. *Prog. Theor. Phys. 78* (1987), 1051–1064.

[24] Mouschovias, T. C., and Morton, S. A. Ambipolar diffusion, cloud cores, and star formation: Two-dimensional, cylindrically symmetric contraction. I - The issues, formulation of the problem, and method of solution. *Astrophys. J. 371* (1991), 296–316.

[25] Nakamoto, T., and Ogochi, K. Multi-dimensional radiation hydrodynamics simulations of star and planetary system formation. *Detection and Study of Planets Outside the Solar System, 23rd meeting of the IAU, Joint Discussion 13, 25-26 August 1997, Kyoto, Japan. 13* (1997), E12.

[26] Nakamura, F. What determines the typical mass of dense cores in quiescent, nonmagnetized molecular clouds? *Astrophys. J. Letters 507* (1998), L165–L169.

[27] Nakamura, F., Hanawa, T., and Nakano, T. Fragmentation of filamentary molecular clouds with longitudinal magnetic fields: Formation of disks and their collapse. *Astrophys. J. 444* (1995), 770–786.

[28] Nakamura, F., Matsumoto, T., Hanawa, T., and Tomisaka, K. Gravitational collapse of isothermal magnetized clouds: The universality of self-similar collapse. *Astrophys. J. 510* (1999), 274–290.

[29] Nakamura, F., and Umemura, M. On the mass of population III stars. *Astrophys. J. 515* (1999), 239–248.

[30] Ogochi, K., and Nakamoto, T. The gravitational collapse of filaments: 1D RHD simulations. In *Star Formation 1999* (1999), T. Nakamoto, Ed., Nobeyama Radio Observatory, pp. 193–194.

[31] Ogochi, K., and Nakamoto, T. Radiation hydrodynamical simulations of the gravitational collapse of filamentary gas clouds. In *Numerical*

Astrophysics (1999), S. M. Miyama, K. Tomisaka, and T. Hanawa, Eds., Kluwer Academic Publishers, pp. 171–172.

[32] Padgett, D. L., Brandner, W., Stapelfeldt, K. R., Strom, S. E., Terebey, S., and Koerner, D. Hubble space telescope/NICMOS imaging of disks and envelopes around very young stars. *Astron. J. 117* (1999), 1490–1504.

[33] Pollack, J. B., Hollenbach, D., Beckwith, S., Simonelli, D. P., Roush, T., and Fong, W. Composition and radiative properties of grains in molecular clouds and accretion disks. *Astrophys. J. 421* (1994), 615–639.

[34] Rees, M. J. Opacity-limited hierachical fragmentation and the masses of protostars. *Mon. Not. R. Astron. Soc. 176* (1976), 483–486.

[35] Rybicki, G. B., and Lightman, A. P. *Radiative Processes in Astrophysics*. John Wiley & Sons, Inc., 1979.

[36] Schneider, S., and Elmegreen, B. G. A catalog of dark globular filaments. *Astrophys. J. Suppl. 41* (1979), 87–95.

[37] Silk, J. On the fragmentation of cosmic gas clouds. II. Opacity-limited star formation. *Astrophys. J. 214* (1977), 152–160.

[38] Stahler, S. W., Shu, F. H., and Taam, R. E. The evolution of protostars. I — Global formulation and results. *Astrophys. J. 241* (1980), 637–654.

[39] Stahler, S. W., Shu, F. H., and Taam, R. E. The evolution of protostars. II — The hydrostatic core. *Astrophys. J. 242* (1980), 226–241.

[40] Stahler, S. W., Shu, F. H., and Taam, R. E. The evolution of protostars. III — The accretion envelope. *Astrophys. J. 248* (1981), 727–737.

[41] Stone, J. M., Mihalas, D., and Norman, M. L. ZEUS-2D: A radiation magnetohydrodynamics code for astrophysical flows in two space dimensions. III. The radiation hydrodynamic alogrithms and tests. *Astrophys. J. Suppl. 80* (1992), 819–845.

[42] Stone, J. M., and Norman, M. L. ZEUS-2D: A radiation magnetohydrodynamics code for astrophysical flows in two space dimensions. I. The dydrodynamic alogrithms and tests. *Astrophys. J. Suppl. 80* (1992), 753–790.

[43] Tomisaka, K. Collapse and fragmentation of magnetized cylindrical clouds. *Astrophys. J. 438* (1995), 226–243.

[44] Tomisaka, K. Accretion in gravitationally contracting clouds. *Publ. Astron. Soc. Japan 48* (1996), L97–L101.

[45] Tomisaka, K. Collapse and fragmentation of cylindrical magnetized clouds: Simulation with nested grid scheme. *Publ. Astron. Soc. Japan 48* (1996), 701–717.

[46] Tomisaka, K. Collapse-driven outflow in star-forming molecular cores. *Astrophys. J. Letters 502* (1998), L163.

[47] Uehara, H., Susa, H., Nishi, R., Yamada, M., and Nakamura, T. Fragmentation of the primordial gas clouds and the lower limit on the mass of the first stars. *Astrophys. J. Letters 473* (1996), L95–L98.

[48] Winkler, K.-H. A., and Newman, M. J. Formation of solar-type stars in spherical symmetry. I. The key role of the accretion shock. *Astrophys. J. 236* (1980), 201–211.

[49] Winkler, K.-H. A., and Newman, M. J. Formation of solar-type stars in spherical symmetry. II. Effects of detailed constittive relations. *Astrophys. J. 238* (1980), 311–325.

[50] Yorke, H. W. Numerical solution of the equation of radiation transfer in spherical geometry. *Astron. Astrophys. 86* (1980), 286–294.

[51] Zapatero Osorio, M. R., Béjar, V. J. S., Rebolo, R., Martín, E. L., and Basri, B. An L-type substellar object in Orion :Reaching the mass boundary between brown dwarfs and giant planets. *Astrophys. J. Letters 524* (1999), L115–L118.